# Bond model of steel reinforcement embedded in low binder concrete

**Ricardo Vaz Nogueira Henriques de Bastos**

Dissertation for the obtention of the Master's Degree in

## Civil Engineering

Supervisors:

Dr. Ana Sofia Miranda da Silva Louro

Prof. Eduardo Nuno Brito Santos Júlio

### Examination Committee

Chairperson: Prof. Mário Manuel Paisana dos Santos Lopes

Supervisor: Dr. Ana Sofia Miranda da Silva Louro

Member of the committee: Prof. Jorge Manuel Vinagre Alfaiate

Member of the committee: Dr. Manuel José de Andrade Loureiro Pipa

**May 2022**

# Declaration

I declare that this document is an original work of my authorship and that it fulfils all the requirements of the University of Lisbon's Code of Conduct and Good Practices.

The present dissertation was prepared at Laboratório Nacional de Engenharia Civil, under the protocol between IST and LNEC.

## Acknowledgements

I would like to thank Dr. Ana Sofia Miranda da Silva Louro for sharing her knowledge and time and for aiding me throughout this work. I am very grateful for the commitment and patience that I know were necessary to help take this work to its completion. I will never forget the sympathy and kindness with which I was treated and the constant support that I received through some difficult times that I went through whilst writing this dissertation.

I would also like to thank Prof. Eduardo Nuno Brito Santos Júlio for aiding me in this work. His sharing of knowledge and remarks were always sincere and direct, and I always felt motivated by his words. I am truly grateful to have had the opportunity to learn from him.

I would like to thank my parents for supporting me through the years and for the sacrifices they made to afford me my education. I would especially like to thank my Mother for being my safe haven and helping me always to make it through the storm. I would also like to thank my brother Gonçalo, whose joyous and extravagant personality always makes me see the best side of life.

I also would like to thank some of my friends, which without their support, I would not be able to achieve my goals. First, to my best friend, Carolina Costa Rebelo, thank you for believing in me and always being there to help me when I am down. To my colleague Afonso Ataíde, thank you for being my companion throughout the many challenges and misadventures that we had throughout the years; without you, I would not have gone so far. Last but not the least, thank you to my colleagues Rodrigo Santos, Fábio Albuquerque, Syndykyle Kopingo and Vanessa Alves for helping me through university; your small acts of kindness towards me have not been forgotten.

# Resumo

O presente trabalho apresenta uma nova lei de aderência para varões de aço e betão com baixa dosagem de ligante. A lei de aderência foi obtida por um processo de calibração empírico baseado nos resultados dos ensaios de arrancamento de Louro (2014), Freitas (2016) e Pereira (2019). Estes resultados são relativos a 31 séries de teste e um total de 138 ensaios realizados utilizando diferentes tipos de betão. Além disso, os espécimenes ensaiados nessas campanhas foram replicados através de modelos de elementos finitos recorrendo ao software ATENA. A modelação do comportamento local da aderência foi realizada através de uma abordagem fenomenológica que permitiu comparar resultados experimentais e numéricos utilizando a nova lei de aderência e as leis pré-existentes do fib Model Code 2010, Louro (2014), Freitas (2016) e Pereira (2019). Adicionalmente, foram modeladas duas vigas para estudar a influência da resistência da aderência sobre os comprimentos de ancoragem/emenda.

As conclusões retiradas foram as seguintes: a calibração da nova lei incorporou a influência dos parâmetros área relativa das nervuras, compacidade, diâmetro dos varões e teor de agregados reciclados. Ademais, a calibração da lei melhorou a precisão da previsão da resistência da aderência comparativamente às leis anteriores. Os modelos de ensaios de arrancamento simularam com sucesso a aderência local. Os modelos de vigas revelaram uma relação linear entre o comprimento de ancoragem/emenda e a resistência da aderência. Finalmente, determinou-se que a consideração adequada da capacidade de aderência nas zonas de ancoragem pode contribuir para a sustentabilidade da indústria da construção.

**Palavras-chave**

Lei de aderência, ensaios de arrancamento, betão com baixa dosagem de ligante, análise de elementos finitos, comprimento de ancoragem

# Abstract

The present work presents a new bond model of steel reinforcement embedded in low binder concrete. The bond model was obtained through an empirical calibration process based on the results of the pull-out test campaigns from Louro (2014), Freitas (2016) and Pereira (2019). These results comprise data from 31 test series of 138 pull-out tests conducted with various concrete types. Furthermore, the specimens from these campaigns were emulated through the finite element modelling of the pull-out tests through the ATENA software. The finite element modelling of the local bond behaviour was produced through a phenomenological approach which enabled the comparison between experimental results and numerical results using the new bond model and the pre-existing ones of fib Model Code 2010, Louro (2014), Freitas (2016) and Pereira (2019). Subsequently, two beams were modelled to study the influence of the bond strength over the anchorage/lap-splice length.

The conclusions from this work were as follows: the calibration of a new bond model incorporated the influence of the bond-related parameters of bond index, bar diameter, packing density and recycled aggregate content. Moreover, it improved the bond strength prediction accuracy compared to previous models. The modelling performed for the pull-out test successfully simulated the local bond behaviour. The beam models revealed a linear relationship between the variation of bond strength and anchorage/lap-splice length. Lastly, the proper consideration of the bond strength capacity at anchorage zones can have an important effect on material savings and contribute to the construction industry's sustainability.

**Keywords**

Bond model, pull-out test, low binder concrete, finite element analysis, anchorage length

# Index

# List of Tables

# List of Figures

# List of Abbreviations

| | |
|---|---|
| 1D | One dimensional |
| 3D | Three dimensional |
| ACI | American concrete institute |
| BS | British standard |
| CDW | Construction and demolition waste |
| EC2 | Eurocode 2 |
| EN | European standard |
| FE | Finite element(s) |
| HSC | High strength concrete |
| ISO | International organization for standardization |
| LBC | Low binder concrete |
| LCRAC | Low cement recycled aggregate concrete |
| ME | Macro-element |
| NA | Natural aggregate |
| NP | Portuguese standard |
| NSC | Normal strength concrete |
| OC | Ordinary concrete |
| POT | Pull-out test |
| PSD | Particle size distribution |
| RA | Recycled aggregate |
| RAC | Recycled aggregate concrete |
| RCA | Recycled coarse aggregate |
| RCAr | Replacement percentage of recycled coarse aggregate |
| RFA | Recycled fine aggregate |
| RFAr | Replacement percentage of recycled fine aggregate |
| SPEC | Specimens |
| SLS | Serviceability limit state |
| SSD | Saturated and surface-dry moisture state |
| ULS | Ultimate limit state |

# List of Symbols

## Latin capital letters

| | |
|---|---|
| $A$ | Cross-sectional area of a 1D bar finite element |
| $A_{gt}$ | Steel strain at ultimate strength |
| $C_b$ | Bond stress-slip function |
| $E$ | Modulus of elasticity |
| $F_a$ | Pull-out force |
| $RA_{<c}$ | Percentage of recycled aggregate with size inferior to the rib spacing |
| $RA_{\geq c}$ | Percentage of recycled aggregate with size superior or equal to the rib spacing |
| $R_m$ | Steel ultimate strength |

## Latin lowercase letters

| | |
|---|---|
| a | Rib height |
| $a_m$ | Rib height at mid-point |
| c | Rib spacing |
| d | Nominal diameter of the reinforcement |
| $f_c$ | Compressive strength of concrete |
| $f_{cm}$ | Mean compressive strength of concrete measured in cylinders |
| $f_{cm,cube}$ | Mean compressive strength of concrete measured in cubes |
| $f_{cm,28}$ | Mean compressive strength of concrete at 28 days |
| $f_{cm,j}$ | Mean compressive strength of concrete at *j* days |
| $f_R$ | Relative rib area/bond index |
| $f_y$ | Steel yield strength |
| i | Rib inclination |
| $l_b$ | Anchorage length/lap-splice length |
| p | Perimeter of a 1D bar finite element |
| s | Bond slip |
| $s_1$ | Bond slip relative to the beginning of the bond stress-slip curve's plateau |
| $s_2$ | Bond slip relative to the end of the bond stress-slip curve's plateau |
| $s_3$ | Bond slip relative to the beginning of the residual bond capacity |
| u | Displacement at the concrete finite element node |
| $\vec{u}$ | Displacement at the reinforcing bar finite element node |
| $v_p$ | Constant loading speed of the pull-out force |
| w/b | Water-binder ratio |
| w/c | Water-cement ratio |

## Greek capital letters

| | |
|---|---|
| $\Sigma e_i$ | Circumference part of the reinforcement cross-section without ribs |

## Greek lowercase letters

| | |
|---|---|
| ά | Rib face angle |
| $\varepsilon_s$ | Steel strain |
| $\varepsilon_{s,y}$ | Steel strain at yielding |
| σ | Packing density |
| $\sigma_i$ | Normal stress found in bar finite element i |
| $\tau_b$ | Local bond stress |
| $\tau_d$ | Normalised bond stress |
| $\tau_{bf}$ | Local residual bond stress |
| $\tau_{bmax}$ | Local bond strength |

# 1. Introduction

## 1.1 Framework

The present dissertation is centred on the bond behaviour of embedded steel reinforcement, with a special focus on the use of ecological concrete types involving recycled aggregates (RA) and low quantities of cement. The intention behind the focal study of the behaviour of these types of concrete comes from the current necessity to facilitate and promote the sustainability of the construction industry, which can be achieved by the proper employment of materials with a lower ecological footprint.

Concrete is the most widely used construction material globally and a significant contributor to climate change. The carbon dioxide released during concrete production mainly comes from Portland cement, which makes up 74 to 81% of the total $CO_2$ emissions from concrete (Flower and Sanjayan 2007). The chemical and thermal processes involved in cement production have a massive carbon footprint, being the source of around 8% of the world's $CO_2$ emissions. Currently, more than 4 billion tonnes of cement are produced worldwide, and with concrete taking a significant role in the construction industry of emerging countries, global production is set to increase to 5 billion tonnes by the end of 2030 (Lehne and Preston 2018).

Furthermore, due to the high percentage of coarse aggregate used in concrete (60 to 75% of the total concrete volume, according to Kosmatka *et al.* (1996)), a sustainable and economical source for obtaining high-quality aggregate is essential to the construction industry. Availability of high-quality aggregate sources close to growing urban centres, where the construction demand is high, might be limited; thus, RA produced from the concrete remnants of construction and demolition waste (CDW) is a potential solution to this problem. In this way, there is a potential to reduce aggregate costs as well as $CO_2$ emissions associated with transportation. For the past years, the production of concrete using recycled materials has been increasingly encouraged. According to the European Aggregates Association, the yearly aggregate demand by weight surmounts 3 billion tonnes, with RA only accounting for 8% of the total aggregate production, contrasting with the 87% generated from natural resources in quarries and pits.

Engineers considering the structural use of low quantities of binder and RA to promote the sustainability of concrete construction need to understand the behaviour of these innovative concrete types and how it compares to ordinary concrete (OC). The bond between steel reinforcing bars and concrete has significant importance in the structural performance of concrete structures, both under ultimate and serviceability limit states. Therefore, it is necessary to know the extent to which the current design codes' recommendations can accurately predict the structural response of reinforced concrete members built using new materials such as low binder concrete (LBC), produced with natural and/or recycled aggregates.

## 1.2 Goals

The present dissertation follows the studies performed by Louro (2014), Freitas (2016) and Pereira (2019). These authors performed experimental pull-out tests (POT) and drew important conclusions regarding the influence of several parameters on the local bond stress-slip response of ribbed reinforcing bars embedded in concrete. The target goals of the present work are the following:

- Calibration of a new local bond stress-slip model for steel reinforcement embedded in OC, LBC or low cement recycled aggregate concrete (LCRAC). The calibration is intended to be based on previous bond models presented in the literature and be supported by the experimental data from the POT campaigns of Louro (2014), Freitas (2016) and Pereira (2019).
- Finite element (FE) modelling of the local bond behaviour by replicating the POT specimens of Louro (2014), Freitas (2016) and Pereira (2019).
- Evaluation of the current bond models (including the new calibrated model) through comparison between experimental and numerical results.
- FE modelling of structural members using the local bond model utilised in the POT numerical models. This goal is intended to evaluate the bond behaviour of reinforcement with long embedded lengths and their performance at the anchorage zones.

## 1.3 Structure of the dissertation

The dissertation is organized into six chapters, described next. In addition, a list of consulted bibliographic references and five annexes are also presented.

Chapter 1 presents a framework to justify the development of the present work, followed by the definition of the dissertation's goals and a description of the work's structure.

Chapter 2 presents the state-of-the-art regarding the bond of embedded steel reinforcement. First, the concept of bond is explained, and its resistant mechanisms are addressed. Consequently, the bond stress-slip interaction description is presented, followed by an account of the known parameters that influence the bond behaviour. Additionally, an exposition is made regarding the effects of different concrete types on the bond performance, such as recycled aggregate concrete (RAC) and LBC/LCRAC.

Chapter 3 addresses the empirical calibration of a new bond stress-slip model. Firstly, an account regarding the experimental data that supports the calibration process is delivered, and secondly, some of the existing bond models are addressed. Subsequently, the proper calibration process is exposed, starting with the methodology adopted and followed by the results obtained.

Chapter 4 presents an account of the finite element modelling of bond behaviour by exposing in detail the specific models built for the dissertation.

Chapter 5 presents and discusses the results of the numerical analysis described in previous chapters.

Chapter 6 draws the main conclusions for the present work and presents suggestions for future work.

# 2. State of the art

## 2.1 Bond of embedded steel reinforcement

### 2.1.1 Concept

Bond can be described as the set of physicochemical phenomena that occurs in the interface between steel reinforcement and concrete and is responsible for the transfer of forces between both materials, thus ensuring strain compatibility and composite action. Therefore, bond exerts a strong influence over structural behaviour, be it at the serviceability limit state (SLS) or ultimate limit state (ULS), making it an essential subject of study in the field of the structural behaviour of reinforced concrete structures.

Regarding the SLS, bond influences the cracking behaviour of reinforced concrete. For a structural member provided with the minimum reinforcement necessary to avoid yielding of the steel at first cracking, when subjected to axial tension or bending, the bond will ensure the transfer of stresses between materials, thus promoting the development of secondary cracking in the concrete. As a result, bond helps to reduce the cracks' width and spacing and limits the overall deformation.

At the ULS, bond is responsible for defining anchorage and lap-splice lengths, enabling the adequate structural response of the main load-carrying mechanisms. At this state, bond should also guarantee a large rotation capacity of plastic hinges after the yielding of steel to provide sufficient ductility and energy dissipation of the structural member.

To obtain an optimal behaviour for both limit states, a compromise regarding the bond properties is necessary since the ULS and SLS's individual needs can be detrimental to each other. Mayer and Eligehausen (1998) approached this subject, underlining that high bond resistance and stiffness are required to limit crack opening and overall deformation to acceptable values, while conversely, assuring the necessary ductility for the large rotation capacity of plastic hinges means that bond resistance after passing the steel yield strain should be low.

### 2.1.2 Resistant mechanisms of bond

The resistance mechanisms comprising the bond of steel reinforcement embedded in concrete are well documented in *fib* Model Code 2010. They are separated into three different phenomena: chemical adhesion, mechanical interlock and active friction.

Chemical adhesion, which results from the connection between the cement paste and the steel, is responsible for bond resistance in the early loading stages. This chemical interaction enables a perfect connection between both materials, thus maintaining equal strains on concrete and steel at the interface level. However, when the applied load increases, the chemical adhesion starts to break, thus generating relative displacements between the steel reinforcement and surrounding concrete. At this point, there is a complete and irretrievable loss of chemical adhesion, requiring bond to rely solely on mechanical interlock and active friction.

The mechanical interlock results from the interaction between the steel rebar ribs and the concrete set in front of them and mainly works due to the reaction stresses originating from both materials contacting, hence obstructing rebar slippage. By loading the reinforcement, compressive and tensile reaction stresses will be generated at the tip of the ribs, leading to a wedging effect, consisting of the crushing and shearing off of the concrete between the ribs and cracking of the surrounding concrete. This mechanism is mainly responsible for bond resistance prior to failure, at which point active friction takes a critical role.

Lastly, active friction derives from surface contact forces and depends on the normal forces applied to the interface and the surface treatment provided to the steel reinforcement before casting. Of the three mechanisms, the mechanical interlock is regarded as the most influential to the bond behaviour of ribbed steel bars before failure. According to the research on the bond performance of different bar types performed by Xing *et al.* (2015), the bond strength of plain steel bars corresponds to just 18.3% of that obtained for ribbed steel bars being this discrepancy due to the lack of ribs on the former, which results in minor mechanical interlock.

The authors also compared the bond behaviour of plain steel bars and plain aluminium alloy (Al-alloy) bars to evaluate the influence of chemical adhesion and active friction separately. The premise enabling this evaluation is that plain Al-alloy bars, having a barrier oxide film bonded strongly to their surface, have very smooth surfaces, thus preventing any significant friction forces from occurring, making bond resistance solely dependent on chemical adhesion. Results showed that the bond strength of plain Al-alloy bars was ten times smaller than that of plain steel bars, indicating that chemical adhesion has the smallest influence on bond strength.

### 2.1.3 Bond stress-slip relationship

The local bond behaviour can be described in terms of the bond stress-slip relationship. Figure 1 presents the qualitative relationship with its various stages (I to IV) identified according to the parameters and conditions to which the bond can be subjected.

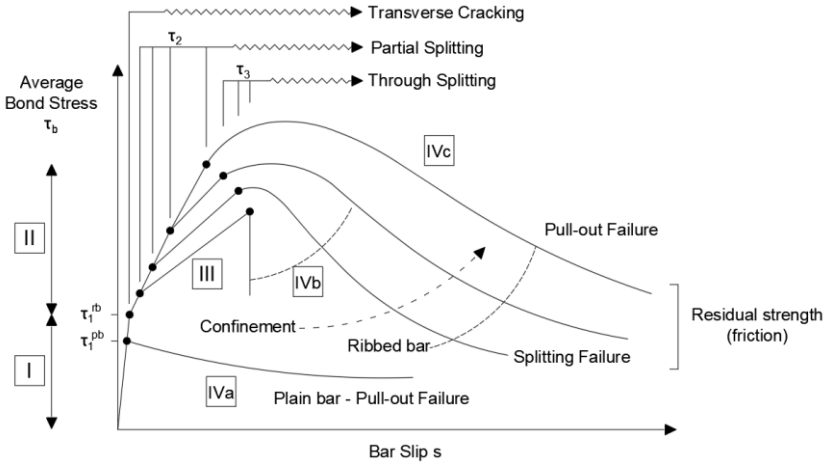


Figure 1 – Bond stress-slip relationship for the bond of embedded steel reinforcement, adapted from Bond of Reinforcement in Concrete: State-of-the-art report, *fib* (2000).

At stage I, the curve takes off in a steep ascending branch with concrete remaining uncracked and chemical adhesion being the main responsible for bond resistance. The low values of bond stress cause little to no rebar slippage; however, it is common to find elevated stresses near the ribs' tip at this point.

Stage II is reached once bond stress levels surpass that lower range, meaning that breakage of the chemical adhesion occurs. The bearing stresses applied by the tip of the ribs to the neighbouring concrete continue to increase, leading to transversal micro-cracking, which allows for slippage of the rebar and relative displacements between materials.

As the loading further increases, the rebar ribs start developing a wedging action against the concrete in front of them, crushing it and generating longitudinal splitting cracks that spread radially to the rebar axis. These processes can be described as stage III, where the concrete surrounding the reinforcement will exert a confinement action, and mechanical interlock will be the main responsible for bond resistance.

Whilst rebar slippage values continue to increase, the same happens with the bond stress until a peak value is reached. The maximum bond stress value, referred to as bond strength, means the end of the bond stress-slip curve's ascending branch and the starting point of the various bond failure mechanisms. Stage IV corresponds to the decrease of bond stress and the continuing increase of the rebar slippage, with the shape of the bond stress-slip curve varying mainly according to the level of confinement provided to the bar. In the instance where light to no transverse reinforcement is provided (stage IVb), confinement levels will be low and longitudinal cracks will easily propagate through the concrete cover and the rebar spacing, resulting in an abrupt brittle failure due to splitting. Otherwise, when heavy reinforcement is provided by stirrups (stage IVc), good confinement conditions are ensured, thus hindering the propagation of longitudinal cracks and limiting splitting to a cracked core around the rebar. This way, the wedging action developed by the ribs will be more aggressive, crushing and shearing off the concrete in front of them and smoothing the steel-concrete interface. Thus, the result is a ductile bond failure by pulling out the rebar. However, an intermediate scenario can occur, where moderate confinement may lead to the simultaneous occurrence of different stages of the bond stress-slip interaction along the embedded length of the bar, resulting in a splitting-induced pull-out failure.

At failure, bond stress will decrease with increasing slip values in what can be described as the descending branch of the bond stress-slip curve. When slip values are equal to the rib spacing, it means that the concrete between ribs has been completely crushed and sheared off, demanding bond resistance to rely solely on its residual capacity, i.e. active friction.

Lastly, concerning the behaviour of plain reinforcement, given the absence of mechanical interlock, the failure of bond (stage IVa) will occur following the breakage of chemical adhesion. Bond stresses due to active friction will decrease with increasing rebar slippage, mimicking the behaviour of ribbed bars under pull-out failure.

### 2.1.4 Parameters influencing bond behaviour under monotonic loading

#### 2.1.4.1 Concrete strength

The effect of concrete properties on bond behaviour has often been represented in descriptive expressions by the square root of the concrete's compressive strength, $\sqrt{f_c}$ (Tepfers (1973), Orangun *et al.* (1977) and Darwin *et al*. (1992)). This representation has proven accurate for concrete with a compressive strength lower than 55 MPa, approximately. Eligehausen *et al*. (1983) tested pull-out specimens with normal (NSC) and high strength concrete (HSC) with compressive strengths from 30 to 54.6 MPa, respectively. Specimens with higher compressive strength had greater bond stiffness and strength. Bond strength increased around 35%, approximately the same increase noticed for the concrete tensile strength between NSC and HSC, which was shown to vary proportionally with $\sqrt{f_c}$.

Some studies regarding the bond behaviour of HSC have shown that past a specific compressive strength value, bond strength starts to decrease. For example, Tepfers (1973) noted that concrete with compressive strength higher than 68.6 MPa started having decreased bond strength values. In addition, shrinkage problems originated due to the higher quantities of cement in HSC mixtures, creating additional tensile stresses around the reinforcement, separate from those originated by the bond performance, thus resulting in weakened bond strength.

However, more recent studies have presented contrary evidence, with bond strength still increasing for very high compressive strength values. Such are the cases of Alavi-Fard and Marzouk (2004), Arel and Yazici (2012), Shen *et al.* (2016) and Yoo and Shin (2018). For example, the pull-out load versus compressive strength results of Arel and Yazici, presented in Figure 2, indicates that bond resistance increases with higher compressive strength values and thicker cover distances, although the rate of increase diminishes for HSC.

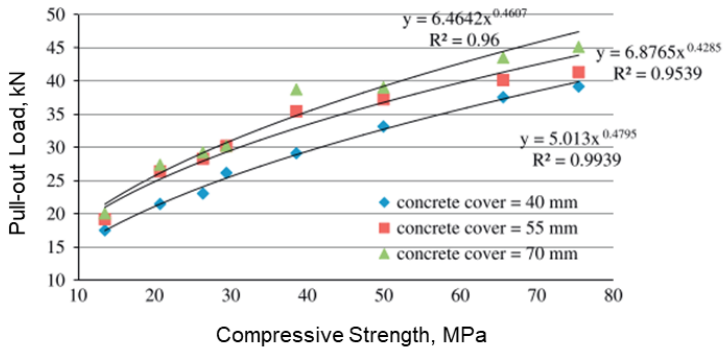


Figure 2 – Pull-out load versus compressive strength, adapted from Arel and Yazici (2012).

Azizinamini *et al.* (1995) consider that, comparatively to NSC, the bearing capacity of HSC (which relates to $f_c$) increases more rapidly than the tensile strength (which in turn relates to $\sqrt{f_c}$), thus preventing the crushing of the concrete between ribs and subsequently reducing the slip. Slip reduction, in turn, equates with fewer ribs being able to transfer the load between the concrete and steel, leading to a brittler bond behaviour. Alavi-Fard and Marzouk support these statements. Their study of the bond performance of

HSC with compressive strengths ranging from 70 to 95 MPa registered a brittle bond behaviour due to a sudden loss of bond stress right after bond strength values were reached.

Some studies have suggested the use of $f_c^{1/3}$ and $f_c^{1/4}$ to better represent the influence of concrete strength over bond, as were the cases of Zsutty (1985) for the former and Darwin *et al.* (1996) and Zuo and Darwin (1998, 2000) for the latter. Zuo and Darwin (1998), based on a database of 171 test specimens of developed/spliced bars with no transverse reinforcement, investigated the ability of $f_c^{1/4}$ to represent the effect of concrete strength. The authors plotted a test-prediction versus $f_c$ graphic, depicted in Figure 3 (a), containing two best-fit lines based on an optimised descriptive equation for bond strength, one using $f_c^{1/4}$ and the other $f_c^{1/2}$. The best-fit line of $f_c^{1/4}$ remains approximately horizontal and close to the test-prediction ratio value of one, whereas the one of $f_c^{1/2}$ has a negative slope with a much steeper inclination due to the test-prediction ratio values of specimens with HSC. This fact indicates that $f_c^{1/2}$ might not provide the best representation for HSC with no transverse reinforcement.

The same authors repeated the previous process for a database of 161 specimens with transverse reinforcement. This time, best-fit lines of test-prediction ratio versus compressive strength, which are depicted in Figure 3 (b), were based on $f_c^p$ with $p$ equal to ¼, ½, ¾ and 1. In this instance, $f_c^{1/4}$ provided a poor representation by underestimating the effect of the concrete strength. The power of ¾ was better adjusted to the experimental data, with the best-fit line possessing a small slope.

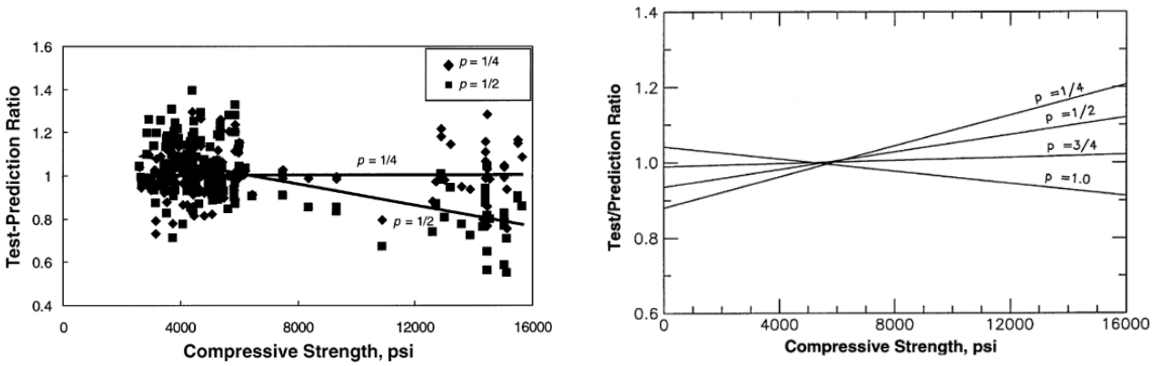


(a) (b)

Figure 3 – Test-prediction ratio versus concrete compressive strength for developed/spliced bars not confined (a) and confined by transverse reinforcement (b).
The contribution of concrete to bond strength is characterised by $f_c^p$.
Adapted from ACI Committee 408 (2003). (Note: 1000 psi = 6.89 MPa)

On the whole, the previous data indicate that the use of $\sqrt{f_c}$ for the representation of the concrete strength effect on bond leads to an overestimation of bond strength for HSC whilst providing good results for NSC.

#### 2.1.4.1 Confinement

Concrete confinement can be described as the restraining effect to concrete lateral expansion due to the employment of lateral compressive pressure. The origin of this lateral pressure can be active or

passive. Active confinement is due to compressive stresses applied externally to a structural member, such as those resulting from the interaction with other structural members or the direct application of external forces. On the other hand, passive confinement is due to stresses originating within the member because of transverse reinforcement and concrete cover. For example, in a beam-column connection, the upper part of the column provides active confinement whilst the column's longitudinal reinforcement ensures passive confinement. Between the two types of confinement, the active one reveals to be the most efficient since its effect is not dependent on the mobilisation of bond stresses. In turn, passive confinement depends on the concrete dilatancy, which accompanies crack formation and is strictly related to the actual bond.

Confinement is said to warrant positive effects on bond behaviour, such as greater ductility to bond failure modes and higher residual capacity. The compressive confinement stresses acting transversally to the reinforcement's direction will counteract the tensile stresses originated by the mechanical interlock between the reinforcement and concrete. Consequently, the opening of splitting cracks will be hindered, favouring the crushing and shearing off of the concrete in front of the ribs, therefore increasing the likelihood of a ductile failure mode by pull-out. Compressive confinement stresses will also increase active friction between materials, resulting in higher bond stress values after failure and a lower slope of the descending branch of the bond stress-slip curve. (*fib*, 2000)

Research has revealed that higher confinement levels may lead to an increase in bond strength. Eligehausen *et al.* (1983) performed several pull-out tests, where the specimens were subjected to a unidirectional confining pressure, applied perpendicular to the splitting plane. Results showed an increase of 25% in bond strength when confinement levels were raised from 0 to 13.10 MPa. Malvar (1991), which conducted pull-out tests, achieved an increase in bond strength of about 200% when confinement pressure was raised from 500 to 4500 psi (approximately 3.45 to 31.03 MPa). The results of the pull-out testing performed by Yasojima and Kanakubo (2004), presented in Figure 4, indicate increased bond strength with the increase of the lateral confinement stress and concrete compressive strength.

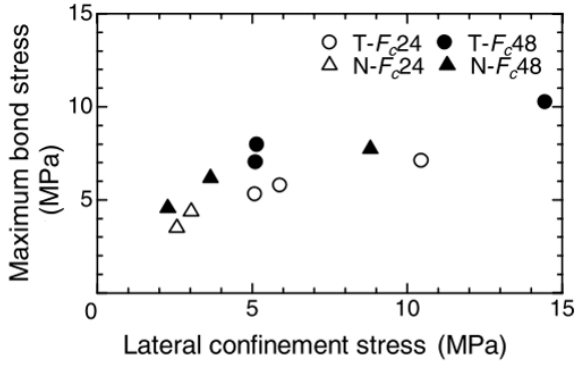


Figure 4 – Maximum bond stress versus lateral confinement stress.
Notation: T refers to lateral type rib, N to screw-type rib and Fc to the concrete compressive strength of 24 and 48 MPa. Adapted from Yasojima and Kanakubo (2004).

Harajli *et al.* (2004) attempted to justify this bond behaviour under confinement by claiming that the higher ductility, which is originated from the confinement effect, allows for a higher number of ribs to

resist the pull-out force applied to the reinforcement, thus enabling higher bond stresses to be developed along the embedded length.

#### 2.1.4.2 Rebar geometry

Rebar geometry and its influence on bond behaviour have been a subject of complex study mainly due to the many parameters needed to accurately define the ribs geometry. Such parameters mainly comprehend the transversal rib's height (*a*), spacing (*c*), inclination (*i*), and face angle (*ά*). Figure 5 illustrates a lateral view of a ribbed bar section and identifies its geometrical characteristics.

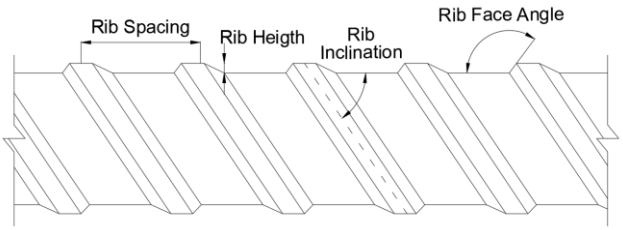


Figure 5 – Geometrical characteristics of ribbed reinforcement, adapted from Lorrain *et al.* (2010).

A valuable parameter used to describe rebar geometry is the relative rib area/bond index ($f_R$) that consists of the ratio of bearing area (projected rib area normal to the bar axis) to the shearing area (bar perimeter times centre-to-centre distance between ribs). The International Standard ISO 15630-1 presents several different formulas for performing the calculation of the parameter, such as the simplified parabola formula presented in equation (1), where $a_m$ refers to rib height at the mid-point, $d$ to the nominal diameter of the bar and $\sum e_i$ to the circumference part of the cross-section of the bar without ribs. Figure 6 illustrates the concepts regarding the bond index's calculation.

$$f_R = \frac{2 \cdot a_m}{3 \cdot \pi \cdot d \cdot c} \cdot \left(\pi \cdot d - \sum e_i\right) \quad (1)$$

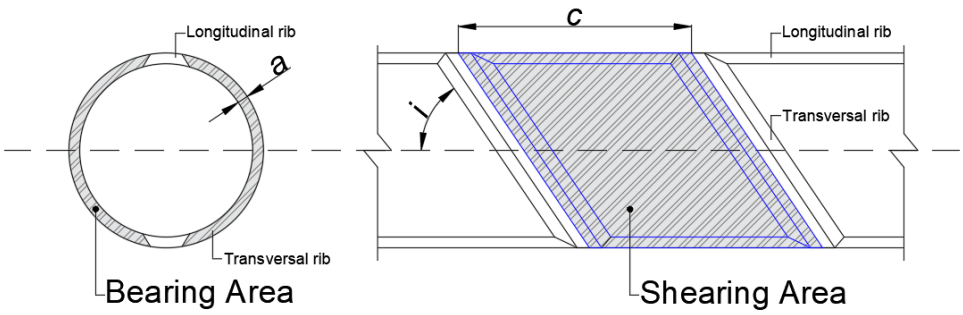


Figure 6 – Concepts regarding the bond index, adapted from ACI 408R-03.

The bond index has been recognised as the most critical rebar geometry parameter influencing bond behaviour, with higher values of $f_R$ leading to better bond performance. Current Eurocode 2 (EC2) specifications determine minimum values of $f_R$ according to the bar's diameter. For example, ribbed bars larger than 12 mm should not have a $f_R$ lower than 0.056.

Darwin and Graham (1993) concluded that greater values of $f_R$ lead to higher bond strength and bond stiffness. The authors also stated that bond behaviour is independent of the rib height and spacing combination used to achieve a given value of $f_R$. Metelli and Plizzari (2014) performed pull-out tests on bars with a wide range of $f_R$ values and observed an increase in bond strength of about 40% when varying $f_R$ from 0.04 to 0.10. Furthermore, the test results were indicative of bars with higher values of $f_R$ having a reduced wedging effect, thus enabling smaller splitting crack widths to occur. The authors also cite Cairns and Jones (1995), who observed similar behaviour. By doubling the $f_R$ value from 0.05 to 0.10, an increase of 30% was obtained in bond strength, the reason being that highly ribbed bars exhibit a lower bursting force on the surrounding concrete. Figure 7, depict the results of Metelli and Plizzari for bond strength versus bond index, with a clear tendency for stresses to increase as $f_R$ also increases.

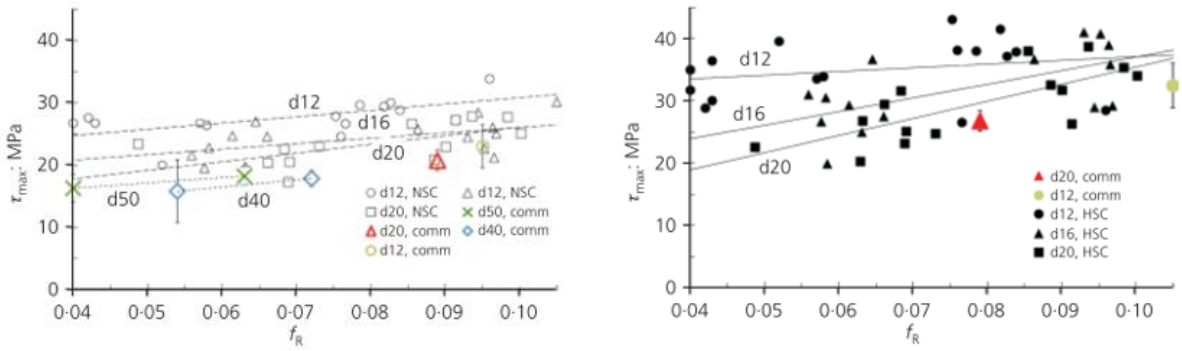


Figure 7 – Bond strength versus $f_R$, adapted from Metelli and Plizzari (2014). Notation: *d* refers to rebar diameter of 12, 16, 20, 40 and 50 mm; *comm* refers to hot rolled commercial bars.

Rebar geometry influence over bond has shown to be related to the level of confinement. Darwin and Graham (1993) documented that bond index variations produced little influence over bond strength when bars lacked confinement by transverse reinforcement or reasonable cover distance. Conversely, bond strength tends to increase with $f_R$ when confinement is properly provided to the reinforcement.

Darwin and Graham (1993) cite several authors that significantly contributed to the knowledge of the influence of rebar deformation patterns on bond behaviour. For example, Clark (1946, 1949) indicated that the rib face angle had an important effect on rebar slippage, with lower angles enabling greater slip values for a given applied load. Later, Lutz and Gergely (1967) point out that the rebar slip action has the effect of crushing the concrete present in front of the ribs, thus producing an effective rib angle of 30 to 40º, making it such that the concrete debris assists the ribs in the wedging effect. Skorogobatov and Edwards (1979) supported this conclusion by testing bars with face angles of 48.5 and 57.8º and realizing that bond strength remained unaffected by these high values because the crushed concrete flattened the rib face angle to an effectively lower angle. Soretz and Holzebein (1979) added that angles superior to 40º do not translate into higher bond strength, while Lutz *et al.* (1966, 1967) claim that angles below 30º result in the softening of the load-slip relationship. Soretz and Holzebein also observed that, although lower values of rib face angle equate to larger slippage, bond strength remains mostly unaffected, with bars of equal rib height but steeper face angles having similar peak stress values. Findings by Darwin and Graham (1993) on the testing of bars with a wide range of rib face angles and

subsequent effective angles support the statement of no clear relation between the bond strength and the rib face angle.

Hamad (1995) performed pull-out and beam splice tests on bars with specially designed rib geometries, with varying rib face angle values of 30, 45, 60, 75 and 90º. Of all the specimens involved in both testing procedures, the ones containing bars with a rib face angle of 60º were the ones that exhibited greater bond strength/load capacity and a stiffer load-slip/load-deflection curve. Improvement of bond strength caused by the increase in rib face angle proved to be marginal, with the ultimate load at failure of pull-out specimens increasing around 10% when the angles varied from 30 to 60º. In beam splice tests, a variation of the angle value from 45 to 60º only caused a 7% rise at the ultimate load.

Regarding rib inclination, Soretz and Holzebein (1979) observed that ribs inclined more perpendicularly to the rebar axis would produce a higher bond strength. However, it is also stated that the improvement is relatively minor. For example, Cairns and Jones (1995), cited by ACI Committee 408 (2003), and Lorrain *et al.* (2010) observed no significant influence of this parameter on bond behaviour.

Although rebar geometry influence over bond behaviour focuses mainly on the characteristics of the transversal ribs, longitudinal ribs have also shown relevance. Darwin and Graham (1993) and Cairns and Jones (1995) reported that longitudinal ribs positioned parallel to the splitting cracks' plane achieved higher bond strength values than when positioned transversally. Darwin and Graham speculate that with longitudinal ribs aligned with the failure plane, transversal ribs will have more surface area to bear on the concrete, thus improving bond performance. Lastly, Wassouf *et al.* (2015) compared test results of bars with two and four longitudinal ribs, with the latter ones reaching worse results, showing a decrease in normalised bond strength of 6% (i.e. bond strength normalised by the characteristic compressive strength of concrete raised to the power of $2/3$). The justification can be linked to the reduced transversal ribs' surface area, which decreases interlock and friction. Furthermore, bars with a higher number of longitudinal ribs showed a lower tendency to fail by splitting.

#### 2.1.4.3 Rebar diameter

In ribbed reinforcement, the size effect influence over bond behaviour is not easy to evaluate, given the complex bond-related phenomena responsible for the transverse cracking of the concrete, wedging effect between ribs and concrete, and the splitting of the concrete cover. (Louro 2014) Nonetheless, Metelli and Plizzari (2014) performed pull-out tests in ribbed bars, and the results registered a drop in bond strength of up to 25% and a drop in bond tangent stiffness greater than 70% when comparing diameters ranging from 12 to 50 mm. This tendency for the decrease in bond strength with the increase in diameter is explicitly shown in the previous Figure 7. Similarly, Turk *et al.* (2003) performed lap-splice tests and registered a decrease in bond strength when using ribbed bars with a larger size, although a significant ductility increase was also verified. Bamonte and Gambarova (2007) conducted experiments in cylindrical specimens, subjecting them to either a pull-out or a push-in force, and compared the obtained results with those of Eligehausen *et al.* (1983) and Soroushian and Choi (1989). The compared results are presented in Figure 8, with bond strength decreasing with increasing diameter.

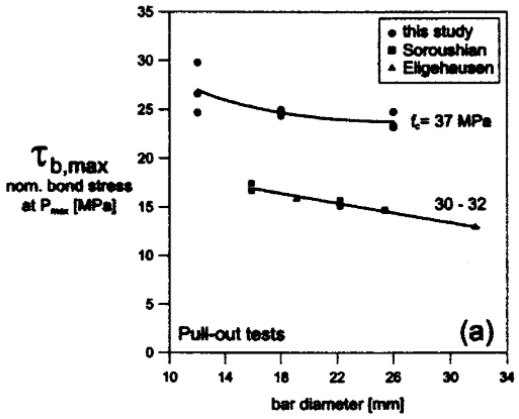


Figure 8 – Bar diameter versus bond strength, adapted from Bamonte and Gambarova (2007).

Ichinose *et al.* (2004) performed pull-out and lap-splice tests, and the results showed, in addition to the behaviour observed in other studies, that confinement levels have a relevant role in how detrimental the effect of larger sized bars is on bond behaviour. By increasing the concrete cover and adding transverse reinforcement, the loss of bond strength due to the size effect was less prevalent than in specimens with low confinement levels.

Current design codes already consider the adverse effects of bar diameter on bond strength. For example, in EC2, a reduction in the design value of bond strength is expected when using a diameter greater than 32 mm. In turn, *fib* Model Code 2010 is even stricter, with 25 mm being its limit size.

#### 2.1.4.4 Loading rate

Loading rate can be described as the speed at which a load is applied or, equivalently, the rate of the imposed displacement. The loading rate at which a pull-out force is applied to reinforcement embedded in concrete influences the bond stress results obtained from experimental campaigns. *Eligehausen et al.* (1983) state that bond strength increases with an increase in loading rate. Test results showed that changing the rate by a factor of one hundred resulted in increased bond strength by about 15%. The authors also compared their experimental results with Hjorth (1976) and Tassios (1979). Figure 9 presents this comparison, showing a tendency for increased bond stress with the increase in pull-out slip rate.

Vos and Reinhardt (1982) conducted impact bond tests in several types of reinforcement and concluded that an increase in loading rate led to higher bond strength and bond stiffness on ribbed bars. This tendency, however, was not so evident in the case of plain bars. It was also observed that the increase of bond stress due to the loading rate variation is more prominent in lower quality concrete and for the lower values of slip.

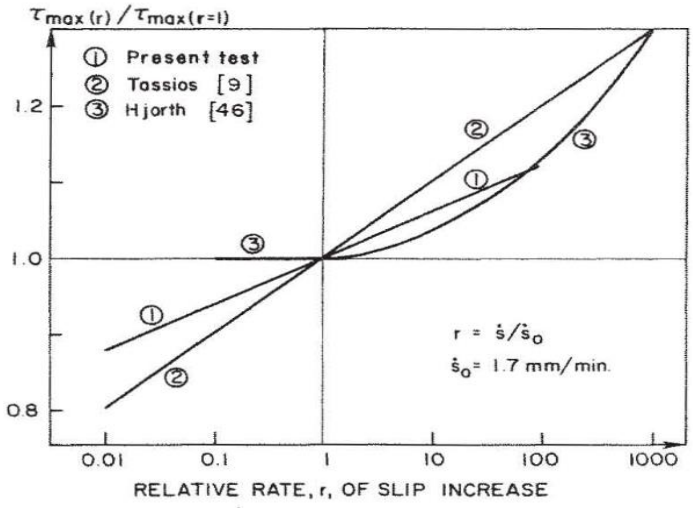


Figure 9 – Influence of the relative rate of the slip increase over bond resistance, adapted from Eligehausen *et al.* (1983).

Pull-out testing performed by Li *et al.* (2015) on confined and unconfined specimens with plain bars showed that bond strength increases with the loading rate in this type of reinforcement. Furthermore, the authors refer that the effects of loading rate variation are affected by the confinement levels. The loading rate effect was minimal when no confinement was provided, while specimens with lateral pressure applied showed increased bond strength and residual bond stress values. According to *Li et al.* (2016), when testing ribbed bars subjected to lateral pressure, bond strength and corresponding slip values increased and decreased, respectively, with the increase in loading rate. Moreover, in the tested diameters of 12, 16 and 22 mm, the level of increase of bond strength tended to decrease with higher concrete strength and larger sized bars. Conversely, bars with larger diameter sizes tended to be more susceptible to the decrease in the value of slip corresponding to the peak bond stress. Overall, the shape of the bond stress-slip curve remained unaffected by the loading rate in both types of reinforcement.

More recently, Long *et al.* (2020) identified two mechanisms supposedly responsible for the increase in the bond strength that results from a higher loading rate. Said mechanisms are the rapid development of slip between steel rebar and concrete and the inertia effect induced by high strain rates at the loaded end. The first one only increased the bond strength at the elastic range of the reinforcement, whilst both were dominant after the yielding of steel.

## 2.2 Bond of steel reinforcement embedded in recycled aggregate concrete

Recycled aggregate concrete is a material used in reinforced concrete structures, where the natural aggregate (NA) content of the concrete mixture is replaced by recycled aggregate (RA) produced from construction and demolition waste (CDW). After a series of treatments, such as particle homogenization, grinding, sieving, and autogenous cleaning (Pepe *et al.* 2014), used concrete is transformed into RA,

which is subsequently used to replace, totally or partially, the NA used in ordinary concrete (OC), thus producing recycled aggregate concrete (RAC).

As the various treatment options for CDW currently used to produce RA do not entirely separate the original NA from the enveloping adhered mortar, the introduction of RA into the concrete mix modifies, to a certain extent, both fresh and hardened concrete properties (Chiriatti *et al.* 2018). The adhered mortar has hydrated and dehydrated cement particles as well as fine aggregate particles, which affect the properties of RA, such as density and water absorption. Thus, removing the adhered paste is required to minimize these adverse property changes.

Several methods are currently available to improve the quality of recycled coarse aggregates (RCA), such as nitric acid dissolution, freeze-thaw, thermal expansion and mechanical methods. Butler *et al.* (2011) and Pandurangan *et al.* (2016) reported on the effectiveness of these various treatments in removing the adhered paste and improving the bond of embedded steel reinforcement. Butler declared that the thermal treatment was more effective at removing the adhered mortar than the freeze-thaw and acid methods. Conversely, Pandurangan *et al.* claim that the thermal treatment is the least effective compared to the acid and mechanical methods, with acid dissolution being the most effective. Furthermore, the authors observed that the bond strength of RAC treated with acid, mechanical and thermal methods was 96, 90 and 74% of that of OC, respectively. Regardless of the adopted treatment method, the compressive strength of RAC made with treated aggregates was around 95% of that of OC, whereas untreated aggregates resulted in lower values of around 86%. Although the acid treatment was the best at improving the bond strength of RAC, Pandurangan *et al.* recommend the mechanical method as the best treatment since it is the most eco-friendly, the less time consuming and the most inexpensive option.

Regarding the influence of the compressive strength of RAC over bond behaviour, similarly to OC, higher compressive strength relates to having higher bond strength, as showcased by Kim *et al.* (2015) and Kim and Yun (2013). Kim *et al.* (2015) also underline that as the compressive strength increases, its influence over the bond strength decreases. In Figure 10, a comparison of various studies is presented for the bond strength of RAC and OC specimens, whilst accompanied by the prediction lines of several bond models. In general, all results satisfy the conservative predictions given by the models, indicating that OC bond models can reasonably predict the bond behaviour of RAC. Furthermore, several authors have suggested that the design formulae provided by current codes to calculate the anchorage length of ribbed bars embedded in OC of normal strength can be adopted for a conservative calculation of the anchorage length for RAC under the condition of the same compressive strength. (Xiao and Falkner 2007; Breccolotti and Materazzi 2013; Prince and Singh 2013, 2014; Lv *et al.* 2018)

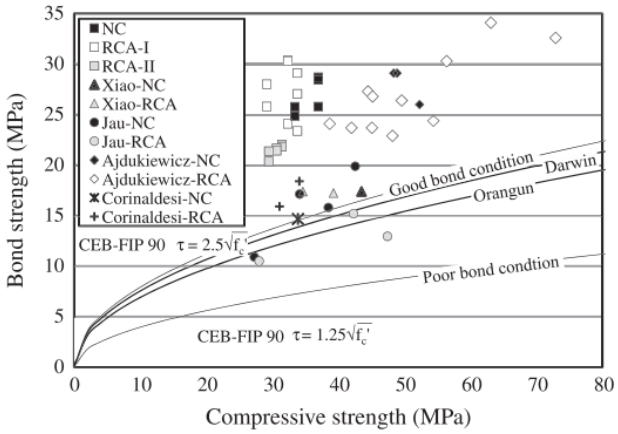


Figure 10 – Bond strength versus compressive strength, adapted from Kim and Yun (2013).

Fernandez *et al.* (2016) highlight that RAC with similar compressive strength to OC tends to have higher bond strength. According to Xiao and Falkner (2007), RAC can achieve bond strength values higher than OC due to the similar elastic modulus of the RCA and of the cement paste, which in turn leads to the improvement of the composite action between these two phases at a microstructural level, thus reducing deformation incompatibilities under applied loads. In contrast, Prince and Singh (2013) postulate that it is due to the RCA particles' better internal curing action. In their work, RCA particles used in the saturated and surface-dry moisture state (SSD) had a water absorption six times higher than that of natural coarse aggregate. As a result, RCA particles can maintain a steady release of water during the internal curing process as the need arises for hydration or to replace moisture lost through evaporation or self-desiccation. Hence, this is expected to help improve the cement hydration, the integrity of the contact zone between the RCA particles and the concrete matrix as well as significantly reduce the permeability, thus producing a stronger concrete with a higher quality paste. The improved integrity and mechanical properties of the concrete conglomerate are then expected to enhance bond strength.

When comparing POT specimens with the same compressive strength, Xiao and Falkner (2007) observed that RAC with a replacement percentage of RCA (RCAr) of 100% had higher bond strength than OC. This effect might be associated with the increased friction resulting from the rougher surface of RCA or even the better internal curing action resulting from RCA being used in an SSD. However, other studies have presented contrary results regarding the relation between RCAr and bond strength. For instance, Xu *et al.* (2018) observed that the highest bond strength occurred in RAC with 60% RCAr. In turn, Seara-Paz *et al.* (2014) observed that increasing RA content leads to a decline in bond strength as high as 27%. Additionally, RAC specimens with lower compressive strength suffered smaller drops in bond strength than OC specimens. Dong *et al.* (2019) also found that bond strength tends to decrease with increasing RCAr, with specimens with a lower water-cement ratio (w/c) suffering a smaller reduction.

When comparing specimens with different values of compressive strength, the relative bond strength (i.e. the maximum bond stress normalised with the respective concrete compressive strength) has shown to increase with higher values of RCAr, as shown by Kim and Yun (2013) and Prince and Singh

(2013, 2014). Prince and Singh attribute this effect to the RCA particles in the SSD, producing a higher quality cement paste. Figure 11 presents a comparison of the results from Xiao and Falkner (2007), Kim and Yun (2013) and Prince and Singh (2013, 2014). The various best-fit lines with positive slopes help support the argument that RCA content influences bond behaviour. (Note: Prince and Singh state that unidentified casting-related difficulties might have caused the discrepancy of the 8 mm diameter results.)

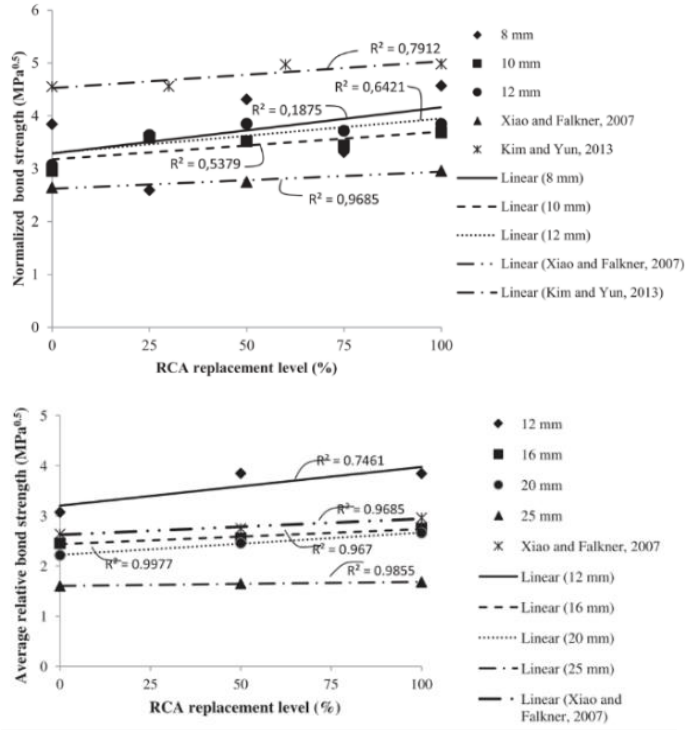


Figure 11 – Relative bond strength versus RCAr, adapted from Prince and Singh (2013, 2014).

When considering the bond behaviour under the condition of equivalent mixture ratio, evidence from studies has not been conclusive. For example, Xiao and Falkner (2007) observed that the bond strength of plain bars decreases with an increase in RCAr, whereas no obvious relation was noted for the case of ribbed bars. However, Butler *et al.* (2011) observed that the bond strength of OC was 9 to 21% higher than that of RAC. Furthermore, according to Moallemi Pour and Alam (2016), the bar diameter and the ratio of embedded length to bar diameter presented an inverse relation to the bond strength of RAC, while larger cover distances helped to improve bond performance. The authors also highlight that the RAC specimens with 30% RCAr presented the closest bond strength values compared to OC.

Kim and Yun (2013) argue for the influence of RCA size over the bond strength of RAC. Under the same RCAr, pull-out test specimens made with RCA of greater maximum size had lower bond strength and greater slip values. The authors claim that since the shape of RCA is generally spherical, proper settlement of the aggregates may be impaired by the RCA of larger size, which can lead to segregation problems. Moreover, results showed that RAC made with larger aggregates had non-uniformly distributed bond stresses along the bar's embedded length. Also, the RAC compressive strength was slightly higher for RCA of smaller grain size, which can be related to this type of aggregate's capacity to produce concrete with fewer air voids.

Concerning the use of recycled fine aggregates (RFA), researchers have advised about their potentially harmful effects on bond performance. For example, Dong *et al.* (2019) observed a decrease in bond strength as high as 37.6% when the replacement percentage of RFA (RFAr) increased from 0 to 100%, with Figure 12 showing the bond stress-slip curves resultant from the beam tests performed by the authors.

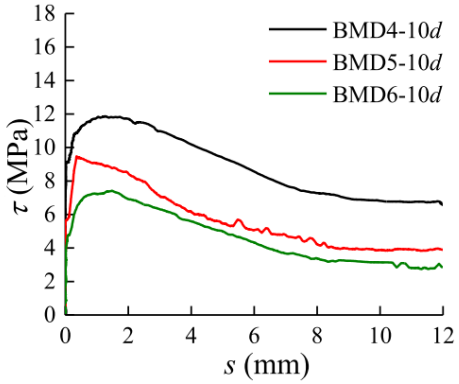


Figure 12 – Bond stress-slip curves of beam specimens with varying RFAr.
Notation: BMD4, BDM5 and BDM6 refer to RFAr equal to 0, 50 and 100%, respectively, whereas 10d refers to a bar diameter of 10 mm. Adapted from Dong *et al.* (2019).

Kim and Yun (2014) performed pull-out tests on specimens made with RFA owning different percentages of water absorption: RFA-A with 6% and RFA-B with 8%. The results showed that higher water absorption makes bond behaviour more susceptible to the effects of RFA content, with the RFA-B specimens achieving lower bond strength values for increasing RFAr. In turn, RFA-A showed no significant effects of RFAr over bond strength up until 60%.

Similar to the case of OC, the lateral confinement pressure provided to RAC exerts a positive influence over the bond behaviour, as is reported by Shang *et al.* (2017). Furthermore, Lv *et al.* (2018) state that the effects that the inclusion of RCA in concrete may have on bond strength are far less noticeable when proper confinement is provided. The authors noticed that the bond strength of unconfined RAC pull-out specimens was slightly higher than that of OC, whereas, for confined specimens, RCA's influence over bond behaviour was insignificant.

## 2.3 Bond of steel reinforcement embedded in low binder concrete/low cement and recycled aggregate concrete

Low binder concrete can be described as an ecological concrete, where the quantity of cement present in the concrete mixture is lower than the minimum value recommended in Annex F of NP EN 206-1, i.e. lower than 260 kg/m$^3$. If this type of concrete incorporates RA into its mixture design, it can be renamed low cement recycled aggregate concrete.

One way to measure the concrete's environmental sustainability is through cement efficiency, which refers to the relationship between the cement content (in mass) used in a concrete mix design and its

performance (e.g. the change in compressive strength associated with a one-unit increase in the mass of cement). (Hayles *et al.* 2018) Cement efficiency can be increased mainly by reducing its quantity in the concrete mixture while retaining its properties. Replacement of Portland cement in concrete can hence be achieved in one of two ways: (i) by substituting clinker, during its fabrication process, for other materials or (ii) by interchanging the cement, during the mixing of fresh concrete, with another binder material or fine filler. (Fennis 2011) Furthermore, other procedures can be adopted to increase cement efficiency, such as particle size optimization, using high reactive/high strength cement, reducing the water content or using suitable superplasticizers. (Robalo *et al.* 2020, 2021)

In standard concrete mixture designs, the cement content used is typically high and is selected empirically as a function of the consistency targeted (i.e. slump), w/c needed to build a required strength and the maximum size and volumetric amount of the coarse aggregate. There is no thorough evaluation and selection of the material's particle size distribution (PSD). (Yousuf *et al.* 2019) Most of the studies that aim to lower the required cement content or optimise concrete properties during fabrication highly value the optimization of the aggregate's PSD. Optimizing the aggregate's PSD involves selecting the particles in the correct sizes and quantities to minimise the volume of voids in the concrete matrix, thus increasing the concrete's packing density. The packing density (i.e. the ratio of the volume of solids to the sum volume of solids and voids), when optimised, can guarantee a sustainable concrete with the lowest possible amount of binder content whilst maintaining the desired level of workability and mechanical performance. (Long *et al.* 2017) The main factors that affect the concrete's packing density are the particles' size, shape and volume, the distance between particles and their electrostatic interactions. (T. de Grazia *et al.* 2019) Presently there are several particle optimisation methods, which can be divided mainly into three groups: (Fennis and Walraven 2012; Zuo *et al.* 2018)

i. Optimisation curves. The concrete components are adjusted so that the total PSD closely resembles an ideal curve's shape. Some of the currently used ideal curves are the Fuller, the Andreasen & Andersen and the Funk & Dinger curves;
ii. Particle packing models. These consist of analytical models, which calculate the mixture's theoretical packing density based on the PSD and packing density of different mean sizes of the mix's particles. In addition, various packing models exist, such as the Furnas model, the compressible packing model, and the 3-parameter model.
iii. Discrete element models. A virtual particle skeleton is built according to the PSD input in the discrete element model to simulate the packing properties and concrete mixtures' flowability. Examples of these models are the one used by Zheng and Stroeven (1999) and the HYMOSTRUC model.

According to Robalo *et al.* (2021), it is possible to produce concrete with suitable compressive strength at 28 days for structural applications, with only 250 kg/m$^3$ of powder in the paste and cement content of 75 to 125 kg/m$^3$. Moreover, it is crucial to achieve high compactness on LBC mixtures to increase their mechanical properties and obtain an adequate performance compared to OC. For example, Freitas (2016) observed an increase of 24% in the compressive strength at 28 days of an LBC mixture

containing 250 kg/m$^3$ of binder powder and 125 kg/m$^3$ of cement content by increasing the packing density by 1%.

As stated by Costa and Appleton (2002), the incorporation of pozzolanic additives into the concrete mixture can increase the packing density of the concrete matrix due to their reactivity with the calcium hydroxide released by the hydration process of the cement, hence resulting in a higher content of hydrated calcium silicates. As a result, the more compact cement paste demands lesser water quantities, which is widely associated with higher compressive strength values. Niu *et al.* (2002) add that the compressive strength increases with the pozzolanic surface area. However, increasing the pozzolanic content above an optimal level decreases the strength due to the higher need for water to keep the consistency. Furthermore, according to Pala *et al.* (2007), the incorporation of fly ash into the concrete mixture reduces the concrete's early compressive strength, increasing it in the long term; however, the contrary effect was noted by the addition of silica fume, which enabled a more rapid gain of compressive strength but achieved lower values later on.

The bond of steel reinforcement embedded in LBC or LCRAC is a relatively recent topic of study that remains mostly not investigated. The two recent studies that approach the subject are those of Freitas (2016) and Pereira (2019), with both authors resorting to pull-out tests to evaluate bond behaviour. Freitas investigated the bond of steel/stainless steel reinforcement embedded in LBC, whereas Pereira studied the bond of steel reinforcement embedded in LBC and LCRAC.

Both studies agreed that the packing density is an essential parameter for bond performance. According to Pereira, an increase in packing density increases bond strength and the stiffness of the bond stress-slip curve's ascending branch. For example, for an increase in the packing density of 0.04, the average bond stress of LBC mixtures increased by 79%. Furthermore, as Freitas's results show, for specimens with equal packing density, the bond strength tends to increase with the increase in compressive strength. However, when comparing an LBC mixture with a 0.86 packing density and 31.9 MPa compressive strength to its control mixture, which had a 0.81 packing density and 38.4 MPa compressive strength, the decrease in packing density led to a decrease in bond strength, even though the compressive strength increases.

On the subject of rebar geometry and size, both authors agree that the increase of the bond index positively influences bond strength. Moreover, Freitas adds that the bond strength of bars with equal values of bond index is higher for those with higher rib height. Lastly, Pereira denotes that the increase of rebar diameter is detrimental to the bond performance of LBC and LCRAC, as it is also in the case for OC.

Regarding LCRAC mixtures, bond performance tends to be negatively influenced by the increasing content of RA. The decrease in bond strength is due mainly to the incorporation of RA of size inferior to the rib spacing, which is explained by the RA's lesser strength comparatively to NA, which compromises the mechanical interlock. Thus, the incorporation of RA in these types of concrete should focus mainly on the coarser sizes. Nonetheless, the aggregate’s PSD revealed no significant influence over bond behaviour. (Pereira 2019)

# 3. Calibration of the bond stress-slip relationship

## 3.1 Introduction

The present section describes the calibration process of an optimized bond stress-slip model regarding the local bond behaviour in good bond conditions and with a pull-out ductile failure. Through the analysis of the existing bond models presented by several authors and the data from pull-out test experiments performed on reinforcement embedded in various concrete mixtures, the calibration process aimed to achieve an optimised bond stress-slip model which would be capable of accurately predicting the local bond behaviour of ribbed bars embedded in OC, LBC and LCRAC mixtures.

Numerous experimental investigations have been carried out on bond behaviour under monotonic or cyclic pull-out loading conditions. Some examples are those of Alavi-Fard and Marzouk (2004), Eligehausen *et al.* (1982), Ichinose *et al.* (2004), Kim *et al.* (2015), Kim and Yun (2013, 2014), Li *et al.* (2016), Long *et al.* (2020), Louro (2014), Lv *et al.* (2018), Metelli and Plizzari (2014), Moallemi Pour and Alam (2016), Prince and Singh (2013, 2014), Seara-Paz *et al.* (2014), Shang *et al.* (2017), Shen *et al.* (2016), Xiao and Falkner (2007), Yanweerasak *et al.* (2018), Yasojima and Kanakubo (2004), Yoo and Shin (2018) and Zuo and Darwin (1998, 2000). However, most of these studies concern the bond between ribbed bars and OC/RAC. Thus, a knowledge gap exists in the field of study of the influence of newly developed concrete technologies, such as LBC and LCRAC, over the bond behaviour. Furthermore, introducing these ecological concrete types presents novel bond-related factors such as high concrete packing densities and RA contents. Therefore, it is paramount that these new variables be addressed to determine their influence on the behaviour of the bond of embedded reinforcement in concrete.

The existing bond models analysed during the calibration process were those presented in *fib* Model Code 2010, Louro (2014), Freitas (2016) and Pereira (2019). Furthermore, the empirical evidence was provided by the data relative to the total of 138 pull-out tests performed separately by Louro (2014), Freitas (2016) and Pereira (2019). Ultimately, the bond-related parameters investigated during this operation were the concrete compressive strength, the bond index, the packing density, the bar diameter and the RA content. These parameters were chosen because of their strong influence over the local bond behaviour. The influence of these parameters on the local bond behaviour was accounted in the optimized bond stress-slip model by way of coefficients, either newly created or previously existing and calibrated. It should be noted that there was not found in the literature anymore POT campaigns either performed using LBC/LCRAC or performed on OC and where the relevant parameters for this work were appropriately accounted for.

## 3.2 Experimental Data

### 3.2.1 Pull-out test

The experimental studies which support the development of the present work were carried out by Louro (2014), Freitas (2016) and Pereira (2019). Each of these studies involved performing pull-out tests to investigate the influence of several parameters on the local bond behaviour. The pull-out test method consists of a concrete parallelepiped test piece containing a partially embedded reinforcing bar which is tension loaded by a servo-controlled hydraulic machine attached by grips to one end of the reinforcement. In addition, a displacement measurement device is installed to register the rebar slip throughout the test at the other end. Figure 13 illustrates the pull-out test principle described in EN 10080:2005 – Annex D.

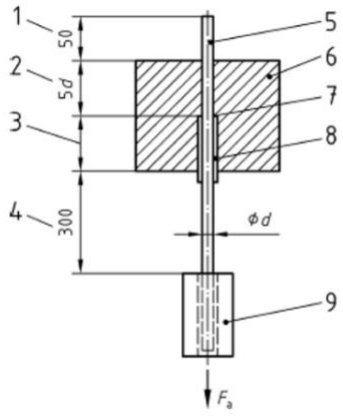


**Key**
1 part of the bar up to the point of application of the displacement measuring device
2 bond length
3 free pre-length 5*d*, min. 200 mm –5*d*
4 part of the bar to the point of application of the tension force
5 reinforcing bar
6 concrete
7 plugging
8 plastic sleeve
9 grip of the testing machine

Dimensions in millimetres

Figure 13 – Pull-out test principle, adapted from EN 10080:2005 – Annex D.

At the end of testing, it is possible to obtain the bond stress-slip relationship curve, thus permitting the evaluation of the local bond behaviour. Given the load values registered by the hydraulic machine, bond stress values for every registered slip value can be calculated and subsequently normalised to the concrete compressive strength following the proposed equations (2) and (3) given by EN 10080:2005 – Annex D and *fib* Model Code 2010, respectively. (Note that equation (2) is only valid for bars with an embedded length of five times the diameter and should be modified in the case of different embedded lengths)

$$\tau_b = \frac{F_a}{5 \cdot \pi \cdot d^2} \quad (2)$$

$$\tau_d = \tau_b \cdot \sqrt{\frac{f_{cm,28}}{f_{cm,j}}} \quad (3)$$

Where,

- $\tau_b$ and $\tau_d$ are the local bond stress and the normalised bond stress according to concrete compressive strength, respectively;

- $F_a$ is the pull-out force;
- $f_{cm,28}$ and $f_{cm,j}$ are the mean concrete compressive strength at 28 days and at $j$ days (age of testing), respectively;

In all the experimental studies, monotonic loading tests were performed under an imposed displacement of 1.7 mm/min, as was first proposed by Eligehausen *et al.* (1983), despite EN 10080:2005 – Annex D suggesting the application of a load at a constant speed $v_p$ (4).

$$v_p = 0.56 \cdot d^2 \quad (\mathrm{N/s}) \tag{4}$$

Adopting the previous formulae would have introduced the loading rate as an undesirable variable given the changes in diameter; moreover, the proposed loading rates could be higher than adequate, promoting tensile loading by impulse, which could lead to the register of higher non-conservative bond stress values. Therefore, the literature considers best the application of a continued imposed displacement until the total rebar slip approaches 20 mm to enable the proper characterisation of bond stresses both in the initial stages and after failure. (Eligehausen *et al.* 1983; Louro 2014)

Regarding the specificities of each study, Louro (2014) conducted an experimental program to study the bond behaviour of ribbed reinforcing bars horizontally positioned in beam-column connection joints to understand the behaviour of critical structural zones of reinforced concrete elements subjected to seismic activity. With such purpose in mind, a modified version of the standard pull-out test specimen specified in EN 10080:2005– Annex D was produced to enable both monotonic and cyclic loading tests. Later, Freitas (2016) studied the bond behaviour of steel/stainless steel reinforcement embedded in LBC by performing pull-out tests under monotonic loading, whereas Pereira (2019) investigated the bond behaviour of steel reinforcement embedded in LBC/LCRAC through standard pull-out tests.

### 3.2.2 Pull-out specimens

The pull-out specimens of Freitas (2016) and Pereira (2019) consisted of cubic concrete test pieces cast with reinforcing bars centred in a horizontal position and extended outside the concrete test piece on both sides, which can be described as the free-end and the loaded-end. Before casting, a plastic sleeve was placed surrounding the bar length that should stay non-bonded to the concrete, with duct tape being positioned at the sleeve's end to block concrete from entering. The bar's non-bonded length helps avoid the overlap of stresses regarding the bond breaking and the contact reactions between the pull-out specimen and the support apparatus, thus ensuring that bond test results go unadulterated. Moreover, the reinforcement's embedded length varied according to rebar size, always maintaining a value of five times the nominal diameter.

In the case of Louro (2014), some modifications were introduced to the test specimens, such as the increase of the embedded length from $5d$ to $6d$ (the advisable limit for the study of local bond behaviour), the inclusion of transverse reinforcement surrounding the main bar's embedded length and two non-bonded lengths at each end of the concrete test piece to enable both monotonic and cyclic loading. Additionally, a plastic film was placed in the bar axis' longitudinal plane to limit the splitting area, thus

emulating the local bond behaviour of bars located in beam-column joints, as suggested by Eligehausen *et al.* (1983).

All specimens were placed in an auxiliary steel apparatus for the testing procedure, with the main reinforcing bar laying vertically, thus keeping the specimens in position during the appliance of the tension force to the bar. In addition, a servo-controlled hydraulic machine was attached by grips to the rebar's loaded end, whereas a displacement measurement device was placed at the free end. Finally, in the cases of Freitas (2016) and Pereira (2019), an additional wooden chock accessory was used to address the height difference between the pull-out specimens and the auxiliary apparatus. Figure 14 presents a general view of the testing systems used by each author, followed by Figure 15 and Figure 16, which present schematic illustrations of the pull-out specimens' layout, with the respective dimensions being presented in Table 1.

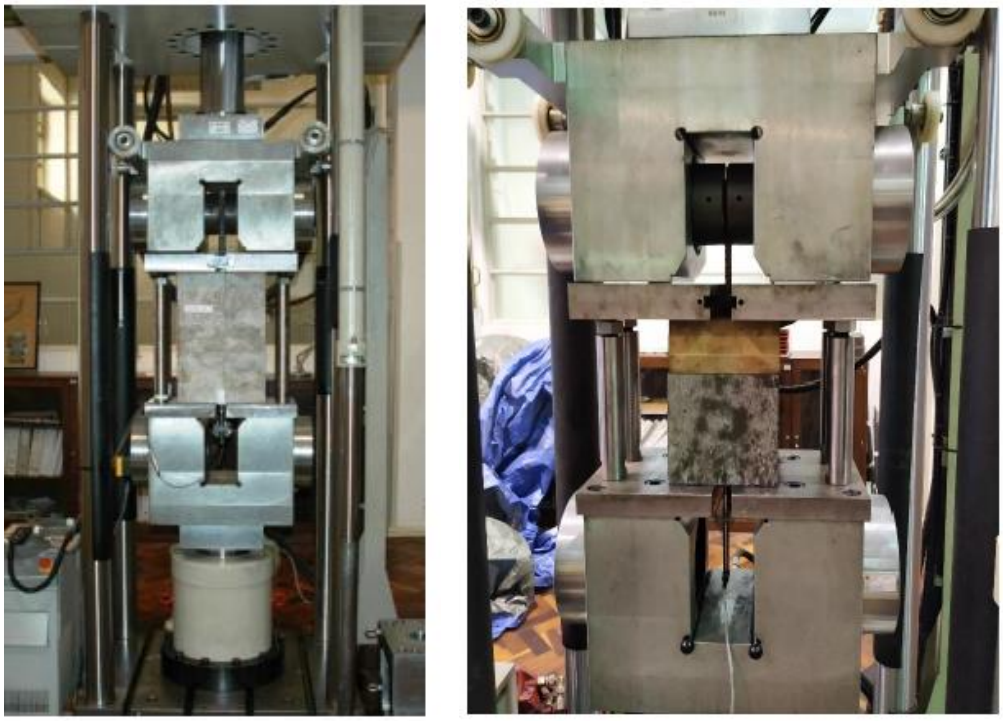

Figure 14 – POT systems as used by Louro (2014) (left) and by Freitas (2016) and Pereira (2019) (right). Adapted from Pereira (2019) and Louro (2014).

Table 1 – Dimensions of the pull-out test specimens. (See Figure 15 and Figure 16).

| *Specimen type* | *d* | *dt* | *b* | *h* | *L* | *l1* | *l2* | *l3* | *l4* | *e1* | *e2* | *e3* | *e4* | | *Embedded Length* |
|---|---|---|---|---|---|---|---|---|---|---|---|---|---|---|---|
| *Standard* | 12 | - | 200 | 200 | 200 | 340 | 140 | 60 | 100 | - | - | - | - | mm | 5*d |
| | 16 | - | 200 | 200 | 200 | 340 | 120 | 80 | 100 | - | - | - | - | | 5*d |
| *Modified* | 16 | 10 | 150 | 195 | 200 | 265 | 100 | 100 | 140 | 80 | 45 | 55 | 10 | | 6*d |
| | 25 | 12 | 215 | 300 | 450 | 265 | 150 | 150 | 140 | 100 | 74 | 86 | 15 | | 6*d |

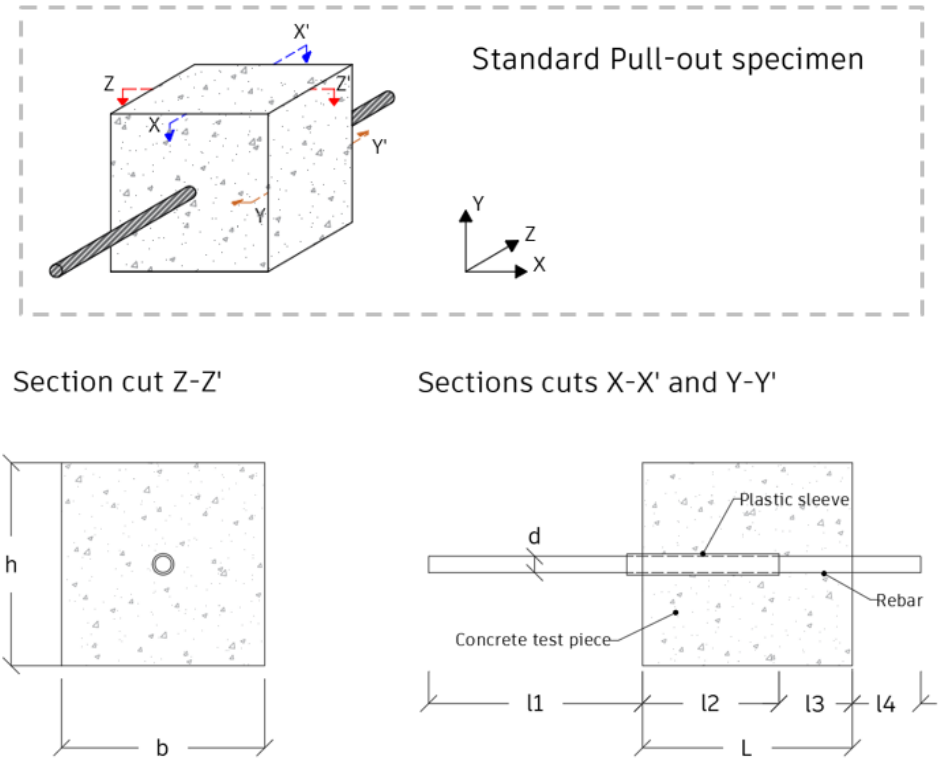


Figure 15 – Schematic of the standard POT specimens, adapted from Louro (2014).

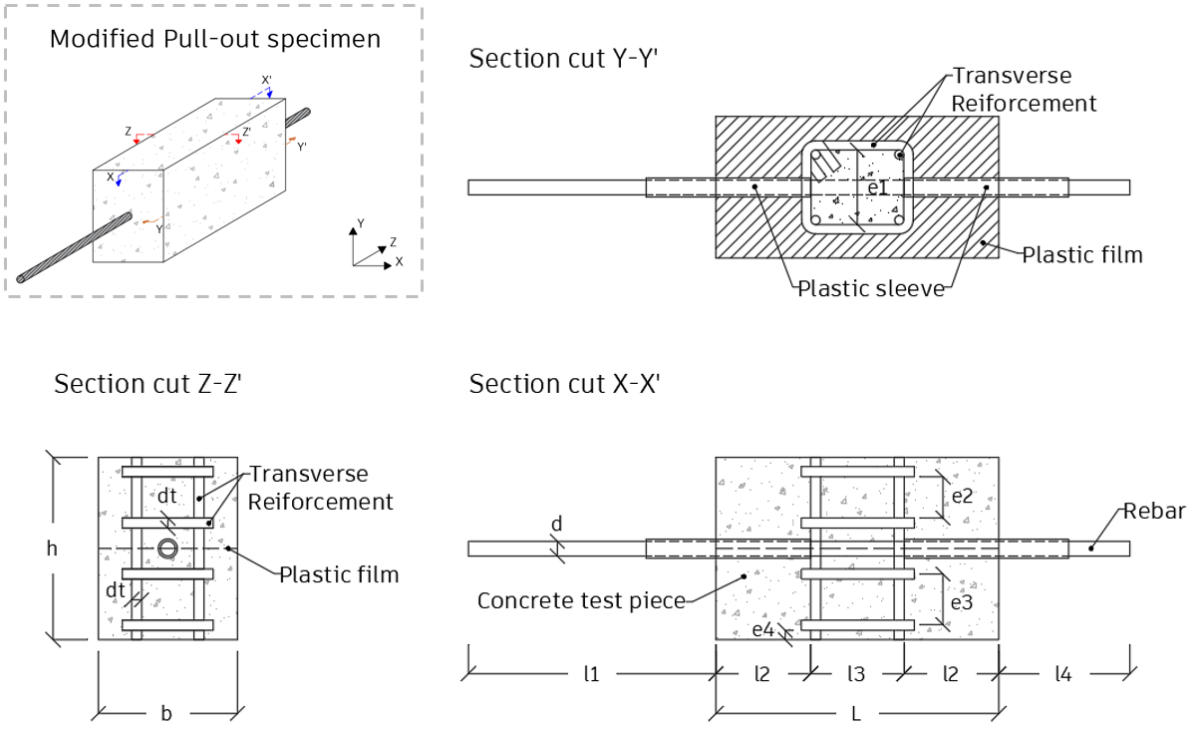


Figure 16 – Schematic of the modified POT specimens, adapted from Louro (2014).

### 3.2.3 Materials

#### 3.2.3.1 Concrete mixtures

Two concrete strength classes were used in the work of Louro (2014) for an adequate representation of the concrete used in Portuguese construction: C30/37 and C50/60 (i.e. typical habitational buildings and bridges/viaducts/buildings of greater relevance, respectively). Four different concrete batches were produced, two for each strength class. All batches were produced using a limestone Portland cement of class CEM II - A/L 52.5 R, with fly-ash being used on just one occasion. In addition, two different admixtures were used to improve the fresh and hardened concrete properties. Lastly, aggregate content was comprised of four types of NA, and the optimisation of the aggregate's PSD was performed through Faury's ideal curve. Table 2 describes the composition of the concrete mixtures used in the experimental campaign carried out by Louro.

Freitas (2016) produced three different concrete mixtures: C250, LBC125 and LBC75. The binder materials used were Portland cement of class CEM I – 52.5 R, limestone-filler, and fly ash. Additionally, the superplasticiser *BASF Glenium SKY 526* was used to reduce the water content. Moreover, four NA types were utilised: fine siliceous sand 0/3 mm, medium siliceous sand 0/4 mm, siliceous gravel 4/8 mm and crushed limestone 6/14 mm. The PSD of all mixtures was optimised using the curve of Funk and Dinger. Table 3 describes the composition of the concrete mixtures produced by Freitas.

Pereira (2019) produced seven different concrete mixtures: four LBCs with various packing density values and packing optimisation curves and three LCRAC mixtures with varying RA replacement percentages. Pereira used two sources of CDW to produce RA and four types of NA. Whereas LBC mixtures contained exclusively NA, LCRAC mixtures had varying RA contents of 30, 55 and 80%. The PSD optimisation was implemented through the Alfred curve for the LBC and LCRAC mixtures, while the corrected Faury's curve was only applied to one of the LBC mixtures. Furthermore, the binder materials included Portland cement CEM I – 52.5 R, limestone-filler and fly-ash. Finally, a superplasticiser commercially named *MasterGlenium SKY 526* was added to all compositions. Table 4 and Table 5 describe the composition of Pereira's LBC and LCRAC mixtures, respectively

Table 2 – Composition of the concrete mixtures of Louro (2014).

| | *Series 1 (C30/37)* | *Series 2 (C50/60)* | *Series 3 (C30/37)* | *Series 4 (C50/60)* | |
|---|---|---|---|---|---|
| *CEM II - A/L 52.5 R* | 348 | 473 | 208 | 472 | kg/m$^3$ |
| *Fly-ash* | 0 | 0 | 111 | 0 | |
| *Admixture 1* | 3.5 | 6.1 | 1.8 | 5.9 | |
| *Admixture 2* | 3.5 | 5.7 | 2.9 | 5.7 | |
| *Crushed Limestone 1* | 789 | 753 | 811 | 751 | |
| *Crushed Limestone 0.5* | 190 | 225 | 214 | 228 | |
| *Coarse Sand* | 412 | 505 | 455 | 520 | |
| *Fine Sand* | 414 | 173 | 422 | 170 | |
| *Water* | 173 | 185 | 136 | 181 | |
| *w/c* | 0.50 | 0.39 | 0.65 | 0.38 | (-) |
| *w/b* | 0.50 | 0.39 | 0.43 | 0.38 | |
| *Packing density* | 0.796 | 0.780 | 0.834 | 0.785 | |
| *Air content* | 2.6 | 2.5 | 2.6 | 2.5 | % |

Table 3 – Composition of the concrete mixtures of Freitas (2016).

| | *OC* | *LBC125* | *LBC75* | |
|---|---|---|---|---|
| *CEM I – 52.5 R* | 250 | 125 | 75 | kg/m$^3$ |
| *Limestone-filler* | 100 | 125 | 75 | |
| *Fly-ash* | 0 | 0 | 100 | |
| *BASF Glenium Sky 526* | 1.00 | 2.50 | 2.30 | |
| *Fine Sand 0/3 mm* | 492.00 | 44.00 | 43.50 | |
| *Medium Sand 0/4 mm* | 427.40 | 1080.10 | 1067.60 | |
| *Gravel 4/8 mm* | 116.40 | 287.20 | 283.90 | |
| *Crushed Limestone 6/14 mm* | 795.40 | 630.60 | 623.30 | |
| *Water* | 169.10 | 117.64 | 117.90 | |
| *w/c* | 0.68 | 0.94 | 1.57 | (-) |
| *w/b* | 0.48 | 0.47 | 0.47 | |
| *Packing density* | 0.81 | 0.86 | 0.86 | |
| *Air content* | 2.00 | 2.00 | 2.00 | % |

Table 4 – Composition of the LBC mixtures of Pereira (2019).

| | *LBC_0,86_Alfred* | *LBC_0,84_Alfred* | *LBC_0,82_Alfred* | *LBC_0,86_Faury* | |
|---|---|---|---|---|---|
| *CEM I - 52.5 R* | 125 | 125 | 125 | 125 | kg/m$^3$ |
| *Limestone-filler* | 0 | 0 | 0 | 0 | |
| *Fly-ash* | 125 | 125 | 125 | 125 | |
| *Master Glenium SKY 526* | 2.8 | 1.5 | 0.3 | 2.8 | |
| *Fine Sand 0/1 mm* | 20.9 | 20.3 | 19.8 | 271.7 | |
| *Medium Sand 0/4 mm* | 1049.6 | 1022.2 | 994.8 | 722.4 | |
| *Gravel 4/8 mm* | 276.1 | 268.9 | 261.7 | 79.3 | |
| *Crushed Limestone 6/14* | 675.5 | 657.9 | 640.3 | 951.9 | |
| *CDW 1/20 mm* | 0 | 0 | 0 | 0 | |
| *CDW 4/20 mm* | 0 | 0 | 0 | 0 | |
| *CDW 10/20 mm* | 0 | 0 | 0 | 0 | |
| *Absorbed water* | 0 | 0 | 0 | 0 | |
| *Effective water* | 117.4 | 138.6 | 159.8 | 117.4 | |
| *w/c* | 0.94 | 1.11 | 1.28 | 0.94 | (-) |
| *w/b* | 0.47 | 0.55 | 0.64 | 0.47 | |
| *Packing density* | 0.86 | 0.84 | 0.82 | 0.86 | |

Table 5 – Composition of the LCRAC mixtures of Pereira (2019).

| | *LCRAC_30* | *LCRAC_55* | *LCRAC_80* | |
|---|---|---|---|---|
| *CEM I - 52.5 R* | 175 | 175 | 175 | kg/m$^3$ |
| *Limestone-filler* | 100 | 100 | 100 | |
| *Fly-ash* | 75 | 75 | 75 | |
| *Master Glenium SKY 526* | 2.1 | 2.9 | 2.6 | |
| *Fine Sand 0/1 mm* | 161 | 169 | 376 | |
| *Medium Sand 0/4 mm* | 645 | 675 | 0 | |
| *Gravel 4/8 mm* | 188 | 0 | 0 | |
| *Crushed Limestone 6/14* | 325.7 | 0 | 0 | |
| *CDW 1/20 mm* | 0 | 0 | 1343.5 | |
| *CDW 4/20 mm* | 0 | 926 | 0 | |
| *CDW 10/20 mm* | 476 | 0 | 0 | |
| *Absorbed water* | 24 | 46 | 67 | |
| *Effective water* | 138 | 137 | 138 | |
| *w/c* | 0.79 | 0.78 | 0.79 | (-) |
| *w/b* | 0.39 | 0.39 | 0.39 | |
| *Packing density* | 0.84 | 0.84 | 0.84 | |
| *RA replacement* | 30 | 55 | 80 | % |

#### 3.2.3.2 Reinforcement

Louro (2014) used B500C steel for the main and transversal reinforcing bars. The main bars were distinguished by their diameter size (16 and 25 mm) and according to their bond index value: batch *A* for low $f_R$ and batch *B* for high $f_R$. Additionally, some bars were exposed to a thermal treatment to lower their yield strength (batches AT and BT). The thermal treatment applied was intended to lower the steel yield strength to study the influence of the yielding over the bond behaviour and had effect over the remaining bond characteristics of the reinforcement. Lastly, the diameter sizes used for the transverse reinforcement were 10 and 12 mm.

Freitas (2016) used either B500C steel or AISI 304/AISI 316 stainless steel ribbed bars of 12 and 16 mm diameter, whereas Pereira (2019) used only B500C bars of 12 mm diameter. Table 6 displays the most relevant mechanical and bond properties of the main reinforcing bars of the various authors.

Table 6 – Mechanical and bond properties of the main reinforcing bars used in the experimental POT.

| | *d (mm)* | *Batch* | *Class* | $f_y$ *(MPa)* | $R_m$ *(MPa)* | $A_{gt}$ *(%)* | *E (GPa)* | $a$ *(mm)* | *c (mm)* | $f_R$ |
|---|---|---|---|---|---|---|---|---|---|---|
| *Louro (2014)* | 16 | A | B500C | 544 | 640 | 13.0 | 197 | 1.29 | 9.97 | 0.081 |
| | | B | | 517 | 611 | 13.0 | 194 | 1.58 | 9.87 | 0.099 |
| | | AT | | 541 | 636 | 13.0 | 187 | 1.28 | 9.95 | 0.080 |
| | | BT | | 444 | 540 | 14.0 | 191 | 1.59 | 9.87 | 0.098 |
| | 25 | A | | 530 | 638 | 10.0 | 191 | 2.22 | 14.35 | 0.096 |
| | | B | | 464 | 570 | 12.0 | 192 | 2.41 | 14.47 | 0.101 |
| | | AT | | 549 | 662 | 11.0 | 198 | 2.27 | 14.37 | 0.097 |
| | | BT | | 473 | 578 | 9.0 | 192 | 2.41 | 14.45 | 0.101 |
| *Freitas (2016)* | 12 | | B500C | 543 | 630 | 13.4 | no data | 1.07 | 7.80 | 0.082 |
| | | | AISI304 | 651 | 757 | 19.8 | | 0.67 | 6.67 | 0.058 |
| | 16 | | B500C | 536 | 633 | 11.2 | | 1.18 | 10.80 | 0.066 |
| | | | AISI316 | 573 | 760 | 28.3 | | 1.06 | 10.18 | 0.066 |
| *Pereira (2019)* | 12 | | B500C | 551 | 671 | 12.0 | 205 | 0.95 | 7.70 | 0.073 |

### 3.2.4 Experimental results and data treatment

Before the calibration process, each author's experimental bond stress-slip results were collected together with the data regarding the bond-related parameters. Table 7 puts together the relevant information regarding the characteristics of each experimental test series performed, and each series is identified by the name given by its corresponding author.

Regarding Louro (2014), the specimens are identified by their reinforcement batch (i.e. A, B, AT or BT), followed by the type of concrete used and lastly, the diameter of the main bar. C1 and C2 refer to the target strength classes C30/37 and C50/60, respectively. It should also be noted that the specimens which involved cyclic loading or where yielding of the reinforcement occurred were excluded from the data considered in the present work.

Freitas's (2016) experimental campaign specimens are identified by the type of concrete (i.e. C250, LBC125 or LBC75), followed by the type of steel and the bar's diameter. In this case, the identifiers *A* and *i* correspond to steel and stainless steel, respectively.

Finally, Pereira's (2019) experimental campaign is divided into LBC and LCRAC concrete specimens. LBC series includes a numeric identifier ranging from 0,82 to 0,86, which is related to their packing density and a second identifier concerning the optimisation packing curves used (i.e. Alfred or Faury). In contrast, LCRAC series are identified regarding the total percentage of RA content.

Regarding the concrete compressive strength data, to convert the $f_{cm,cube}$ values presented by Louro (2014) and Freitas (2016) into $f_{cm}$, the equation (5) was used, following the same criteria applied by Pereira (2019). This harmonisation was necessary since the different bond stress-slip models studied during the calibration process use different compressive strength parameters to calculate bond stress.

$$f_{cm} = 0.82 * f_{cm,cube} \tag{5}$$

Additionally, each author's local bond stress values were normalised according to the same criteria, considering the non-linear influence of the concrete compressive strength over bond behaviour, as is shown in expression (3). This step was also essential since the authors used different criteria for calculating $\tau_d$; whereas Freitas (2016) used the recommendations presented in Annex D of EN 10080 (2005), which indicate the use of $f_{cm,28}/f_{cm,j}$ instead of $\sqrt{f_{cm,28}/f_{cm,j}}$, Louro (2014) and Pereira (2019) followed the recommendations of *fib* Model Code 2010. Afterwards, the mean values of the bond stress-slip curve were calculated for each series, which would serve as the target for the calibration process to be developed.

Table 7 – Characteristics of the POT specimens of each testing series.

| | Test Series | Nº SPEC | d (mm) | $f_{cm,28}$ (MPa) | σ | $f_R$ | c (mm) | a (mm) | $RA_{<c}$ | $RA_{\geq c}$ |
|---|---|---|---|---|---|---|---|---|---|---|
| *Louro (2014)* | A_C1_16 | 3 | 16 | 38.25 | 0.796 | 0.081 | 9.97 | 1.29 | 0.00 | 0.00 |
| | B_C1_16 | 3 | | | 0.834 | 0.099 | 9.87 | 1.58 | | |
| | AT_C1_16 | 3 | | | 0.796 | 0.080 | 9.95 | 1.28 | | |
| | BT_C1_16 | 3 | | | 0.834 | 0.098 | 9.87 | 1.59 | | |
| | A_C2_16 | 3 | | 57.80 | 0.780 | 0.081 | 9.97 | 1.29 | | |
| | AT_C2_16 | 3 | | | | 0.080 | 9.95 | 1.28 | | |
| | A_C1_25 | 6 | 25 | 38.25 | 0.796 | 0.096 | 14.35 | 2.22 | | |
| | B_C1_25 | 6 | | | | 0.101 | 14.47 | 2.41 | | |
| | AT_C1_25 | 3 | | | 0.834 | 0.097 | 14.37 | 2.27 | | |
| | BT_C1_25 | 3 | | | | 0.101 | 14.45 | 2.41 | | |
| | A_C2_25 | 3 | | 57.80 | 0.780 | 0.096 | 14.35 | 2.22 | | |
| | B_C2_25 | 6 | | | | 0.097 | 14.47 | 2.41 | | |
| *Freitas (2016)* | C250_A12 | 5 | 12 | 32.64 | 0.810 | 0.082 | 7.80 | 1.07 | 0.00 | 0.00 |
| | C250_i12 | 4 | | | | 0.058 | 6.67 | 0.67 | | |
| | LBC125_A12 | 5 | | 27.12 | 0.860 | 0.082 | 7.80 | 1.07 | | |
| | LBC125_i12 | 5 | | | | 0.058 | 6.67 | 0.67 | | |
| | LBC75_A12 | 5 | | 17.77 | | 0.082 | 7.80 | 1.07 | | |
| | LBC75_i12 | 5 | | | | 0.058 | 6.67 | 0.67 | | |
| | C250_A16 | 5 | 16 | 32.64 | 0.810 | 0.066 | 10.80 | 1.18 | | |
| | C250_i16 | 5 | | | | | 10.18 | 1.06 | | |
| | LBC125_A16 | 5 | | 27.12 | 0.860 | | 10.80 | 1.18 | | |
| | LBC125_i16 | 5 | | | | | 10.18 | 1.06 | | |
| | LBC75_A16 | 5 | | 17.77 | | | 10.80 | 1.18 | | |
| | LBC75_i16 | 5 | | | | | 10.18 | 1.06 | | |
| *Pereira (2019)* | LBC_0,86_Alfred | 4 | 12 | 29.70 | 0.860 | 0.073 | 7.7 | 0.95 | 0.00 | 0.00 |
| | LBC_0,84_Alfred | 5 | | 20.20 | 0.840 | | | | | |
| | LBC_0,82_Alfred | 5 | | 14.70 | 0.820 | | | | | |
| | LBC_0,86_Faury | 5 | | 26.90 | 0.860 | | | | | |
| | LCRAC_30 | 5 | | 24.50 | 0.840 | | | | | 0.30 |
| | LCRAC_55 | 5 | | 19.30 | | | | | 0.10 | 0.45 |
| | LCRAC_80 | 5 | | 15.50 | | | | | 0.34 | 0.46 |

## 3.3 Bond stress-slip models

Most of the existing bond stress-slip models result from semi-empirical/analytical approaches in which relationships between bond stress and slip are formulated under theoretical hypotheses (e.g. concrete behaving as an elastic material). A prime example of a semi-empirical model is the one proposed by Eligehausen *et al.* (1982), which essentially established a connection between bond stress and rebar slip for monotonic and cyclic pull-out loading. Later on, this model developed into the one currently presented in *fib* Model Code 2010, which establishes a local bond stress-slip relationship for monotonic loading of ribbed bars in the elastic range of steel ($\varepsilon_s < \varepsilon_{s,y}$), and accounts for diferent types of failure, as established in Figure 17.

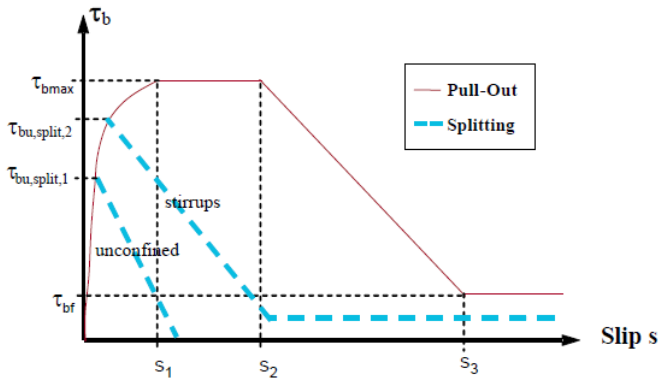


Figure 17 – Bond stress-slip relationship for monotonic loading, adapted from fib Model Code 2010.

The *fib* Model Code 2010 model performs the calculation of the bond stress values $\tau_b$ according to the diferent stages of the bond stress-slip curve, as shown by the expressions (6), (7), (8) and (9). Additionally, each of the referenced parameters varies according to the different conditions presented in Table 8 regarding the type of failure, the bar's bond conditions and the confinement level provided by the transverse reinforcement.

$$\tau_b = \tau_{bmax} \cdot \left(\frac{s}{s_1}\right)^{\alpha}, \qquad for\ 0 \le s \le s_1; \tag{6}$$

$$\tau_b = \tau_{bmax}, \qquad for\ s_1 \le s \le s_2; \tag{7}$$

$$\tau_b = \tau_{bmax} - \left(\tau_{bmax} - \tau_{bf}\right) \cdot \frac{s - s_2}{s_3 - s_2}, \qquad for\ s_2 \le s \le s_3; \tag{8}$$

$$\tau_b = \tau_{bf}, \qquad for\ s_3 < s; \tag{9}$$

Where,

- $\tau_b$ is the bond stress;
- $s$ is the slip;
- $\tau_{bmax}$ is the bond strength for the pull-out failure;
- $\tau_{bu,split,1}$, $\tau_{bu,split,2}$ are the bond strength for the splitting failures (without and with confinement), respectively;
- $\tau_{bf}$ is the reference residual bond stress due to bond friction;
- $s_1, s_2$ and $s_3$ are the slip for the beginning and end of the bond strength plateau and the beginning of the residual bond stress, respectively;
- $f_{cm}$ is the mean concrete compressive strength;
- $c$ is the clear distance between ribs (i.e. rebar rib spacing);
- $\alpha$ is the coefficient that characterizes the $\tau_b - s$ relationship of the ascending branch.

Based on the conditions defined by *fib* Model Code 2010 for bond behaviour of bars with a pull-out failure and good bond conditions, several authors have proposed new models that incorporate coefficients that account for the influence of several parameters well-known in the literature to influence the bond behaviour. For example, Louro (2014) proposed a model which accounts for the influence of

high bond index bars, whereas later, Freitas (2016) proposed a model with coefficients to take into account the influence of the bond index and packing density over the bond behaviour of steel/stainless steel reinforcement embedded in OC/LBC. Subsequently, Pereira (2019) proposed a bond stress-slip model which considers the influence of the bond index, the packing density and the RA content of size inferior to the rib spacing over the bond behaviour of steel reinforcement embedded in OC/LBC/LCRAC. Table 9 displays the various parameters and coefficients of the aforementioned bond models. These models, along with the one prescribed in *fib* Model Code 2010, supported the calibration process of the present work to achieve a calibrated bond stress-slip model for the local bond behaviour of embedded steel in OC/LBC/LCRAC.

Table 8 – Parameters of the bond stress-slip model for ribbed bars presented in *fib* Model Code 2010.

| | ***Pull out failure*** | | ***Splitting failure*** | | | |
|---|---|---|---|---|---|---|
| | $\varepsilon_s < \varepsilon_{s,y}$ | | | | | |
| | Good bond conditions | All other bond conditions | Good bond conditions | | All other bond conditions | |
| | | | unconfined | stirrups | unconfined | stirrups |
| $\tau_{bmax}$ | $2.5 \cdot \sqrt{f_{cm}}$ | $1.25 \cdot \sqrt{f_{cm}}$ | $7.0 \cdot \sqrt[4]{\frac{f_{cm}}{25}}$ | $8.0 \cdot \sqrt[4]{\frac{f_{cm}}{25}}$ | $5.0 \cdot \sqrt[4]{\frac{f_{cm}}{25}}$ | $5.5 \cdot \sqrt[4]{\frac{f_{cm}}{25}}$ |
| $s_1$ | $1.0\ mm$ | $1.8\ mm$ | $s(\tau_{máx})$ | $s(\tau_{máx})$ | $s(\tau_{máx})$ | $s(\tau_{máx})$ |
| $s_2$ | $2.0\ mm$ | $3.6\ mm$ | $s_1$ | $s_1$ | $s_1$ | $s_1$ |
| $s_3$ | $c$ | $c$ | $1.2 \cdot s_1$ | $0.5 \cdot c$ | $1.2 \cdot s_1$ | $0.5 \cdot c$ |
| $\alpha$ | 0.4 | 0.4 | 0.4 | 0.4 | 0.4 | 0.4 |
| $\tau_{bf}$ | $0.4 \cdot \tau_{máx}$ | $0.4 \cdot \tau_{máx}$ | 0 | $0.4 \cdot \tau_{máx}$ | 0 | $0.4 \cdot \tau_{máx}$ |

Table 9 – Bond models proposed by Louro (2014), Freitas (2016) and Pereira (2019) for the case of pull-out failure and good bond conditions.

| | *Louro (2014)* | *Freitas (2016)* | *Pereira (2019)* |
|---|---|---|---|
| $\tau_{bmax}$ | $\beta \cdot \sqrt{f_{cm,cube}}$ | $2.5 \cdot \sqrt{f_{cm,cube}} \cdot\ k_{f_R} + k_\sigma$ | $2.5 \cdot \sqrt{f_{cm}} \cdot\ \eta_{f_R} \cdot\ \eta_\sigma \cdot\ \eta_{RA_{<c}}$ |
| $\beta \mid k_{f_R} \mid \eta_{f_R}$ | $\begin{cases} 2.65, & if\ f_R > 1.6 \cdot f_{R,min} \\ 2.35, & if\ f_R \le 1.6 \cdot f_{R,min} \end{cases}$ | $\frac{f_R}{0.056}$ | $4.757 \cdot f_R + 0.8785$ |
| $- \mid k_\sigma \mid \eta_\sigma$ | - | $100 \cdot (\sigma - 0.81)$ | $7.927 \cdot \sigma - 5.408$ |
| $- \mid - \mid \eta_{RA_{<c}}$ | - | - | $1 - 0.972 \cdot RA_{<c}$ |
| $s_1$ | $\begin{cases} 0.5, & if\ f_R > 1.6 \cdot f_{R,min} \\ 1.0, & if\ f_R \le 1.6 \cdot f_{R,min} \end{cases}$ | 1.0 | $1.0 - 5 \cdot (\sigma - 0.82), \quad for\ \sigma \ge 0.82$ |
| $s_2$ | $\begin{cases} 1.5, & if\ f_R > 1.6 \cdot f_{R,min} \\ 2.0, & if\ f_R \le 1.6 \cdot f_{R,min} \end{cases}$ | 2.0 | $2.0 - 5 \cdot (\sigma - 0.82), \quad for\ \sigma \ge 0.82$ |
| $s_3$ | $c$ | $c$ | $c$ |
| $\alpha$ | 0.4 | 0.4 | $0.4 - 4 \cdot (\sigma - 0.82), \quad if\ \sigma \ge 0.82$ |
| $\tau_{bf}$ | $0.4 \cdot \tau_{bmax}$ | $0.4 \cdot \tau_{bmax}$ | $0.3 \cdot \tau_{bmax}, \quad for\ LBC/LCRAC$ |
| | | | $0.4 \cdot \tau_{bmax}, \quad for\ OC$ |

## 3.4 Empirical calibration

### 3.4.1 Methodology

The calibration of the optimized bond stress-slip model followed a process of evaluating the influence of several previously documented bond-related parameters to define a set of coefficients. These coefficients would then be incorporated in the expressions for the calculation of the model's parameters of bond strength, residual bond stress and slip values at peak bond capacity, thus predicting the local bond behaviour of OC, LBC and LCRAC in the most accurate way possible. The bond-related parameters considered in the optimised model were the bar diameter, the bond index, the packing density and the RA content, which, as previously mentioned, are the ones that have the greatest influence on the performance of the steel-concrete connection.

It is consensual in the scientific community that the most important parameter of the bond stress-slip relationship is the bond strength, and for its calibration, an iterative method was applied. The method adopted followed the next steps:

1. First of all, the *fib* Model Code 2010 expression for bond strength was multiplied by a set of coefficients $\varphi_j$, as shown in expression (10). Each coefficient had a physical significance and related to the influence of a certain bond-related parameter.

$$\tau_{bmax} = 2.5 \cdot \sqrt{f_{cm}} \cdot \prod_{j=1}^{n} \varphi_j \quad (10)$$

2. The initial expression for each $\varphi_j$ coefficient was either obtained from previous bond models or created through analysis of the experimental data. The goal of the iterative method was to refine the initial expressions of the $\varphi_j$ coefficients by weighing their isolated influence over the data relative to the mean bond strength of each pull-out test series. For example, at the first iteration step, the preponderance of the coefficient $\varphi_1$ is weighed through the calculation performed in the expression (11).

$$\tau_{dmax} = 2.5 \cdot \sqrt{f_{cm}} \cdot \prod_{j=1}^{n} \varphi_j \;<=>\; \varphi_1 = \tau_{dmax} / 2.5 \cdot \sqrt{f_{cm}} \cdot \prod_{j=2}^{n} \varphi_j \quad (11)$$

3. The data regarding the preponderance of the weighed coefficient is gathered, and a graphic containing a regression line of the results is plotted. If the plotted regression line proves to better adapt to the isolated influence of the coefficient than the first (or previous) equation of the coefficient, the equation is 'stored' as the new expression for the coefficient, thus ending the present iteration step.
4. In each following iteration step, the same process is performed for the subsequent coefficient, using an equal process, although taking into account the replacement equation(s) stored for the previous iterated coefficient(s).
5. Once all coefficients have been iterated once, the process restarts until otherwise a pre-established convergence criterion is met.

At each iteration of a given coefficient $\varphi_j$ the goodness-of-fit measure value $R^2$ regarding the plotted regression line tends to converge. Once the differences between $R^2$ values from the previous and the subsequent iteration of all coefficients were equal to or lower than 0.001, then the calibration was deemed complete, as no significant improvement was expected to be obtained. Figure 18 presents a flowchart describing graphically the iterative calibration method employed for the bond strength parameter.

A simpler calibration approach was used for the remaining parameters of the calibrated bond stress-slip model since it was intended that the calculations of the parameters $s_1$ , $s_2$ and $\tau_{bf}$ were to be kept straightforward to promote the use of the optimised model. Furthermore, isolating and identifying the influence of the various material parameters over the aforementioned slip and stress parameters was revealed to be difficult. Therefore, the slip parameters were calibrated considering the rebar diameter size, whereas the residual bond stress was mainly influenced by the concrete type and is directly related to the bond strength. The results of the calibration process and the thought process behind its application are further detailed in the next section.

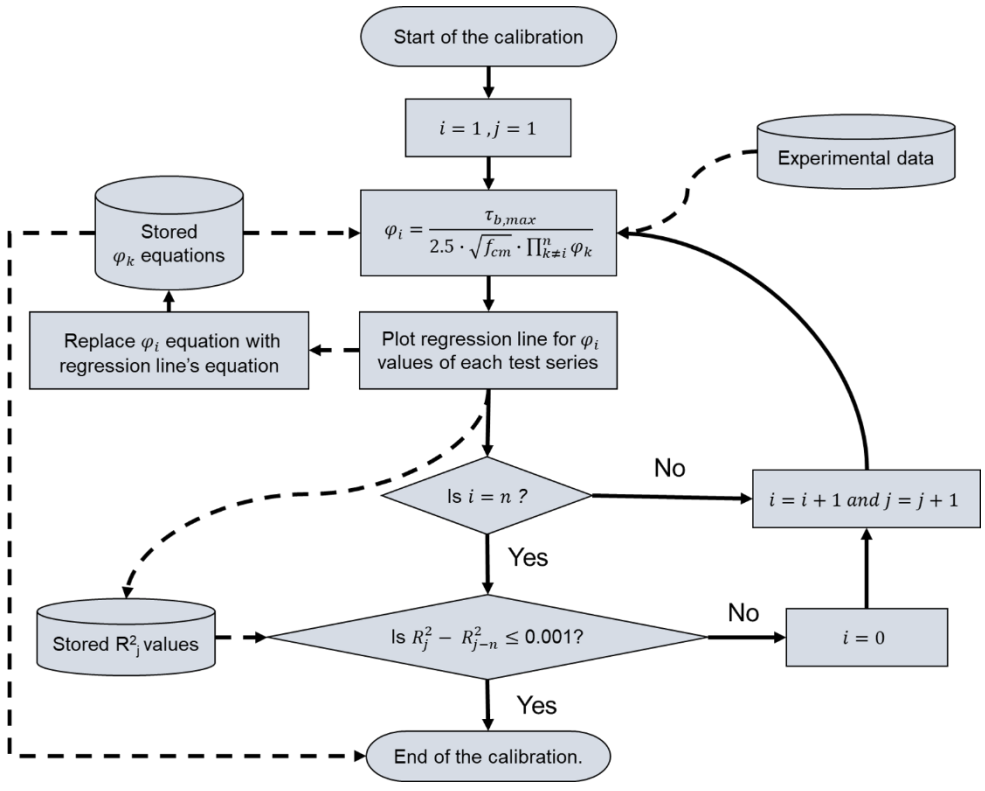


Figure 18 – Flowchart of the iterative calibration process used for the bond strength parameter.

### 3.4.2 Calibration results

#### 3.4.2.1 Bond strength

The present section describes the results of the previously described methodology for the calibration of the bond stress-slip model's parameter. Firstly, by analysing each of the pre-existing bond stress-slip

models and their coefficients, as well as the data regarding the deviation to accuracy error Δ calculated through expression (12), Pereira's (2019) model presents the best coefficients for predicting the bond behaviour of the present set of experimental results.

$$\Delta = \frac{Experimental\ result - Theoretical\ model\ result}{Theoretical\ model\ result} \tag{12}$$

Moreover, the possible addition of a coefficient accounting for the influence of the bar's diameter on the bond behaviour was investigated. As pointed out by several researchers, bond strength decreases when larger-sized bars are considered. (Eligehausen *et al.* 1983, Soroushian and Choi 1989, Turk *et al.* 2003, Bamonte and Gambarova 2007 and Metelli and Plizzari 2014) When calculating bond strength values using Pereira's (2019) model and subsequently measuring the ratio between experimental and theoretical bond strength $\tau_{dmax}/\tau_{bmax}$ for each test series, as expected, a downward tendency was registered with the increase in diameter size. Consequentially, an exercise was performed where the median of the experimental to theoretical ratio values for each bar size group of test series was calculated, which resulted in the formulation of a coefficient for the influence of the bar diameter over bond behaviour. Figure 19 presents the plotted results of this operation, where the equation of a linear regression line was adopted for the new coefficient $\varphi_d$ (see also expression (13)). This coefficient was then integrated in the bond strength expression (14) for Pereira's model (2019) prior to the beginning of the calibration process.

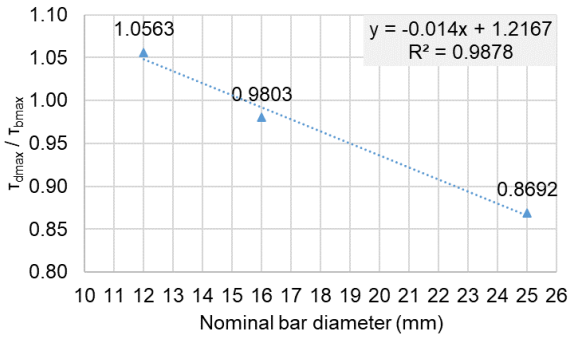


Figure 19 – Formulation of the new coefficient $\varphi_d$: $\tau_{dmax}/\tau_{bmax}$ versus nominal bar diameter.

$$\varphi_d = -0.014 \cdot d + 1.2167 \tag{13}$$

$$\tau_{bmax} = 2.5 \cdot \sqrt{f_{cm}} \cdot \eta_{f_R} \cdot \eta_\sigma \cdot \varphi_d \tag{14}$$

At the start of the calibration of the bond strength parameter using the iterative method, it was important to restrict the data to the test series involving OC/LBC, thus removing the RA content variable from this initial stage and simplifying the operation. Therefore, the order by which the coefficients were iterated was the following: $\eta_{f_R} \rightarrow \eta_\sigma \rightarrow \varphi_d$.

The iteration operations for the coefficient $\eta_{f_R}$ proved to be unsuccessful. Despite various attempts to calibrate being performed (using either linear or second-degree polynomial regression lines), the results proved unfruitful, given their persistent indication of a detrimental effect of increasing $f_R$ values over

bond strength. Such results were refuted given it is well-documented in the literature that increasing $f_R$ improves bond performance; hence, $\eta_{f_R}$ was left unaltered [expression (15)]. The unexpected results could have been caused by factors such as the influence of other bond-related parameters being coupled together with the bond index or possible shortcomings of the devised iterative method. Figure 20 shows the plotted results of the first attempted iteration, with both considered hypotheses failing to produce satisfactory results.

The calibration of the following coefficient, regarding the influence of the packing density, returned much better results. Data analysis revealed that when $\sigma$ increases above 0.83, the bond strength significantly improves, whereas when $\sigma$ is located within the 0.78 to 0.83 range, the effect over bond strength is less prominent. In order to take into account this behaviour, the $\eta_\sigma$ coefficient was calibrated using a second-degree polynomial regression line [expression (16)].

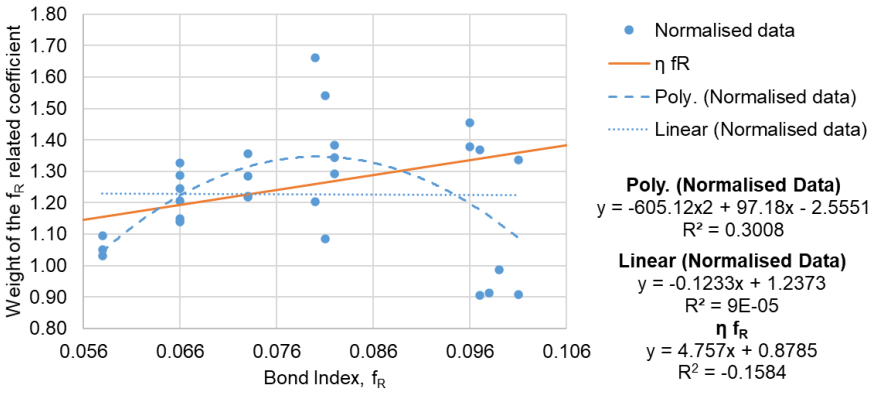


Figure 20 – Weight of the $f_R$ related coefficient versus $f_R$: plotted normalized data results of OC/LBC test series at the first iteration of the calibration process.

Lastly, the calibration of the coefficient concerning the influence of the nominal diameter was performed using a linear regression, which maintained the detrimental effect of the diameter size over bond strength and resulted in expression (17). In conclusion, the first iterative operation performed using OC/LBC test series data successfully calibrated these last two coefficients under a total of six iterative loops.

$$\varphi_{f_R} = \eta_{f_R} = 4.757 \cdot f_R - 0.8785 \quad (15)$$

$$\varphi_\sigma = 135.73 \cdot \sigma^2 - 218.06 \cdot \sigma + 88.498 \quad (16)$$

$$\varphi_d = -0.0293 \cdot d + 1.4719 \quad (17)$$

The next step was to account for the influence of the RA content by addressing the data from the LCRAC test series. These data suggested that the $\eta_{RA_{<c}}$ coefficient was unable to fully explain the experimental bond strength results; hence it was considered the possibility of RA of size equal or greater than the rib spacing, $RA_{\geq c}$ also influencing the bond performance. For example, the series LBC_0,84_Alfred, which has the same characteristics as all LCRAC series (apart from the RA content), had a lower mean bond strength compared to LCRAC_30; regardless, LCRAC_30 only has RA of size equal or greater than the

rib spacing, which seemed to indicate that the inclusion of a coefficient regarding $RA_{\geq c}$would benefit the model's prediction.

Consequently, a second iterative operation was performed on the data comprising the LBC_0,84_Alfred plus the LCRAC test series. These data were normalised prior to iterating to account for the isolated influence of $RA_{\geq c}$ and $RA_{<c}$, as shown in Figure 21, where various regression lines were considered to find out the best fit for the data. When investigated with a linear regression, both $RA_{\geq c}$ and $RA_{<c}$ showed a detrimental effect on the bond strength; however, when adopting a second-degree polynomial line fit the results, there was an indication that whilst $RA_{\geq c}$ is in the range between 0 and 18%, bond performance could be improved. Nevertheless, it should be noted that the amount of data available regarding the bond of LCRAC was very small, which limited, to a great extent, the accuracy of the extracted conclusions.

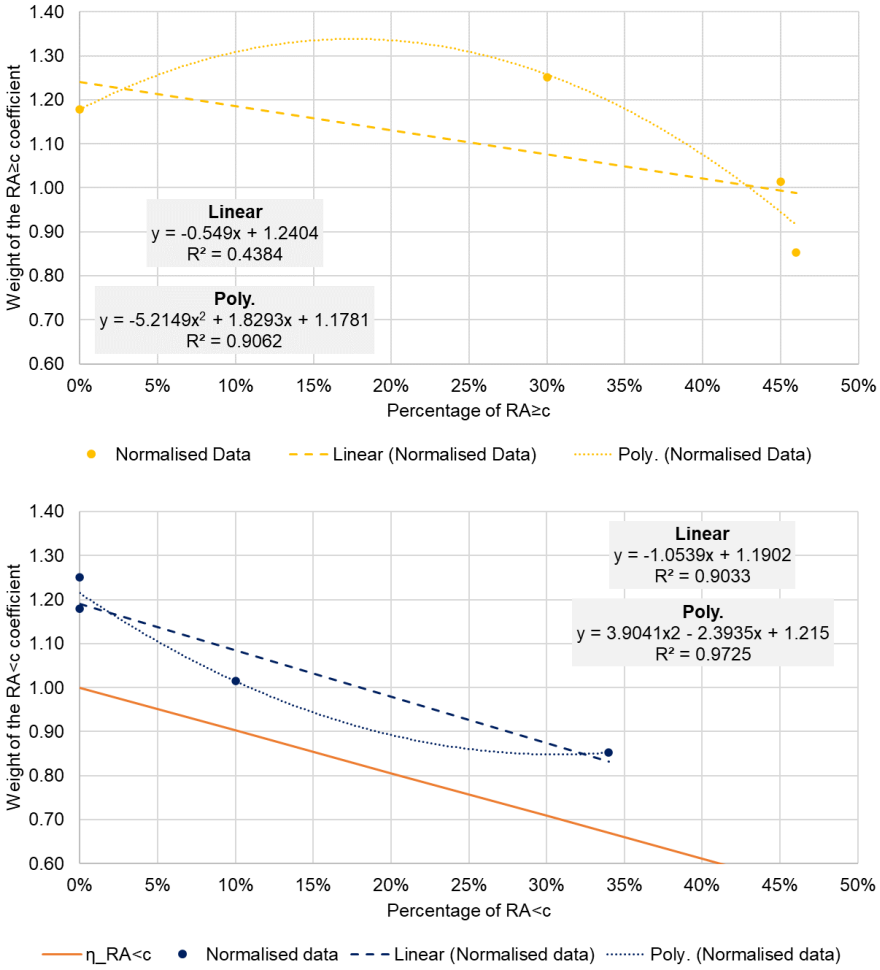


Figure 21 – Weight of the $RA_{\geq c}$ (top) and $RA_{<c}$ (bottom) coefficients vs percentage of RA content: plotted normalised data results of the LBC_0,84_Alfred and LCRAC prior to the second iterative operation.

Even though the experimental results of test series involving RA were limited, the overall observed tendencies seemed to be in accordance with the previously published works concerning the subject, which provides some degree of trust in this approach. As already addressed in the State-of-the-art

chapter, several authors such as Kim and Yun (2013), Prince and Singh (2013, 2014), Xiao and Falkner (2007) and Xu *et al.* (2018) documented the positive effects of RCA over bond behaviour despite the not so favourable arguments delivered by Seara-Paz *et al.* (2014) and Dong *et al.* (2019). Similarly, Kim and Yun (2014) and Dong *et al.* (2019) have also supported the theory that smaller sized RA are detrimental to the bond strength. With these facts in mind, polynomial regression lines were considered to calibrate the coefficients regarding the influence of $RA_{\geq c}$ and $RA_{<c}$. The second iterative operation was completed after six iterative loops and resulted in the calibrated expressions (18) and (19).

$$\varphi_{RA_{\geq c}} = -0.8541 \cdot RA_{\geq c}^2 + 0.4543 \cdot RA_{\geq c} + 0.9702 \quad (18)$$

$$\varphi_{RA_{<c}} = 3.5346 \cdot {RA_{<c}}^2 - 2.1836 \cdot RA_{<c} + 1.1286 \quad (19)$$

To conclude the calibration of the bond strength parameter, a third iterative operation was conducted using all available data (OC, LBC and LCRAC) to refine the coefficients. The final equations for the bond strength parameter and the calibrated coefficients are presented in expressions (20) to (25), and Figure 22 presents the normalised data plotted with the new coefficient equations for each bond-related parameter involved in the bond strength calculation.

$$\tau_{bmax} = 2.5 \cdot \sqrt{f_{cm}} \cdot \varphi_{f_R} \cdot \varphi_{\sigma} \cdot \varphi_{d} \cdot \varphi_{RA_{\geq c}} \cdot \varphi_{RA_{<c}} \quad (20)$$

$$\varphi_{f_R} = 4.757 \cdot f_R + 0.8785 \quad (21)$$

$$\varphi_{\sigma} = 117.17 \cdot \sigma^2 - 188.24 \cdot \sigma + 76.397 \quad (22)$$

$$\varphi_{d} = -0.0292 \cdot d + 1.4634 \quad (23)$$

$$\varphi_{RA_{\geq c}} = -2.2446 \cdot RA_{\geq c}^2 + 1.4731 \cdot RA_{\geq c} + 0.9579 \quad (24)$$

$$\varphi_{RA_{<c}} = 4.038 \cdot RA_{<c}^2 - 2.4333 \cdot RA_{<c} + 1.2152 \quad (25)$$

The deviation to accuracy error regarding the prediction of bond strength with the new calibrated expression was calculated for each test series and compared to the calculations performed for the existing models. From a statistical point of view, this comparison showed that the calibration process brought substantial improvements to the prediction of bond strength of OC/LBC/LCRAC. Results are presented in Table 10 where $\Delta_{max}$ indicates the maximum positive error among all series, $\Delta_{min}$ the maximum negative error, $\Delta_{max} + |\Delta_{min}|$ indicates the range between the maximum positive and negative error, $\Delta_{mean}$ is the mean error and $\Delta_{med}$ the median error.

Table 10 – Accuracy to deviation error data relative to the bond strength parameter.

| | *fib Model Code 2010* | *Louro (2014)* | *Freitas (2016)* | *Pereira (2019)* | *New Model* |
|---|---|---|---|---|---|
| $\Delta_{max}$ | 104.32% | 96.83% | 12.22% | 30.98% | 24.99% |
| $\Delta_{min}$ | -8.04% | -21.44% | -56.00% | -42.15% | -22.51% |
| $\Delta_{max} + \lvert\Delta_{min}\rvert$ | 112.36% | 118.27% | 68.22% | 73.13% | 47.50% |
| $\Delta_{mean}$ | 39.30% | 31.48% | -17.20% | -1.48% | 0.00% |
| $\Delta_{med}$ | 33.30% | 28.41% | -10.62% | 0.38% | -0.01% |

The calibration of the bond strength parameter successfully reduced both the positive and negative maximum errors in 5.99 and 19.64%, achieving a lower error range of 47.50%, whilst both the mean

and median error got approximately close to 0%, which can be considered only as a minor improvement over the model of Pereira (2019).

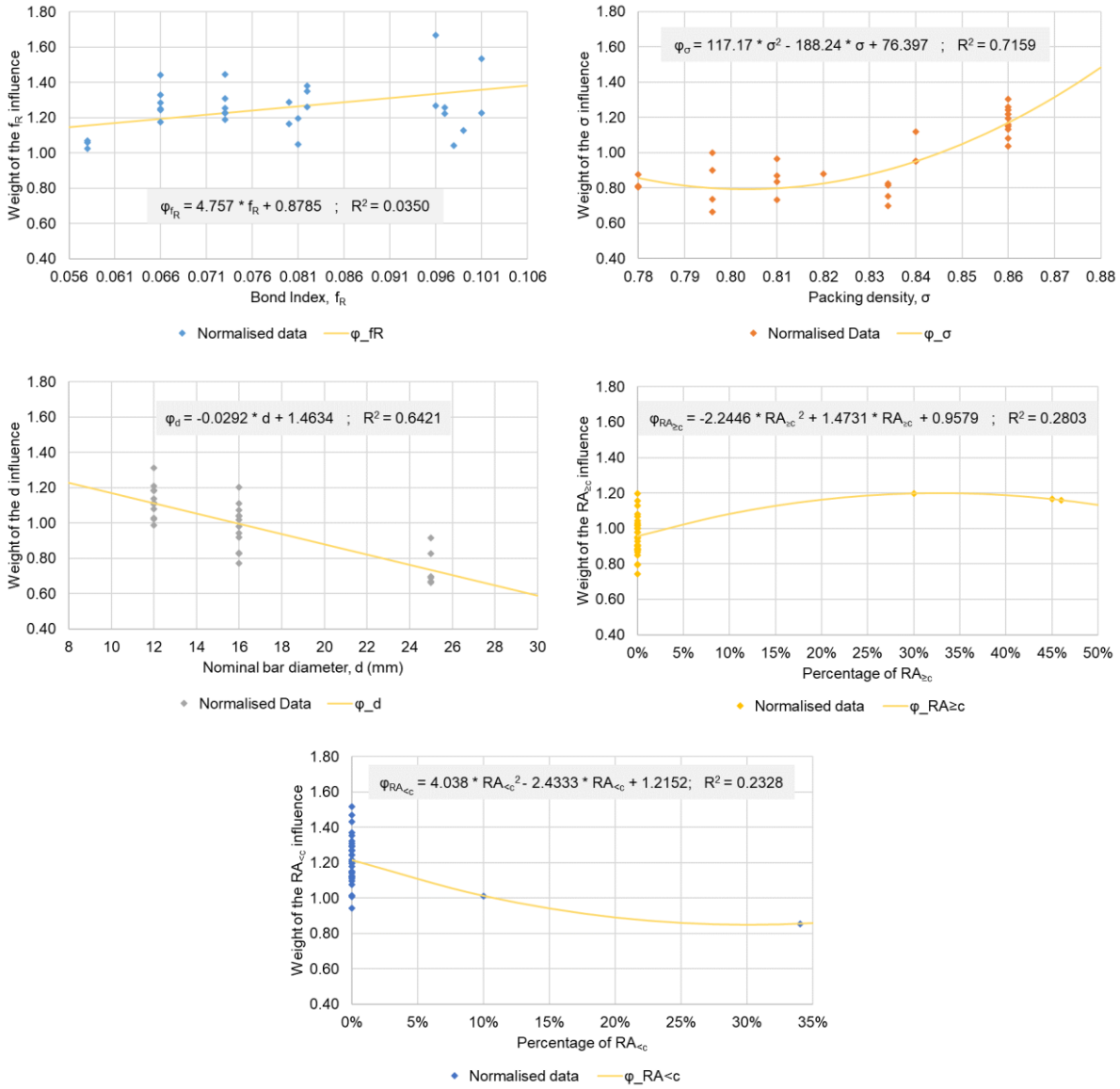


Figure 22 – Normalised data plotted with the new coefficient equations for each bond-related parameter involved in the bond strength calculation.

### 3.4.2.2 Ascending branch and plateau

Concerning the parameters of the ascending branch and bond strength plateau (i.e. $\alpha$, $s_1$ and $s_2$), their calibration process differed significantly from the one used for the bond strength. Since there was no clear influence of the studied bond-related parameters over the slip values at peak stress, a different approach was needed to calibrate the parameters, which finally consisted of analysing the experimental data and tentatively comparing experimental and hypothetical bond stress-slip curves. A clear example of incongruent results that difficulted the calibration of the slip parameters came by observation of data from Freitas (2016) and Pereira (2019), where test series often share the same values (diameter and packing density) but also have very different initial bond stiffness results. More specifically, Pereira's

(2019) specimens often exhibited a stiffer bond behaviour than those of Freitas (2016). This fact is displayed in Figure 23, where the mean bond stress-slip curves of series with d = 12 mm and σ = 0.86 exhibited a distinct initial slope regardless of the bond strength. Additionally, differences in the other parameters, which can be compared in the previous Table 7, cannot justify this inconsistency.

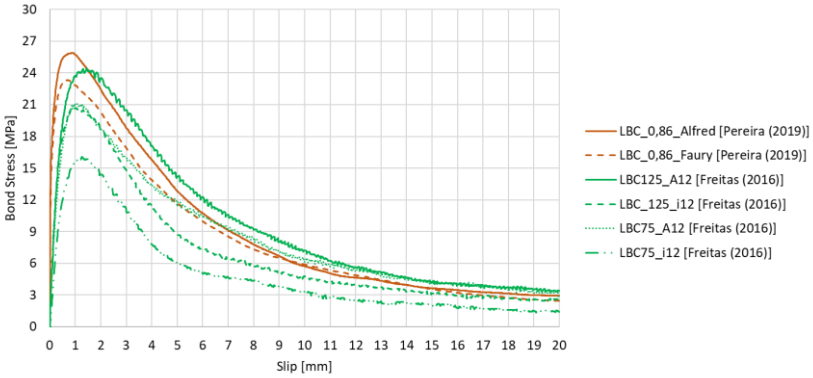


Figure 23 – Initial bond stiffness comparison between Freitas (2016) and Pereira (2019) test series.

Whereas Louro (2014) and Pereira (2019) presented arguments regarding the influence of $f_R$ and $\sigma$ over the bond plateau's slip values, respectively, in the present work, the parameter which indicated a stronger correlation with $s_1$ and $s_2$ was, in fact, the bar diameter. As the diameter increased, a clear tendency was revealed for the increase of slip and concomitantly a decrease in bond stiffness. As such, the expressions (26) and (27) were proposed as the new calibrated equations of $s_1$ and $s_2$. Although there is no exact way to compare experimental and theoretical slip values for the bond strength plateau, both expressions were aimed to provide an overall conservative estimation. In comparison, *fib* Model Code 2010 prescribes the parameters $s_1$ and $s_2$ as equal to 1.0 and 2.0 mm respectively, regardless of bar diameter, whereas the new calibrated $s_1$ parameter takes on the values of 0.75, 0.95 and 1.45 mm for the range of bars used in the experimental data (d = 12, 16 and 25 mm), and with the bond strength's plateau maintaining a length of 1.0 mm.

$$s_1 = 0.05 \cdot d + 0.15 \quad (26)$$

$$s_2 = 0.05 \cdot d + 1.15 \quad (27)$$

Regarding the $\alpha$ coefficient, an attempt was made for its calibration; however, despite the relationship established by Pereira (2019) between the coefficient and the packing density, analysis of a broader set of data showed no noticeable improvements when using his equation presented in Table 9. Hence, the value of 0.4 prescribed by *fib* Model Code 2010 was adopted for the optimised calibrated bond model.

#### 3.4.2.3 Residual bond stress

The residual bond stress was the last parameter to be calibrated. Figure 24 depicts the data from all test series and opposes the experimental values of $\tau_{bf}$ against the prediction values of $\tau_{bmax}$ calculated by equation (20). The data seemed to confirm the statement made by Pereira (2019) that the type of concrete influences the residual bond capacity. Concrete types containing low binder quantities (LBC and LCRAC) tended to present a lower residual bond capacity than OC with the same bond strength.

Pereira (2019) suggested that the $\tau_{bf}$ of LBC/LCRAC be 30% of $\tau_{bmax}$; however, given the new calibrated expression for $\tau_{bmax}$, some adjustments were made to better fit the results. The calibrated prediction curves for $\tau_{bf}$ are plotted in Figure 24 together with those of *fib* Model Code 2010 and Pereira (2019). Additionally, the new equations for the calculation of $\tau_{bf}$ according to concrete type are presented in expressions (28) and (29).

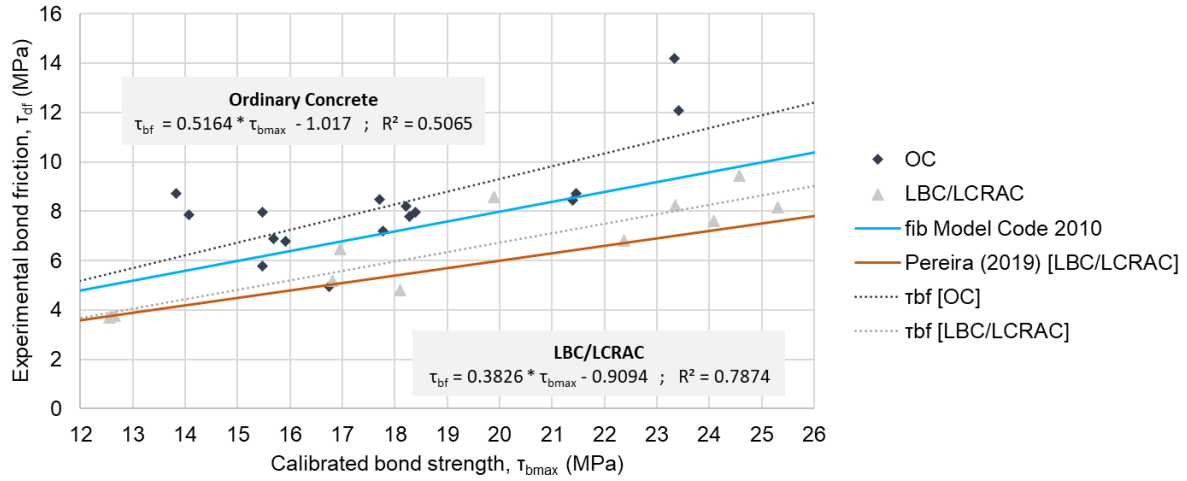


Figure 24 – Relation between the bond strength prediction of the calibrated bond model and the experimental friction bond stress.

$$\tau_{bf} = 0.5164 \cdot \tau_{b,max} - 1.017, \qquad for\ OC \tag{28}$$

$$\tau_{bf} = 0.3826 \cdot \tau_{b,max} - 0.9094, \qquad for\ LBC/LCRAC \tag{29}$$

The following Table 11 presents the data regarding the deviation to accuracy error of $\tau_{bf}$ in accordance with the various bond models. Given that $\tau_{bf}$ is calculated indirectly from $\tau_{bmax}$, in general, every model presents slightly worst predictions for this parameter when compared to the bond strength results. Nonetheless the calibrated $\tau_{bf}$ presents an error range close to the model from Freitas (2016) (lowest of the five models) and presents the mean and median errors closest to 0%; however, the fact that $\Delta_{mean}$ and $\Delta_{med}$ are negative indicate that the calibrated $\tau_{bf}$ will often be slightly overestimated, which is undesirable.

Table 11 – Data regarding the deviation to accuracy errors of $\tau_{bf}$.

| | *fib Model Code 2010* | *Louro (2014)* | *Freitas (2016)* | *Pereira (2019)* | *New Model* |
|---|---|---|---|---|---|
| $\Delta_{max}$ | 108.40% | 100.76% | 34.07% | 66.68% | 46.54% |
| $\Delta_{min}$ | -11.54% | -14.78% | -48.02% | -25.24% | -37.65% |
| $\Delta_{max} + \lvert\Delta_{min}\rvert$ | 119.94% | 115.54% | 82.09% | 91.93% | 84.20% |
| $\Delta_{mean}$ | 36.69% | 27.77% | -18.56% | 14.81% | -1.76% |
| $\Delta_{med}$ | 39.57% | 22.85% | -21.21% | 9.77% | -4.91% |

### 3.4.3 Proposed bond stress-slip relationship

The outcome of the calibration of the new local bond stress-slip model for steel reinforcement embedded in OC, LBC or LCRAC under good bond conditions for pull-out failure is presented in Table 12.

Table 12 – Proposed local bond stress-slip model.

| | |
|---|---|
| $\tau_{bmax}$ [MPa] | $2.5 \cdot \sqrt{f_{cm}} \cdot \varphi_{f_R} \cdot \varphi_\sigma \cdot \varphi_d \cdot \varphi_{RA_{\geq c}} \cdot \varphi_{RA_{<c}}$ |
| $\varphi_{f_R}$ | $4.757 \cdot f_R + 0.8785$ |
| $\varphi_\sigma$ | $117.17 \cdot \sigma^2 - 188.24 \cdot \sigma + 76.397$ |
| $\varphi_d$ | $-0.0292 \cdot d + 1.4634$ |
| $\varphi_{RA_{\geq c}}$ | $-2.2446 \cdot RA_{\geq c}^2 + 1.4731 \cdot RA_{\geq c} + 0.9579$ |
| $\varphi_{RA_{<c}}$ | $4.038 \cdot RA_{<c}^2 - 2.4333 \cdot RA_{<c} + 1.2152$ |
| $s_1$ [mm] | $0.05 \cdot d + 0.15$ |
| $s_2$ [mm] | $0.05 \cdot d + 1.15$ |
| $s_3$ [mm] | $c$ |
| $\alpha$ | $0.4$ |
| $\tau_{bf}$ [MPa] | $0.5164 \cdot \tau_{bmax} - 1.017, \quad for\ OC$ |
| | $0.3826 \cdot \tau_{bmax} - 0.9094, \quad for\ LBC/LCRAC$ |

Where,

- $\tau_{bmax}$ is the bond strength;
- $\varphi_{f_R}$ is the coefficient for the influence of the bond index $f_R$;
- $\varphi_\sigma$ is the coefficient for the influence of the packing density $\sigma$;
- $\varphi_d$ is the coefficient for the influence of the bar diameter $d$;
- $\varphi_{RA_{\geq c}}$ is the coefficient for the influence of the RA with a size equal or greater than the rib spacing;
- $\varphi_{RA_{<c}}$ is the coefficient for the influence of the RA with a size smaller than the rib spacing;
- $s_1$ and $s_2$ are the limit slip values of the bond strength plateau;
- $s_3$ is the slip value for the beginning of the bond's residual capacity;
- $\alpha$ is the coefficient that characterizes the $\tau_b - s$ relationship of the ascending branch;
- $\tau_{bf}$ is the residual bond stress due to bond friction.

# 4. Finite element modelling of bond behaviour

## 4.1 Introduction

The bond behaviour can strongly affect the structural performance, be it at the SLS, where bond has an impact on the width and spacing of transverse cracks, the tension stiffening and the curvature, or be it at the ULS, where bond is responsible for the strength of end anchorages and lapped joints of reinforcement and influences the rotation capacity of plastic hinge regions; thus, the study of bond behaviour is essential. (Federation internationale du beton 2010)

Cairns and Plizzari (2003) explained that bond stresses are not uniform along a length of rebar and tend to be greater near points of curtailment/anchorage or transverse cracks. Furthermore, bond strength depends on many factors, making a detailed evaluation of bond performance a complex affair. As such, bond characterisation tests should adopt short bond lengths (i.e. smaller than $6\phi$) to assess local bond behaviour. Furthermore, bond stresses in test specimens with short bonded lengths are generally larger than design bond stress values since they rely on relatively high confinement, which is necessary to ensure that bond failure occurs in a ductile manner and not by splitting. The study of local bond stress-slip relationships has the advantage of demanding lighter test specimens and smaller testing equipment; furthermore, it can provide the necessary data for the numerical modelling of bond behaviour, consequentially enabling the study of bond behaviour of embedded reinforcement on a more global structural scale with longer bond lengths.

The present chapter will address the specificities concerning the finite element modelling of bond behaviour and how it was performed, starting with a simple overview of the alternative methods currently available to perform this operation. Shafaei *et al.* (2009) briefly described the two main ways of modelling bond behaviour: (a) detailed modelling in which the whole reinforcing bar (i.e. nominal diameter and ribs) is modelled as a 3D element or (b) phenomenological modelling, in which a smeared or discrete formulation for the rebar-concrete interface is used, with bond being simulated either by interfacial FE or through a reinforcing bar with a bond function. Figure 25 presents a schematic illustration of the aforementioned methods.

The alternative chosen for the present work was the phenomenological modelling approach, which overall enables the realistic simulation of bond behaviour with relatively low computational effort and in a short timeframe. By assigning a constitutive bond function to the model, it is possible to emulate bond behaviour for different structural element geometries and boundary conditions; however, for example, it lacks the capability of accurately predicting the bond behaviour based on influencing concrete or rebar parameters not included as variables of the bond function *a priori*. As such, if it is needed to assess the influence of these unaccounted parameters, a detailed modelling approach should be enforced; however, this method arises heavier computational efforts since the geometrical modelling of the rebar elements and the concrete lugs demand the generation of very refined 2D or 3D FE meshes to ensure good results.

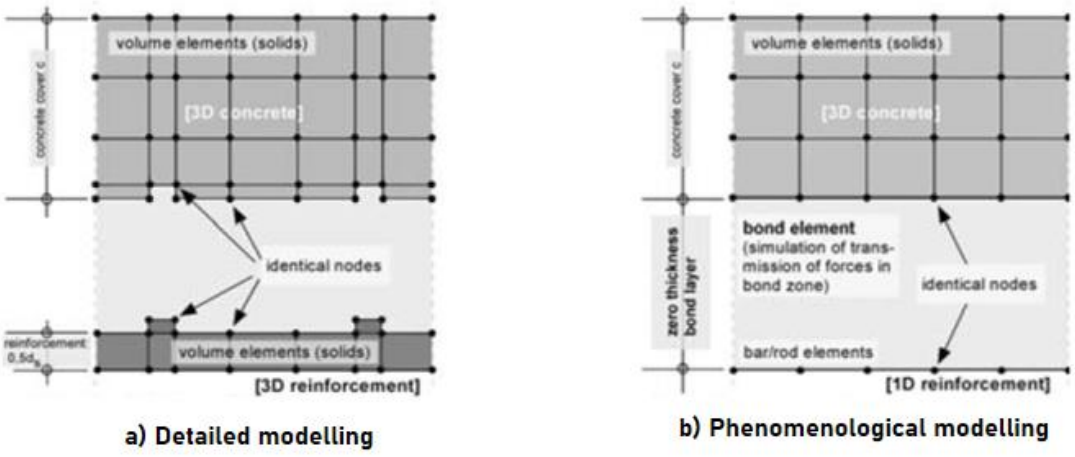


Figure 25 – Methods for the numerical modelling of bond behaviour.
Adapted from Shafaei *et al.* (2009).

## 4.2 Modelling in ATENA 3D/GiD

The creation of finite element models to study bond behaviour through non-linear structural analysis was performed using the commercial software ATENA (Advanced Tool for Engineering Nonlinear Analysis) developed by *Červenka Consulting s.r.o.*. This choice of software was based on its ability to perform the phenomenological modelling of bond behaviour by assigning reinforcement elements with a bond function through a so-called *reinforcing bar with bond* system. This system, detailed by Jendele and Cervenka (2006) and illustrated in Figure 26, is constituted of three different FE types: a "concrete" 3D continuous element, a 1D bar truss element (with constant strain) and a 1D superimposed bond element (with constant slip).

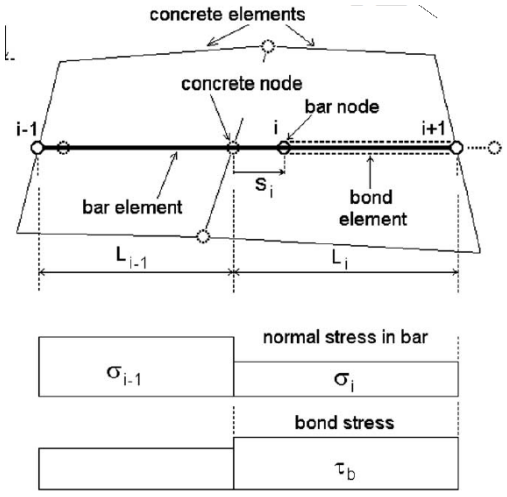


Figure 26 – System of reinforcing bar with bond embedded in a concrete element, adapted from Jendele and Cervenka (2006).

The bond FE has two nodes, each with two orthogonal springs that connect and transmit shear and normal forces between the coincident 1D bar and 3D concrete element nodes (whilst in the non-deformed configuration).

Changes in the stresses between concrete and bar elements generate slip $s$ (i.e. a constant displacement field in the bond FE, with a direction parallel to the bar element's axis). The slip constitutes a new degree of freedom (non-existent in the hypothesis of a perfect bond) that is the difference between the concrete and bar displacements. As depicted in Figure 27, the original length of the bar $L_0$ changes to $L$ as the bar nodal displacement $\vec{u}$ is calculated by expression (30) as the sum of the slip with the displacement $u$ of the surrounding concrete.

$$\vec{u} = u + s \tag{30}$$

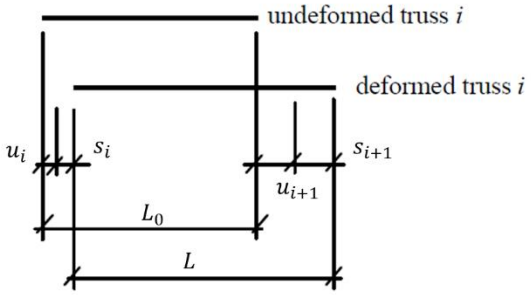


Figure 27 – Truss bar element with slip, adapted from (Červenka *et al.* 2012)

Subsequently, the evaluation of the normal stress $\sigma_i$ found at each bar element $i$ with the nodes $i$ and $i+1$ is performed by the expression (31), where $E$ is the modulus of elasticity and $L_i$ is the length of the bar element $i$. Therefore, expression (32) ensures the system's equilibrium, being that if the inequality is violated, it indicates that there is no relative displacement between materials. It should be noted that $A$ is the bar cross-sectional area, $p$ the bar perimeter and $\tau_{bmax}$ the bond defined by a constitutive bond stress-slip function $C_b$ [expression (33)].

$$\sigma_i = \frac{E}{L_i}(\vec{u}_{i+1} - \vec{u}_i) = \frac{(u_{i+1} + s_{i+1} - u_i - s_i)}{L_i} E \tag{31}$$

$$\frac{\partial \sigma}{\partial x} \leq \tau_{bmax} \frac{p}{A} \Leftrightarrow A(\sigma_{i+1} - \sigma_i) \leq L_i \cdot p \cdot \tau_{b,max} \tag{32}$$

$$\tau_{bmax} = C_b(s) \tag{33}$$

Due to the assumption of constant strain distribution in the bar element, two stress values exist at each bar node. The bond stress is then calculated from the different nodal stresses. The operation for calculating the bond stress at node $i$ is shown in expression (34), thus completing the description of the *reinforcing bar with bond* system. (Jendele and Cervenka 2006)

$$\begin{aligned} \overrightarrow{\sigma_{i+1}} &= \frac{\sigma_{i+1} \cdot L_{i+1} + \sigma_i \cdot L_i}{L_{i+1} + L_i} \\ \overrightarrow{\sigma_i} &= \frac{\sigma_i \cdot L_i + \sigma_{i-1} \cdot L_{i-1}}{L_i + L_{i-1}} \\ \tau_b &= \frac{(\overrightarrow{\sigma_{i+1}} - \overrightarrow{\sigma_i}) \cdot A}{L_i \cdot p} \end{aligned} \tag{34}$$

The present section will briefly explain the basis of the FE modelling development in ATENA. Overall, it consists of the geometry definition, the assignment of constitutive material laws, the load case creation, the mesh generation, and the non-linear analysis configuration in the pre-processing stage.

### 4.2.1 Geometry definition

Modelling in the ATENA software can be performed using the ATENA 3D user interface from *Červenka Consulting s.r.o.* or the *GiD* user interface from *CIMNE – International Center for Numerical Methods in Engineering* and begins with the geometric definition. Concrete elements are created by building 3D regions called macroelements (ME), and a material constitutive law for the desired material (i.e. concrete or otherwise) can be later assigned. In turn, reinforcing bars can be created through discrete 1D truss elements. A bar diameter and a material constitutive law should then be assigned to these 1D truss elements.

By default, ATENA configures each reinforcement element as having a perfect connection to the surrounding ME; however, bond behaviour can be modelled by assigning a bond material function to each truss element, consisting of a local bond stress-slip relationship generated by the software or inputted by the user. In addition, the software provides options to limit the slip at the ends of the reinforcement or introduce a bond stress variation across the bar length, which permits the user to model certain portions of the bar as non-bonded to the surrounding concrete element.

### 4.2.2 Constitutive laws for materials and bond

#### 4.2.2.1 Concrete

Concrete elements were modelled using the material CC*3DNonLinCementitious2.* This material constitutive model is based on fracture mechanics, plasticity and damage and combines constitutive laws for tensile and compressive behaviour, as represented in Figure 28. The material's tensile behaviour employs the Rankine failure criterion and exponential softening, whereas the hardening/softening plasticity model is based on the Menétrey-Willam failure surface. Regarding the hardening/softening law, the hardening curve is elliptical and is based on strains, whereas the softening curve is linear and is based on displacements.

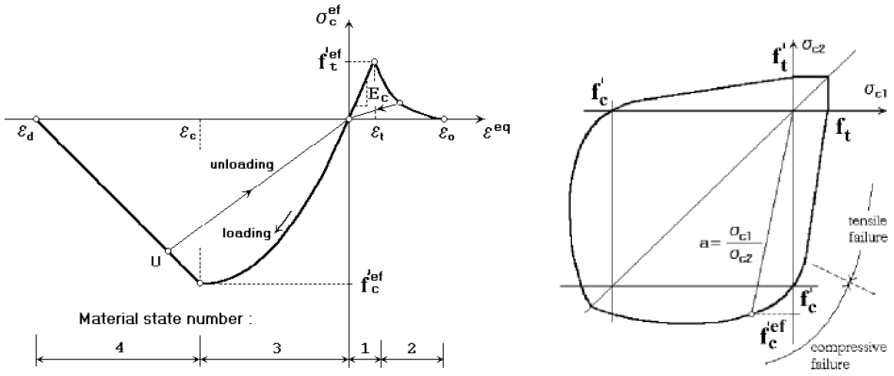


Figure 28 – CC3DNonLinCementitious2 stress-strain law (left) and bi-axial failure surface (right), adapted from Červenka *et al.* (2012).

#### 4.2.2.2 Reinforcement

The reinforcing bars were modelled using the material *CCReinforcement,* which considers the steel behaviour according to a bilinear stress-strain law with hardening, as presented in Figure 29.

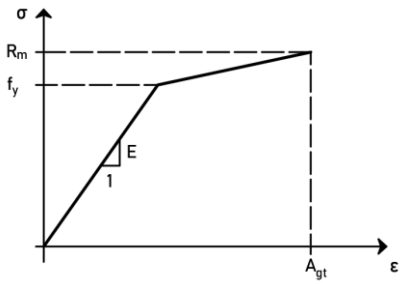


Figure 29 – CCReinforcement bi-linear stress-strain law with hardening.

The bond behaviour is modelled with the material *CCReinforcementBondModel*, which requires the definition of a bond stress-slip function. Figure 30 provides an example of the user-defined bond material in the ATENA 3D interface. When considering the user-defined option, the bond stress value of 0.05 MPa was always matched with the slip of 0 m, as Pryl and Červenka (2015) advised, to avoid numerical errors in the simulation.

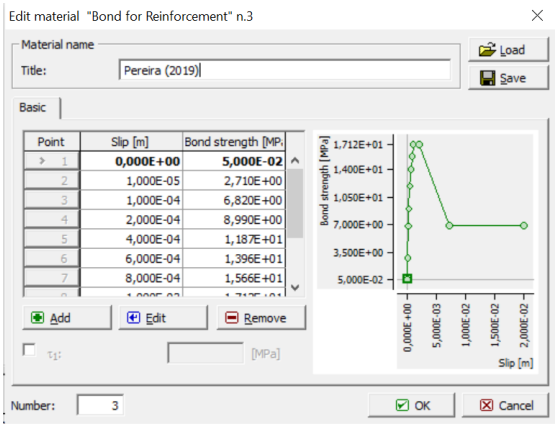


Figure 30 – *ATENA 3D* user interface for the definition of the bond stress-slip function concerning the *CCReinforcemendBondModel* material.

### 4.2.3 Loading History

The loading history defines all actions that occur during the processing phase of the numerical analysis and consists of several analysis steps, each one combining a set of load cases (i.e. the support conditions plus prescribed deformation/applied forces). Furthermore, the ATENA software defines the total actions by the integral in time of the force increments by applying a solution method (i.e. Newton-Raphson or Arc-length). In the present work, the Newton-Raphson method was used for analysing all the developed models.

### 4.2.4 Mesh generation

ATENA offers various options for mesh generation by using different FE types with a varying number of nodes. These element types can either be tetrahedral or hexahedral and are commonly referred as *Tetra* and *Brick* elements. Mesh compatibility is automatically assured in the cases where neighbouring ME have surfaces in contact with an equal area; however, when that is not the case, it is necessary to define surfaces with the *Master* and *Slave* commands so that when the mesh is generated, the nodes from the *Slave* surface will be forced to be compatible with the nodes from the *Master* surface. This method was often used when modelling support/loading plates, described in further sections.

## 4.3 Description of the finite element models

### 4.3.1 Introduction

The pull-out model was created to replicate the test specimens of the experimental campaigns of Louro (2014), Freitas (2016) and Pereira (2019). The initial intent of this model was to perform the numerical calibration of a new bond stress-slip law concerning the local bond behaviour of various concrete types. However, the realisation that the phenomenological approach to the modelling of bond behaviour was not suited to this purpose led to a change in the approach. Hence, the pull-out model showed that it is possible to successfully model local bond behaviour and compare the experimental results from the various campaigns with the theoretical bond models incorporated into the numerical modelling.

In addition, the approach utilised to model the local bond behaviour of the pull-out model was then employed in the modelling of two beam models with different reinforcement configurations. By modelling these structures, utilizing the theoretical bond models for local bond behaviour, it was possible to study the bond behaviour of reinforcing bars with long embedded lengths and the bond failure occurring around the anchorage/lap-splice zones of the reinforcement.

### 4.3.2 Pull-out model

Concerning the pull-out model, four reference models were designed with geometrical properties similar to those of the test specimens. Furthermore, these models were divided into four groups to account for the slight differences between the specimens produced by each author: the Standard pull-out model (with diameters of 12 and 16 mm) and the Modified pull-out model (with diameters of 16 and 25 mm). Each reference model mainly differs in dimensions and represents all the test series performed with similar geometry. The material properties of each reference model are subsequently changed to replicate the characteristics of a given test series and consequently conduct the intended non-linear structural analysis.

#### 4.3.2.1 Model geometry

The model's geometric definition was performed in the *ATENA 3D* user interface and started with creating ME for the concrete parts of the pull-out test and 1D discrete truss elements to represent the reinforcing bars. Additionally, to model the reinforcement as embedded or disconnected to the

surrounding concrete, separate ME were created: two for the Standard and three for the Modified models; The same was applied to the truss elements, which were created with various segments to account for the different bond interfaces. Lastly, as load assignment in *ATENA 3D* is only applicable to 3D regions, an auxiliary cube was created and connected to the main reinforcement element enabling the prescribed displacement to be applied to the pull-out models. Figure 31 presents a 3D view of both the Standard and the Modified models during the pre-processing stage. In addition, Table 13 presents the dimensions of each one of the elements created for each reference model.

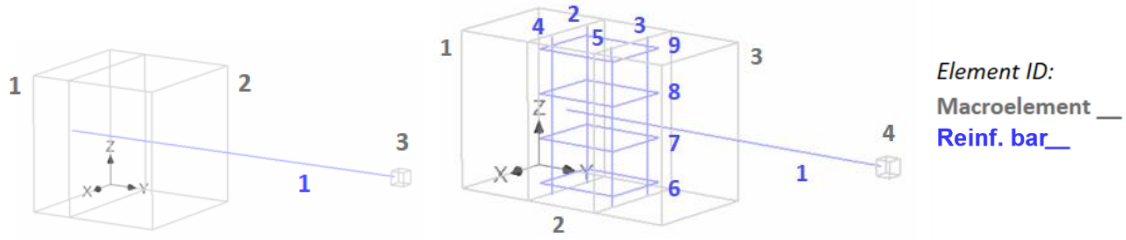


Figure 31 – 3D view of the Standard (top) and Modified (bottom) models.

Table 13 – Dimensions (mm) of the reference models featured in Figure 31.

| | *Standard_12* | | | *Standard_16* | | | *Modified_16* | | | *Modified_25* | | |
|---|---|---|---|---|---|---|---|---|---|---|---|---|
| *Element ID* | X | Y | Z | X | Y | Z | X | Y | Z | X | Y | Z |
| *ME 1* | 200 | 60 | 200 | 200 | 80 | 200 | 150 | 100 | 195 | 215 | 150 | 300 |
| *ME 2* | 200 | 140 | 200 | 200 | 120 | 200 | 150 | 100 | 195 | 215 | 150 | 300 |
| *ME 3* | 20 | 20 | 20 | 20 | 20 | 20 | 150 | 100 | 195 | 215 | 150 | 300 |
| *ME 4* | | | | | | | 20 | 20 | 20 | 20 | 20 | 20 |
| *Reinf. bar 1* | - | 540 | - | - | 540 | - | - | 565 | - | - | 565 | - |
| *Reinf. bar 2* | | | | | | | - | - | 195 | - | - | 300 |
| *Reinf. bar 3* | | | | | | | - | - | 195 | - | - | 300 |
| *Reinf. bar 4* | | | | | | | - | - | 195 | - | - | 300 |
| *Reinf. bar 5* | | | | | | | - | - | 195 | - | - | 300 |
| *Reinf. bar 6* | | | | | | | 90 | 110 | - | 112 | 175 | - |
| *Reinf. bar 7* | | | | | | | 90 | 110 | - | 112 | 175 | - |
| *Reinf. bar 8* | | | | | | | 90 | 110 | - | 112 | 175 | - |
| *Reinf. bar 9* | | | | | | | 90 | 110 | - | 112 | 175 | - |

** Reinf. bars 5 to 9 are composed of multiple 1D segments oriented in the X and Y directions.*

#### 4.3.2.2 Material parameters

The common concrete mechanical properties were automatically generated by the default programmed formulae of ATENA (Červenka *et al.* (2012) as a function of the compressive strength value measured in cubes. So, the concrete material assigned to the ME was generated to match the mean values of compressive strength that were measured by Louro (2014), Freitas (2016) and Pereira (2019) (Table 7) in order to replicate the material behaviour of the studied pull-out test series. Regarding the steel reinforcement material, the input values for the software were those experimentally measured by the authors, specifically the yield strength ($f_y$), ultimate tensile strength ($R_m$), modulus of elasticity ($E$) and elongation at fracture ($A_{gt}$). In cases where data regarding one of these parameters were not available, conservative values were assumed. The considered values can be found in Table 14Table 15Table 16.

Table 14 – Reinforcement material parameters for the pull-out model series based on Louro (2014).

| | *A_C1_16* | *B_C1_16* | *AT_C1_16* | *BT_C1_16* | *A_C2_16* | *AT_C2_16* | *A_C1_25* | *B_C1_25* | *AT_C1_25* | *BT_C1_25* | *A_C2_25* | *B_C2_25* |
|---|---|---|---|---|---|---|---|---|---|---|---|---|
| $f_y$ *(MPa)* | 544 | 541 | 517 | 444 | 544 | 517 | 530 | 548 | 464 | 473 | 530 | 548 |
| $R_m$ *(MPa)* | 640 | 636 | 611 | 540 | 640 | 611 | 638 | 662 | 570 | 578 | 638 | 662 |
| $A_{gt}$ *(%)* | 13 | 13 | 13 | 14 | 13 | 13 | 10 | 11 | 12 | 9 | 10 | 11 |
| *E (GPa)* | 197 | 187 | 194 | 191 | 197 | 194 | 191 | 198 | 192 | 192 | 191 | 198 |

Table 15 – Reinforcement material parameters for the pull-out model series based on Freitas (2016).

| | *C250_A12* | *LBC125_A12* | *LBC75_A12* | *C250_i12* | *LBC125_i12* | *LBC75_i12* | *C250_A16* | *LBC125_A16* | *LBC75_A16* | *C250_i16* | *LBC125_i16* | *LBC75_i16* |
|---|---|---|---|---|---|---|---|---|---|---|---|---|
| $f_y$ *(MPa)* | 543 | | | 651 | | | 536 | | | 573 | | |
| $R_m$ *(MPa)* | 630 | | | 757 | | | 633 | | | 760 | | |
| $A_{gt}$ *(%)* | 13.4 | | | 19.8 | | | 11.2 | | | 28.3 | | |
| *E (GPa)* | No data | | | | | | | | | | | |

Table 16 – Reinforcement material parameters for the pull-out model series based on Pereira (2019).

| | *LBC_0,86_Alfred* | *LBC_0,84_Alfred* | *LBC_0,82_Alfred* | *LBC_0,86_Faury* | *LCRAC_30* | *LCRAC_55* | *LCRAC_80* |
|---|---|---|---|---|---|---|---|
| $f_y$ *(MPa)* | 551 | | | | | | |
| $R_m$ *(MPa)* | 671 | | | | | | |
| $A_{gt}$ *(%)* | 12.0 | | | | | | |
| *E (GPa)* | 205 | | | | | | |

Regarding the auxiliary ME used for loading the model, the material *CC3DElastIsotropic* was chosen to replicate a linear elastic isotropic behaviour. In addition, the material had a modulus of elasticity of 200 GPa, thus making the ME's deformation irrelevant to the results.

The definition of the bond material was always defined by the user considering the bond models previously mentioned in this work and the new calibrated model. Additionally, the option to prevent the slip at the end of the bar was used to ensure the connection between the main reinforcement element and the auxiliary ME. Furthermore, the file generated by the *ATENA 3D* pre-processor with the extension "*.inp"* was programmed with the option "*Embedded in Solid*" to indicate which ME should be bonded to the bar.

Lastly, in the case of the transverse reinforcing bars, no bond material was assigned to them (i.e. perfect connection set by default was considered), given that it would not be relevant to the analysis.

#### 4.3.2.3 Loading history

The loading history of the pull-out model consists of two load cases: a prescribed displacement and the support conditions. Loading of the model was performed through a prescribed displacement of 0.20 mm along the axial direction of the main reinforcement, prescribed to the surface of the auxiliary ME. Thus,

the analysis was set to run for 100 steps using the Newton-Raphson method with a limit of 40 iterations per step to reach a final displacement of 20 mm in order to capture the most relevant part of the bond stress-slip curve, similar to what was performed in the experimental tests. Also, the support conditions consisted of restraining the translations, in all directions, of the concrete ME surface closest to the loaded end of the reinforcement, thus simulating the contact between the concrete test piece and the testing apparatus. Additionally, translations in the X and Z directions were restrained in the loaded surface of the auxiliary ME to avoid any lateral movements when under load.

The mesh generated for the reference models consisted of different finite element types: the concrete regions were meshed using linear *Brick* elements, whereas the auxiliary cube was roughly meshed using linear *Tetra* elements. Table 17 indicates the number of mesh elements contained in each ME.

Table 17 – Number of finite elements per Macroelement of the reference models.

| | *Macroelement 1* | *Macroelement 2* | *Macroelement 3* | *Macroelement 4* |
|---|---|---|---|---|
| *Standard 12* | 576 | | 26 | - |
| *Standard 16* | 1000 | | 26 | - |
| *Modified 16* | 576 | | | 26 |
| *Modified 25* | 576 | | | 26 |

Several monitoring points were defined in the model during the pre-processing stage, as indicated in Figure 32. The definition of these points enabled a better understanding of the results since they allowed the recording, at each step, of certain quantities such as displacements or stresses at given selected coordinates.

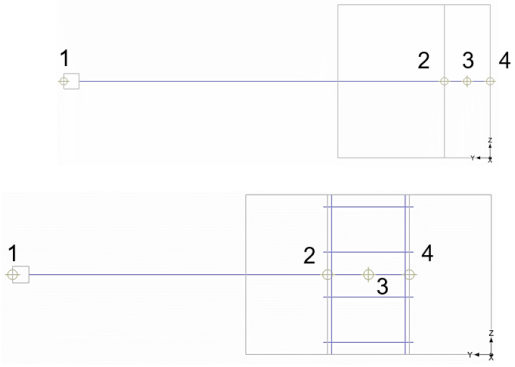


| Monitored quantity | Monitor nº |
|---|---|
| External force | 1 |
| Displacement | 1,2,4 |
| Stress | 2 |
| Bond Stress | 2,3,4 |
| Slip | 2,3,4 |

Figure 32 – Monitoring points of the Standard (top) and Modified (bottom) pull-out models.

### 4.3.3 Beam models

In the sequence of the successful results obtained from the pull-out numerical models, which will be addressed in a further chapter, the intention was to develop the knowledge of the numerical modulation of the local bond behaviour in a practical exercise based on two conceptual structural members. These structural members were conceived as simply supported beams of small cross-section and distinct reinforcement layouts: the first with straight anchored bars (Straight Anchorage Beam model) and the second with lap-spliced bars (Lap-Splice Beam model). The goal of these beams was to evaluate the anchorage length that their reinforcement would require to resist a bending action whilst also varying

the bond function assigned to the reinforcement. Thus, these beam models were the basis of a parametric study investigating the influence of the local bond behaviour on the reinforcement development length on beams with low binder concrete and low cement recycled aggregate concrete.

#### 4.3.3.1 Model geometry

The geometric definition of both beam models was performed in the *GiD* user interface and can be summarised by the creation of the concrete body followed by the rectangular support/loading plates and, finally, the truss elements for the reinforcing bars.

The Straight Anchorage Beam (SAB) model consists of a beam with 0.20 x 0.30 $m^2$ cross-section and 6.00 m span length, where the support/loading plates have dimensions 0.20 x 0.30 x 0.03 $m^3$. Therefore, the model has two support plates at the bottom surface of the beam and one loading plate positioned at mid-span on the top surface. In addition, there are four reinforcing bars symmetrically placed at the bottom of the beam that extend from both sides to the mid-span. The reinforcement ends in contact with the surfaces of the beam were modelled with no slippage, thus simulating the effect of a hooked anchorage. Furthermore, the external bars have a hooked anchorage at mid-span, whilst the inner bars have different straight anchorage lengths, beginning at the mid-span, to conduct the previously cited parametric study. Figure 33 provides a graphical description of the geometry of the SAB model.

The Lap-Splice Beam (LSB) model is very similar to the SAB model with only slight differences. First of all, instead of just one loading plate at the top, the LSB has two, positioned at the top surface at 1 m from the mid-span opposite each other. Moreover, the four bar elements overlap at mid-span to create two lap-splices. The lap-splice development length varied throughout the analysis to conduct the aforementioned parametric study. Figure 34 provides a graphical description of the geometry of the LSB model.

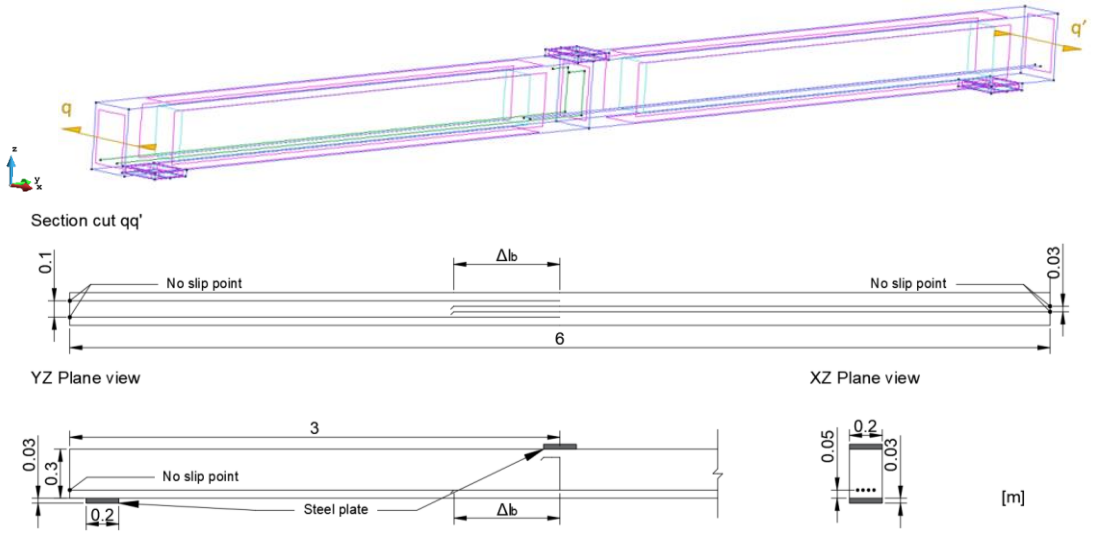


Figure 33 – Geometry of the straight anchorage beam model (SAB model).

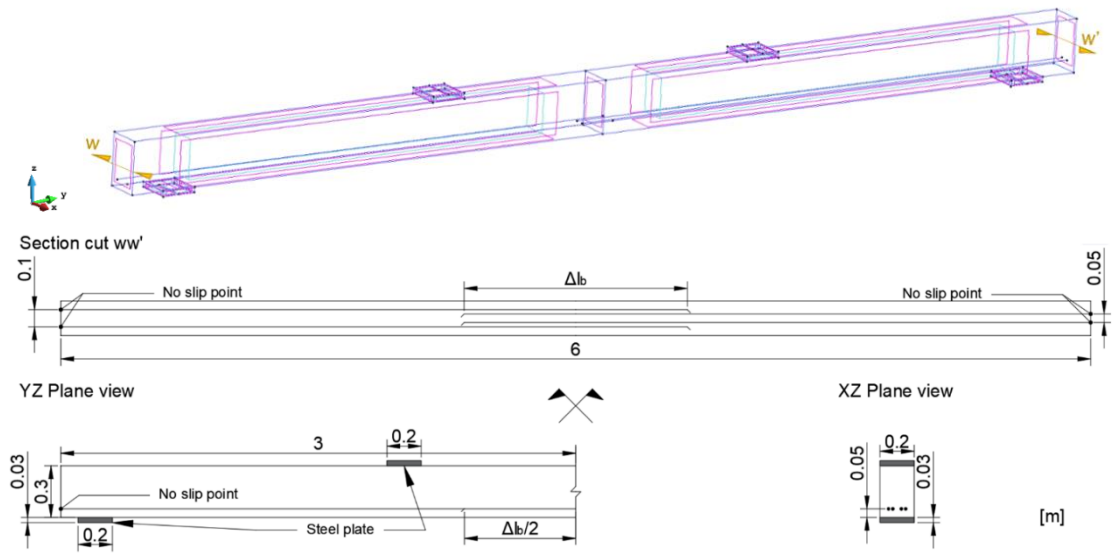


Figure 34 – Geometry of the lap-splice beam model (LSB model).

#### 4.3.3.2 Material parameters

The parameters used for the concrete material of both the SAB and LSB models were those catalogued in Eurocode 2 for a C25/30 concrete with mean values and the reinforcement elements were assigned a steel material with the mean values of a B500C class steel. The support/loading plates were assigned the same material used in the auxiliary ME of the pull-out models. The material parameters for each element are represented in Table 18. Note that $\upsilon$ represents the Poisson's ratio.

Table 18 – Material parameters for the Lap-splice beam model.

| *Concrete* | | |
|---|---|---|
| $f_c$ | 33 | MPa |
| $f_t$ | 2.6 | MPa |
| $E$ | 31 | GPa |
| $\upsilon$ | 0.2 | - |

| *Reinforcement* | | |
|---|---|---|
| $f_y$ | 550 | MPa |
| $R_m$ | 575 | MPa |
| $E$ | 200 | GPa |
| $A_{gt}$ | 0.075 | - |

| *Loading/Support Plates* | | |
|---|---|---|
| $E$ | 32 | GPa |
| $\upsilon$ | 0.3 | - |

The bond model assigned to the reinforcing bars was defined by the user as intended. The slip was restrained where the bars are contacting the beam's lateral surfaces to simulate the restrained slip of a hooked anchorage.

#### 4.3.3.3 Loading history

The loading history of the SAB model consists of a single point load applied at the centre point of the top plate and two simple supports applied along a centre line parallel to the X-axis on the bottom plates. The analysis was performed using the Newton-Raphson method and was set to run for 100 steps, with a limit of 40 iterations per step, until the loading value reached 80 kN, which was chosen to obtain the entirety of the bond stress-slip curve. Also, the beam model mesh generated 2880 linear hexahedral elements in the concrete region and 225 tetrahedral elements divided among the three plates.

The loading history of the LSB model consists of two point loads applied at the centre points of the top plates and two simple supports applied along a centre line parallel to the X-axis on the bottom plates. Once again, the analysis was performed using the Newton-Raphson method, and for this model, it was set to run for 100 steps, with a limit of 40 iterations per step, until the loading value at each plate reached 40 kN. The loading level was chosen to enable the results to capture the most important part of the bond stress-slip curve (i.e. the ascending branch, the bond strength plateau and the beginning of the descending branch). Similarly to the previous one, the beam model mesh generated 2880 linear hexahedral elements in the concrete region and 301 tetrahedral elements divided among the four plates.

Regarding the limit number of iterations per step, the number chosen took into account the error of the several convergence criteria utilised by the ATENA software, which should be kept lower than 10% to achieve reliable results.

Additionally, several monitoring points were configured on the model to measure the external force being applied at the top plates, the deflection of the beam at mid-span and the bond stress and slip values across the length of the anchorage/lap-splice. The load cases and mesh for both the SAB and LSB models are depicted in Figure 35.

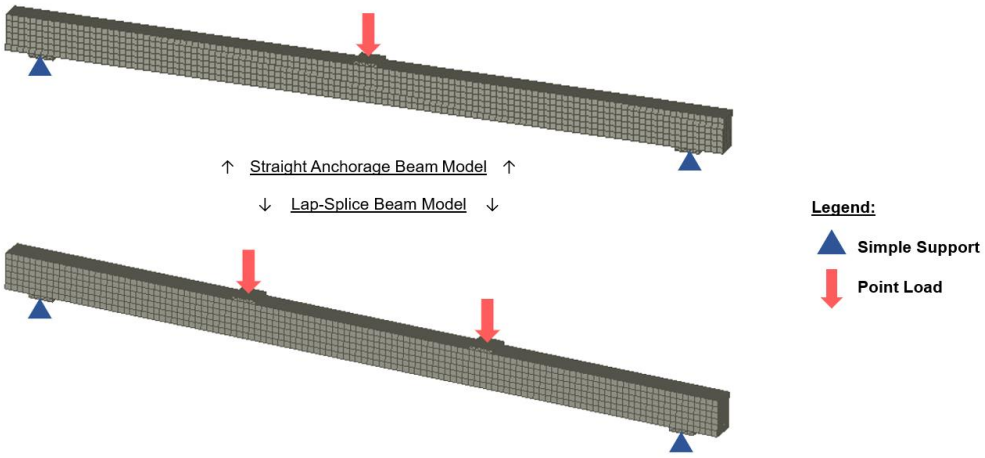


Figure 35 – 3D view of both beam models with the generated mesh and labelled load cases.

# 5. Discussion of the numerical analysis results

## 5.1 Introduction

The results from the numerical analysis performed on the pull-out and beam models will be presented, analysed, and discussed throughout the following chapter. In the case of the pull-out model, results concerning the reference models will be presented to evidence the local bond behaviour model's validation. Subsequently, the results from the numerical simulations carried out for each experimental test series performed by Louro (2014), Freitas (2016) and Pereira (2019) are presented. For a given test series, the various known bond models, including the recently calibrated one, were employed in the numerical analysis to compare experimental and numerical results.

Regarding the two beam models (SAB and LSB models), the goal of the numerical analysis was to establish the anchorage/lap-splice length necessary for a given local bond strength level. The results from this exercise are presented to provide an idea of the influence that different types of concrete or reinforcing bars can have in the performance of anchored/lap-spliced bars.

## 5.2 Discussion of the pull-out model's results

### 5.2.1 Results of the reference models

The four reference models were subjected to a validation process to ensure that the obtained results were in accordance with what was expected from this type of experiment. The models were tested during the validation process using a C30/37 concrete material, a B500C steel material and considering the *fib* Model Code 2010 bond model.

Overall, the models successfully captured the bond behaviour of a short length embedded bar, as depicted in Figures 36 and 37. Results showed that the bond stress starts to increase at the beginning of the embedded length, quickly reaching a mean bond stress value that remains the same throughout the remaining bonded length; this is clearly shown by the fact that the monitored values at the middle and end of the embedded length of the bar agree throughout the analysis.

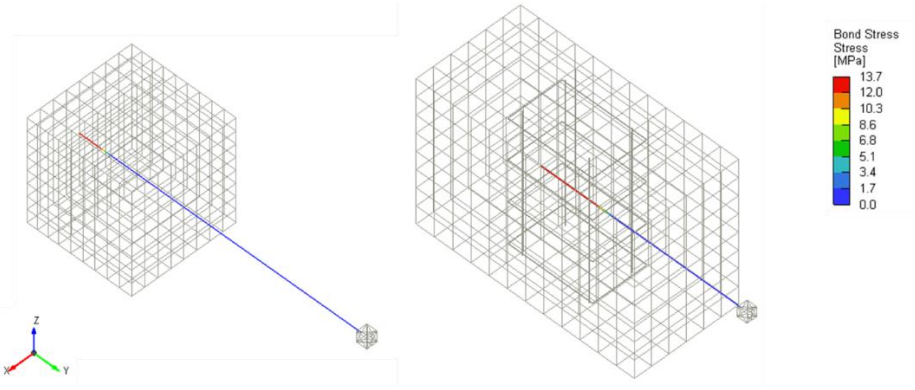


Figure 36 – 3D diagram for the bond stress at peak for the Standard_12 (left) and Modified_25 (right) reference models.

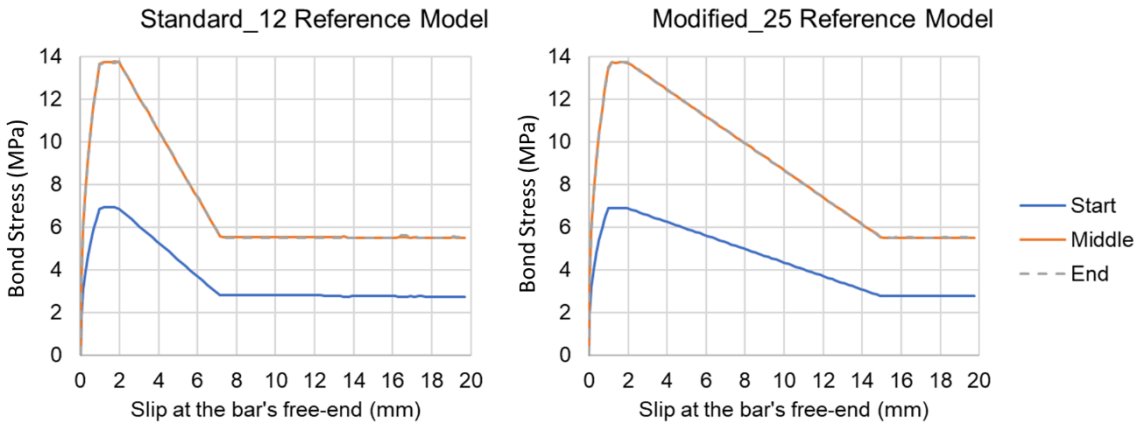


Figure 37 – Bond stress versus slip at the bar's free-end: registry of the monitoring points located at the beginning, middle and end of the embedded length of the bars for the Standard_12 (left) and Modified_25 (right) models.

Observation of the cracking pattern development during the analysis was consistent with the literature concerning the ductile pull-out failure. Figures 38 and 39 depict how the degradation of the tensile strength occurs with increasing slip around the reinforcing's bar free-end of the embedded length, both in the Standard_12 and Modified_25 models. Eventually, this degradation would lead to the radial crack pattern in the concrete core obtained at the end of the numerical analysis and displayed for both reference models in Figure 40.

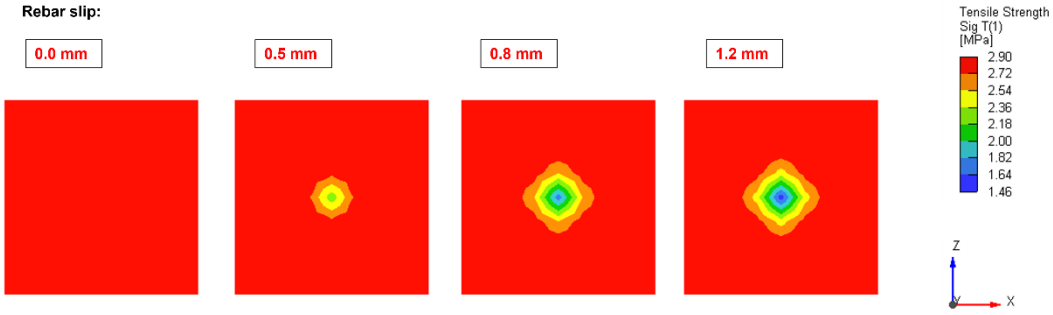


Figure 38 – Standard_12 reference model: degradation of the tensile strength in the surface of the reinforcing's bar free end.

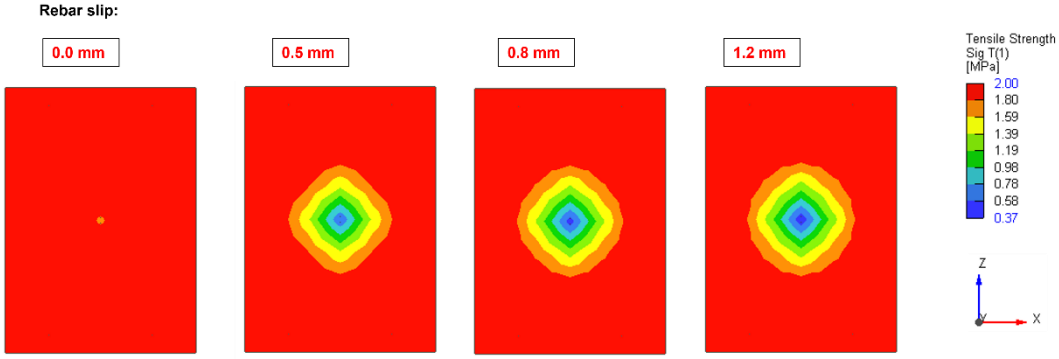


Figure 39 – Modified_25 reference model: degradation of the tensile strength in the surface of the reinforcing's bar free end.

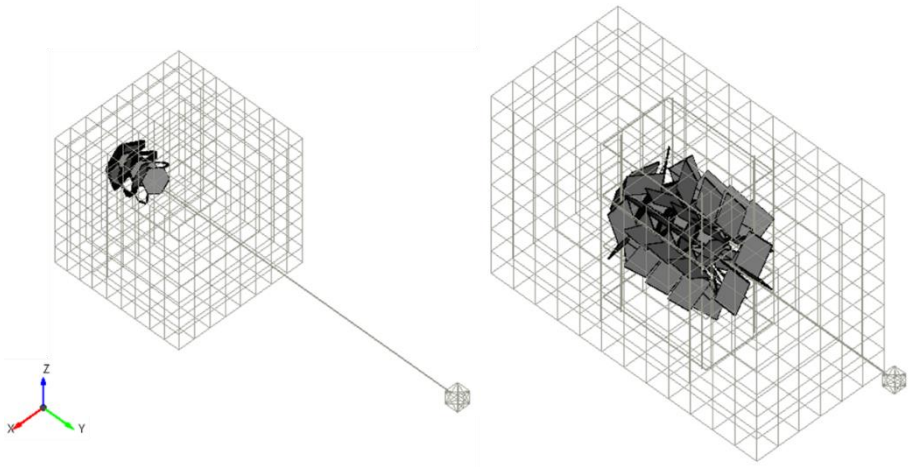

Figure 40 – Standard_12 (left) and Modified_25 (right) reference models: cracking pattern at the end of the analysis.

The validation of the reference models also involved a sensitivity analysis of the material parameters. This process confirmed that the bond behaviour of the reinforcing bars modelled heavily depends on the bond function assigned to the bars and suffers a slight to no variation whilst varying the remaining material properties. However, the models presented a large variation in results when running the analysis with a more or less refined mesh. While the bond stress-slip response suffered no alteration by modifying the mesh, the registered external force measured at the auxiliary ME, where the imposed displacement was applied, significantly changed. This aspect was considered relevant since, experimentally, the bond stress measurements are performed indirectly through the tension force values registered by the hydraulic machine, which are then put through the calculation of expression (2). Thus it was considered important that the numerical bond stress results measured at the monitoring points would agree with the external force results when using the aforementioned expression.

Despite not being able to perfectly adjust the monitored bond stress and external force results, the difference between these was kept close to ±10%, as shown in Table 19. It was observed that refined meshes would increase the external force applied to the model, which enabled a better adjustment of the $\tau_{bmax}$ values measured at the monitoring points; however, the cracking pattern that would be developed in certain situations did not match the expected pull-out failure, thus making these results unreliable. Despite lacking the knowledge to justify these outcomes, the author believes that the user interface ATENA 3D was found unreliable in some situations and would recommend future works to model pull-out specimens in the GiD user interface to avoid this problem. This opinion is based on the fact that whilst attempting to model the equal structures in both user interfaces, ATENA 3D incomprehensibly delivered consistently bad results. Independent of this fact, the pull-out reference models were, overall, successful in reproducing the bond behaviour of the pull-out test experiment.

Table 19 – Difference between $\tau_{bmax}$ values measured at the monitoring point or through conversion of the external force value.

| Standard 12 | Standard 16 | Modified 16 | Modified 25 |
|---|---|---|---|
| 13.7% | 10.7% | 7.4% | 11.5% |

### 5.2.2 Comparison between experimental and numerical results

In the present section, a comparison will be presented between the experimental bond stress-slip curves of the pull-out test series performed by Louro (2014), Freitas (2016) and Pereira (2019) and the bond stress-slip curves obtained from the numerical analysis of the pull-out model using the various known bond models to simulate the bond behaviour. Furthermore, comparisons of the results will be discussed in different sections concerning the concrete type of each test series, i.e. LBC, LCRAC or OC. Furthermore, a comparison of the results will be presented using tables containing the bond strength values of each test series and the respective deviation to accuracy errors for the predictions of each bond model, as well as graphics that will include both numerical and experimental results. Each section will present these data, and its discussion will be provided in the following pages.

Regarding the graphics, the experimental results will appear in a greyed-out area that encompasses the minimum and maximum bond stress-slip results of all specimens belonging to the related test series. Additionally, a mean bond stress-slip curve was calculated and plotted for each test series to support the comparison with the numerical results. Figure 41 provides an example of the previously described data treatment for the case of the LBC_0,84_Alfred test series. Consequently, the bond stress-slip curves resulting from the numerical analysis will be presented as coloured lines appropriately identified with the employed bond model.

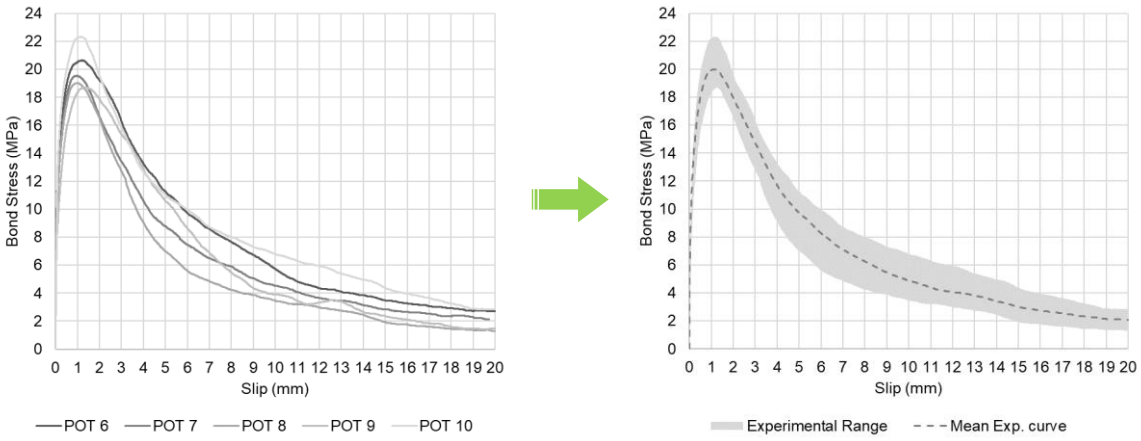


Figure 41 – Example of the graphical presentation of the experimental results for comparison and discussion.

#### 5.2.2.1 Low binder concrete

The low binder concrete data set consists of 12 pull-out test series performed between Freitas (2016) and Pereira (2019). Comparisons between experimental and numerical results for bond strength using the various bond models are presented in Table 20. In addition, the graphical comparisons between experimental and numerical bond stress-slip curves are displayed in Figures 42 and 43.

Table 20 – Comparison of bond strength results for test series involving LBC.

| Results >> | Mean Exp. | Numerical | | | | | | | | | |
|---|---|---|---|---|---|---|---|---|---|---|---|
| Bond Model >> | | fib MC2010 | | Louro (2014) | | Freitas (2016) | | Pereira (2019) | | New Model | |
| | $\tau_{dmax}$ (MPa) | $\tau_{bmax}$ (MPa) | Δ | $\tau_{bmax}$ (MPa) | Δ | $\tau_{bmax}$ (MPa) | Δ | $\tau_{bmax}$ (MPa) | Δ | $\tau_{bmax}$ (MPa) | Δ |
| **LBC_0,86_Alfred** | 25.89 | 14.03 | 84.52% | 14.14 | 83.03% | 24.61 | **5.17%** | 23.53 | **9.99%** | 25.30 | **2.30%** |
| **LBC_0,84_Alfred** | 19.98 | 11.24 | 77.86% | 11.66 | 71.34% | 19.17 | **4.22%** | 17.23 | 16.02% | 16.96 | 17.83% |
| **LBC_0,82_Alfred** | 13.40 | 9.59 | 39.77% | 9.95 | 34.64% | 14.80 | **-9.47%** | 12.83 | **4.41%** | 12.56 | **6.64%** |
| **LBC_0,86_Faury** | 23.33 | 12.97 | 79.93% | 13.46 | 73.33% | 23.67 | **-1.42%** | 22.40 | **4.16%** | 24.08 | **-3.12%** |
| **LBC125_A12** | 24.42 | 12.79 | 91.02% | 13.27 | 84.02% | 25.68 | **-4.87%** | 22.86 | **6.85%** | 24.58 | **-0.62%** |
| **LBC125_i12** | 20.68 | 12.79 | 61.77% | 13.27 | 55.84% | 19.62 | **5.40%** | 20.80 | **-0.56%** | 22.37 | **-7.52%** |
| **LBC75_A12** | 21.15 | 10.35 | 104.32% | 10.74 | 96.83% | 21.74 | **-2.71%** | 18.50 | 14.29% | 19.89 | **6.30%** |
| **LBC75_i12** | 16.06 | 10.35 | 55.16% | 10.74 | 49.47% | 16.84 | **-4.63%** | 16.84 | **-4.62%** | 18.10 | **-11.30%** |
| **LBC125_A16** | 22.26 | 12.79 | 74.06% | 13.27 | 67.68% | 21.64 | **2.84%** | 21.49 | **3.58%** | 20.68 | **7.63%** |
| **LBC125_i16** | 21.57 | 12.79 | 68.69% | 13.27 | 62.50% | 21.64 | **-0.34%** | 21.49 | **0.38%** | 20.68 | **4.31%** |
| **LBC75_A16** | 18.64 | 10.35 | 80.12% | 10.74 | 73.51% | 18.47 | **0.93%** | 17.39 | **7.18%** | 16.74 | 11.37% |
| **LBC75_i16** | 16.49 | 10.35 | 59.29% | 10.74 | 53.45% | 18.47 | **-10.74%** | 17.39 | **-5.21%** | 16.74 | **-1.50%** |
| Δmax | | | 104.32% | | 96.83% | | 5.40% | | 16.02% | | 17.83% |
| Δmin | | | 39.77% | | 34.64% | | -10.74% | | -5.21% | | -11.30% |
| Δrange | | | 144.09% | | 131.47% | | 16.14% | | 21.23% | | 29.12% |
| Δmean | | | 73.04% | | 67.14% | | -1.30% | | 4.71% | | 2.69% |
| Δmedian | | | 75.96% | | 69.51% | | -0.88% | | 4.28% | | 3.30% |

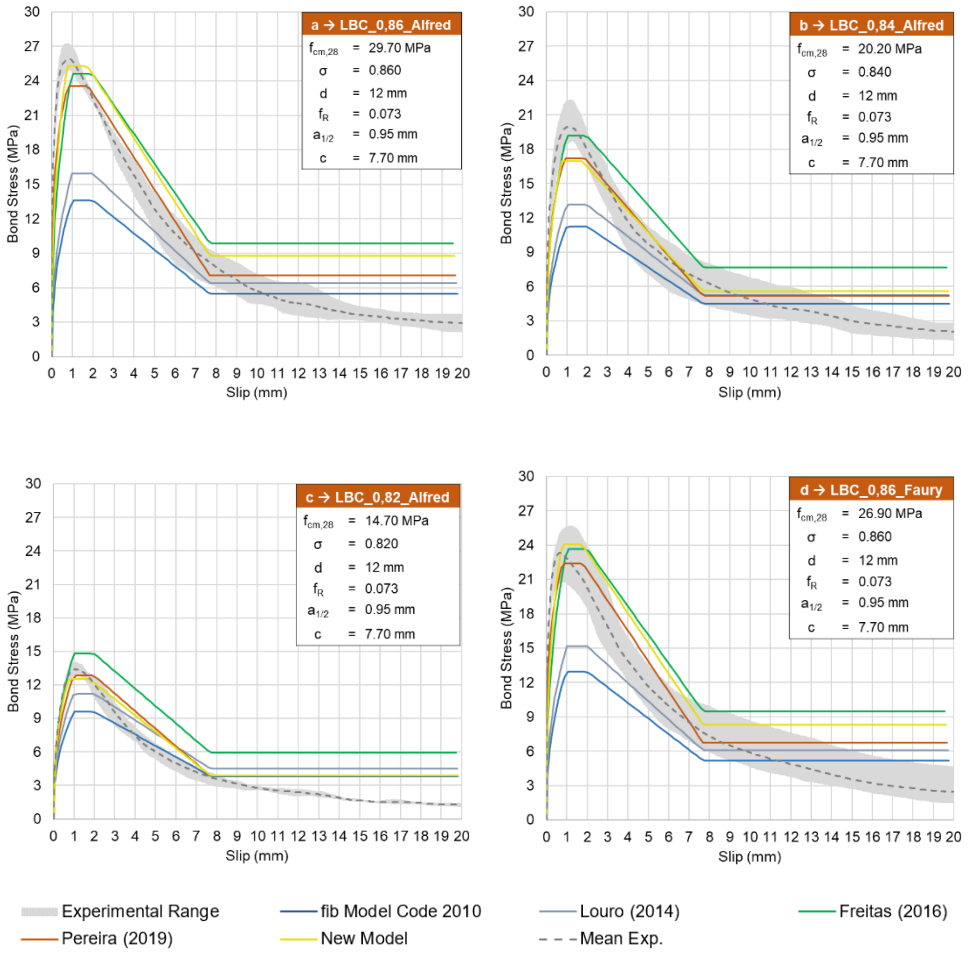


Figure 42 – Comparison of bond stress-slip curve results for the LBC test series of Pereira (2019).

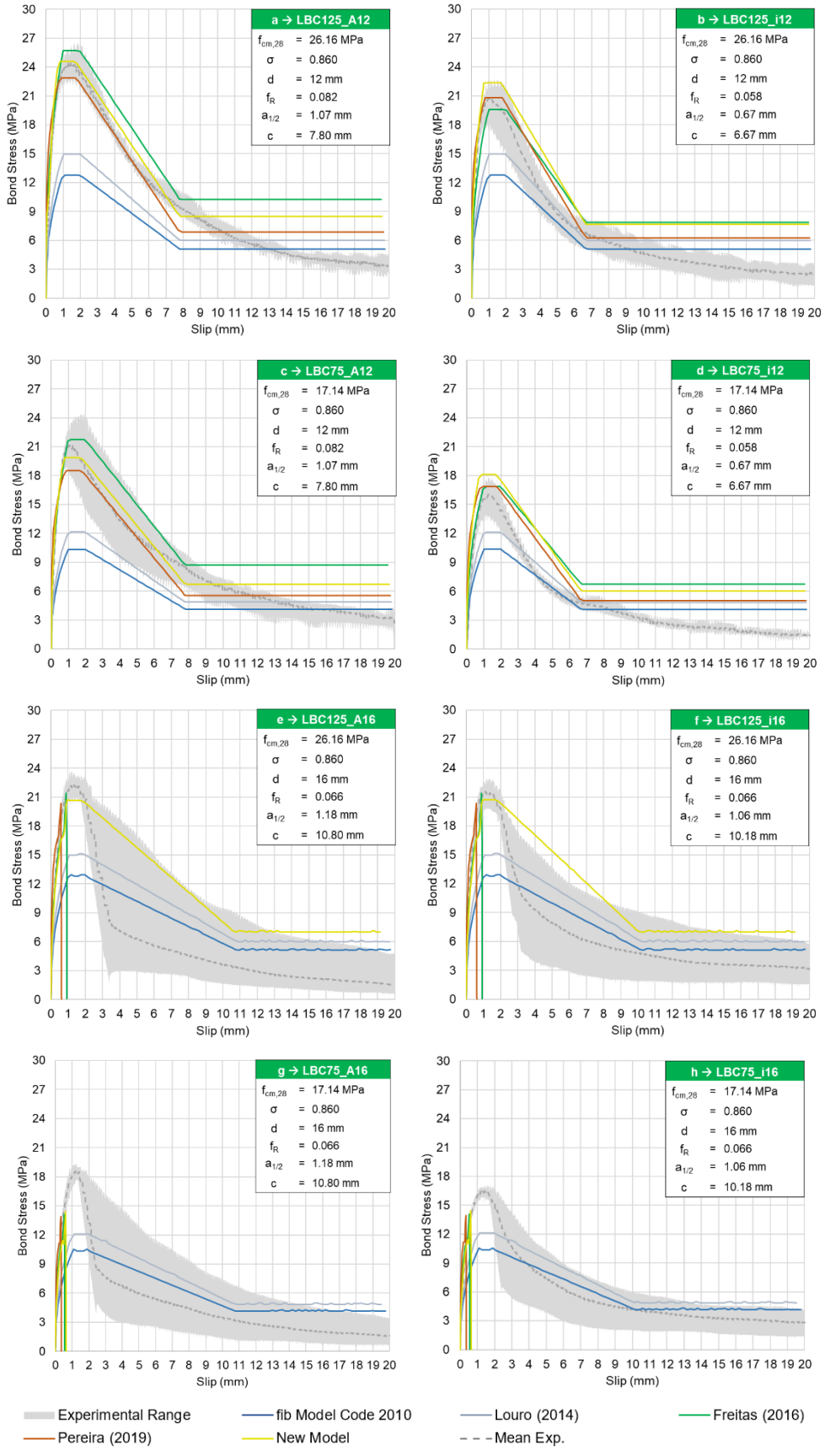


Figure 43 – Comparison of bond stress-slip curve results for the LBC test series of Freitas (2016).

From the comparison of the obtained results, it is possible to assess that considering mainly $\sqrt{f_c}$ to predict the local bond strength of small diameter bars embedded in LBC is a conservative and reliable approach, as shown by the bond models from *fib* Model Code 2010 and Louro (2014) (mean error of 73 and 67%, respectively). Even so, for a more precise estimation, it should be taken into account the influence of other bond-related parameters, such as the packing density, as it happens in the new calibrated model and the models from Freitas (2016) and Pereira (2019). The results of the bond models that account for the influence of $\sigma$ had much closer predictions (although not always conservative) for series where $f_R$ remains the same, whilst the $\sigma$ varies (see Figure 42 a), b) and c)). The high packing density values of LBC seem to greatly influence the local bond behaviour, enabling high bond resistance stresses to be achieved whilst having a low to moderate concrete compressive strength (e.g. series LBC_0,84_Alfred and LBC75_A12).

Nevertheless, the bond models capable of predicting high bond strength values often yield non-conservative results, which can be explained by several factors that were difficult to address during calibration. For example, predictions tend to be more non-conservative when stainless-steel reinforcement is used; compared to their equivalent regular steel reinforcing bars, the stainless-steel reinforcing bars have a different surface, affecting both chemical adhesion and active friction, which should influence the bond stress-slip relationship in its initial and final stages. As is noticeable, this variable was not accounted for in the calibration of the new bond model.

In terms of slip values and the initial bond stiffness, in general, the bond models present conservative results within the ascending branch and plateau of the bond stress-slip curve for the test series of Pereira (2019) (see Figure 42), meaning that the experimental results tend to present a stiffer bond behaviour on the initial stages. However, this tendency is reversed in the series performed by Freitas (2016), as the experimental ascending branch has significantly less initial stiffness in all cases (see Figure 43). Although there is no clear evidence for this discrepancy between the results of both authors, there is a possibility that the concrete composition used by each is an influencing factor. As shown in Table 3 Table 4, Pereira (2019) used 125 kg/m$^3$ of fly-ash in his concrete mixtures, whereas Freitas (2016) used 125 kg/m$^3$ of limestone filler in the LBC125 mixture and 75 kg/m$^3$ of limestone filler, plus 100 kg/m$^3$ of fly-ash in the LBC75 mixtures. Therefore, the use of larger quantities of fly-ash by Pereira (2019) may have been the cause for the better initial stiffness presented in his experimental results in opposition to those of Freitas (2016). Moreover, it is also plausible that the initial bond stiffness differences can be due to the different packing optimisation curves used since Pereira (2019) utilised the Alfred and Faury curves, whereas Freitas (2016) employed the Funk and Dinger curve. Regardless of which factor impacted the results, this is another example of a variable not possible to account for in the calibration of the new model to provide better results.

Looking at the results in the descending branch and residual bond strength of the bond stress-slip curves, all models tend to become less conservative to non-conservative by going near or above the experimental mean line of the test series. This non-conservative tendency can be attributed to the 1 mm length that all models adopt for the bond strength plateau, which overextends maximum resistant bond capacity compared to the experimental results, which seem to drop very early once the peak value is

reached. This sudden drop can be related to the low values of rib spacing exhibited by all these low diameter bars, although such a statement would require further testing to be confirmed.

A special mention should be made to the LBC series performed by Freitas (2016) using the 16 mm diameter reinforcing bars, which all exhibited a brittle failure by splitting (see Figure 43 e), f), g) and h)) in a considerable number of specimens. This change in failure mode explains the unusual mean bond stress drop post-peak seen in the comparisons. Despite the tests following the directives from EN 10080:2005 – Annex D that intended to prevent this type of failure, the high bond strength values achieved by the high packing density levels of the LBC mixture induced an unexpected response, leading to the confinement levels assured by the standard not to be enough to control the sudden concrete cracking up to the surface and the subsequent brittle failure mode. In terms of numerical results, some of the bond models were able to predict the splitting failure successfully, as was the case of the new bond model in Figure 43 e) and f) and the models of Freitas (2016) and Pereira (2019), in all four cases. However, the remaining bond models were unsuccessful in predicting the splitting failure since their predictions for bond strength in these test series were too conservative.

Despite the models' ability to predict the splitting failure, the numerical bond stress-slip curves do not follow the experimental curves due to the phenomenological modelling adopted for simulating the bond behaviour in the FE analysis. According to the bond model, The reinforcing bars have a pull-out failure prescribed, which they try to accommodate during the analysis; however, when the bond stress is too high, it generates tensile stresses in the surrounding concrete that lead to severe cracking that extends beyond the core of the specimen and reaches the surface. Thus the pull-out model displays a cracking pattern associated in the literature with the failure by splitting. Nevertheless, the bond stress-slip curve can only register a sudden drop in stress and no further progression in slip, given that it cannot follow the prescribed bond function assigned to the reinforcement due to the cracking of the concrete around the bar. These facts can be attested by the render of the cracking pattern displayed in Figure 44 from the results relative to the bond model from Freitas (2016) presented in Figure 43 e).

Even though some numerical models could identify the correct failure mode, the maximum bond stresses achieved were not always close to those registered experimentally. Furthermore, it was found that the size of the mesh has a great influence on the cracking pattern (which is modelled according to a smeared approach), and the author would recommend in the future the use of the GiD user interface as opposed to the ATENA 3D user interface, to perform the modelling of these specimens as a way to solve this problem, since ATENA 3D showed to be unreliable in certain cases.

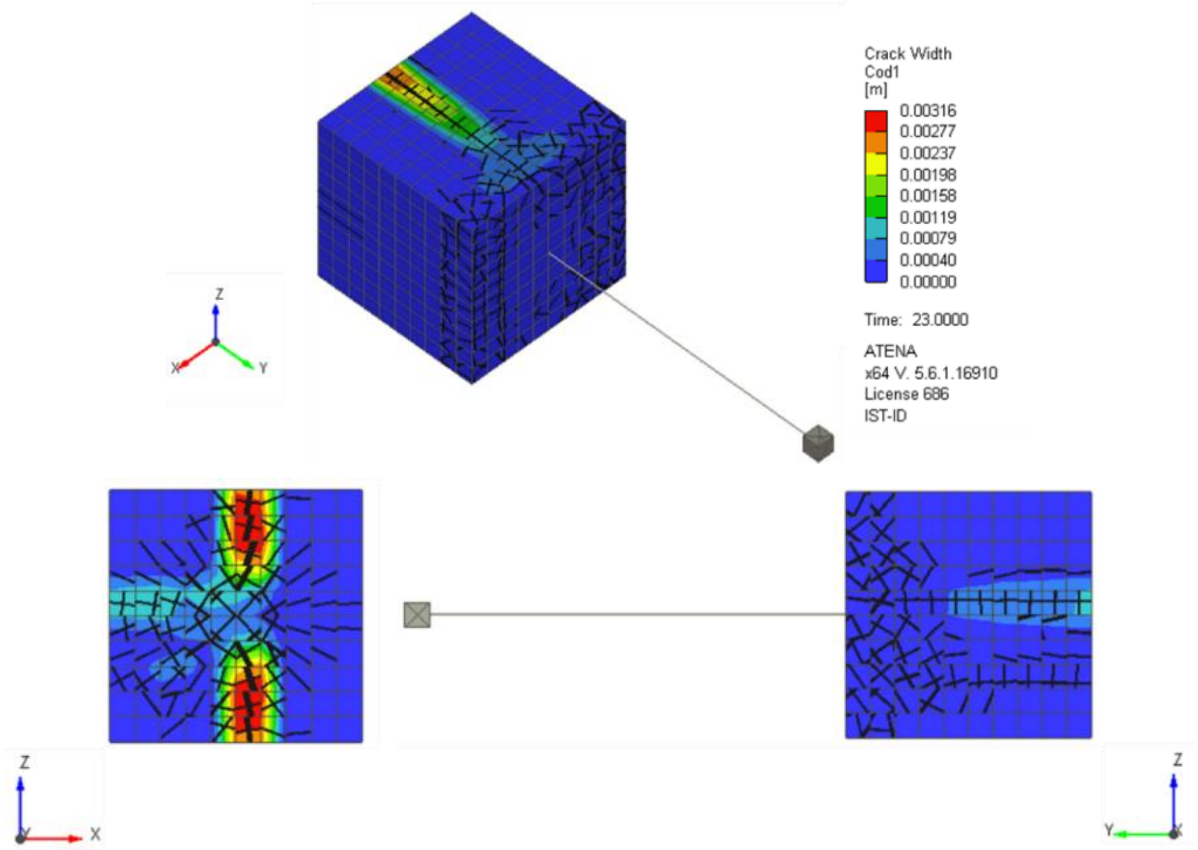


Figure 44 – The cracking pattern of a fragile failure by splitting

### 5.2.2.2 Low cement recycled aggregate concrete

Pereira (2019) performed 3 test series comprising 15 pull-out test specimens made with LCRAC, a limited data sample. Nonetheless, the comparisons between experimental and numerical results for bond strength are presented in Table 21, and the bond stress-slip curves are depicted in Figure 45.

Table 21 – Comparison of bond strength results for test series involving LCRAC.

| **Results >>** | **Mean Exp.** | **Numerical** | | | | | | | | | |
|---|---|---|---|---|---|---|---|---|---|---|---|
| **Bond Model >>** | | **fib MC2010** | | **Louro (2014)** | | **Freitas (2016)** | | **Pereira (2019)** | | **New Model** | |
| | $T_{dmax}$ (MPa) | $T_{bmax}$ (MPa) | Δ | $T_{bmax}$ (MPa) | Δ | $T_{bmax}$ (MPa) | Δ | $T_{bmax}$ (MPa) | Δ | $T_{bmax}$ (MPa) | Δ |
| **LCRAC_30** | 23.36 | 12.37 | 88.76% | 12.85 | 81.84% | 20.81 | 12.22% | 18.97 | 23.13% | 23.36 | 0.00% |
| **LCRAC_55** | 16.81 | 10.98 | 53.09% | 11.40 | 47.48% | 18.81 | **-10.62%** | 15.20 | 10.61% | 16.81 | 0.00% |
| **LCRAC_80** | 12.66 | 9.84 | 28.62% | 10.22 | 23.91% | 17.17 | **-26.26%** | 10.10 | 25.32% | 12.66 | 0.00% |
| Δmax | | | 88.76% | | 81.84% | | 12.22% | | 25.32% | | 0.00% |
| Δmin | | | 28.62% | | 23.91% | | -26.26% | | 10.61% | | 0.00% |
| Δrange | | | 117.38% | | 105.74% | | 38.48% | | 35.93% | | 0.00% |
| Δmean | | | 56.82% | | 51.07% | | -8.22% | | 19.68% | | 0.00% |
| Δmedian | | | 53.09% | | 47.48% | | -10.62% | | 23.13% | | 0.00% |

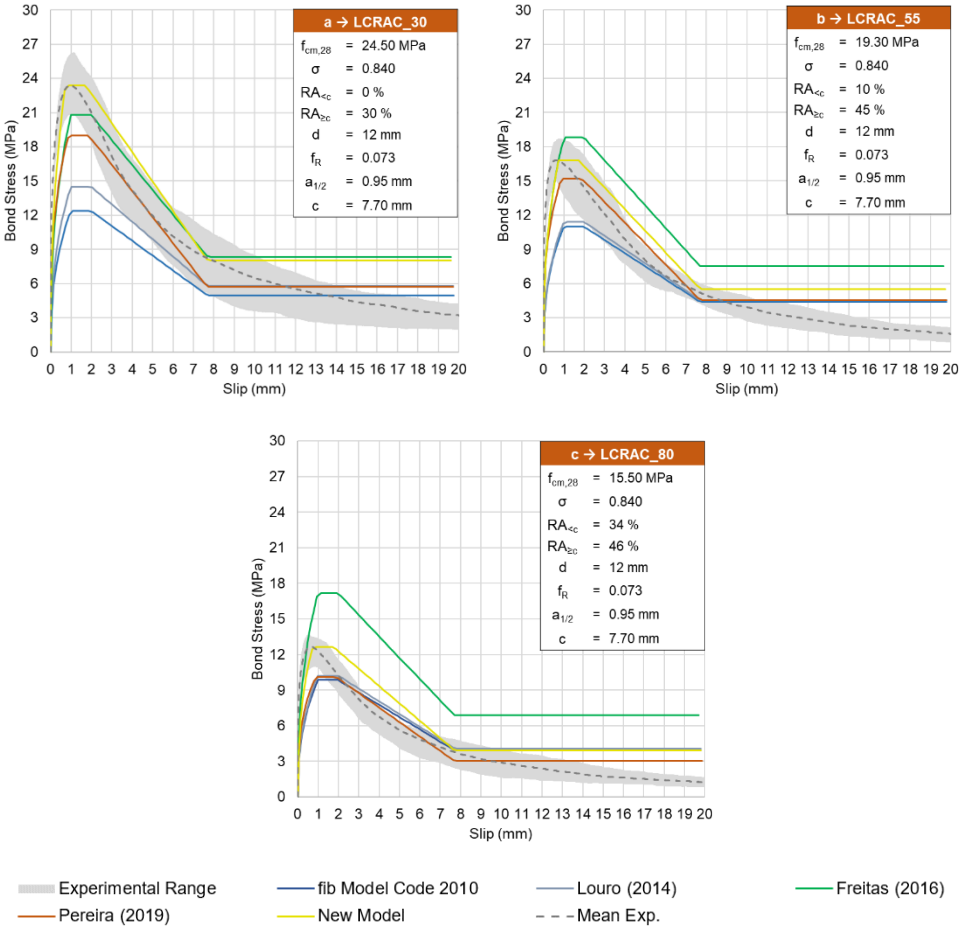


Figure 45 – Comparison of bond stress-slip curve results for the LCRAC test series of Pereira (2019).

Overall, except for the bond model from Freitas (2016), the predictions obtained from the numerical results regarding the local bond behaviour of embedded reinforcement in LCRAC range from good to conservative, both in terms of bond resistance and stiffness. The models from fib Model Code 2010 and Louro (2014) are the most conservative regarding the bond strength, with the gap between these two models and the remaining ones getting shorter when the RA content increases substantially, and the concrete compressive strength decreases simultaneously (see the progression from Figure 45 a) through c). On the other hand, the model from Freitas (2016) is not able to provide good results when the content of RA of smaller size increases since this signifies a decrease in bond strength and the model, which is very dependent on the variation of the packing density, continues to deliver high-value estimations. Overall, the absence of coefficients regarding the various facets of RA content influence over the local bond behaviour compromises the ability of these pre-existing bond models to provide precise predictions for this type of concrete mixtures.

The exact predictions for the bond strength made by the new calibrated model for all three LCRAC series are mainly due to the calibrated coefficients concerning the influence of $RA_{<c}$ and $RA_{\geq c}$ and the fact that the data sample considered for their calibration is very limited, compared to the other parameters. Right now it is still early to assume this model as a good predictor of LCRAC local bond behaviour because there is a high probability that a recalibration based on a larger data sample would return major improvements. Nevertheless, it enables the study of the subject in a preliminary stage and

offers an overall perception of how RA content can influence the local bond: the RA establishes a size relationship with the reinforcing's bar ribs, with larger sized aggregates seemingly improving the bond to a certain extent and smaller aggregates being detrimental. Furthermore, the detrimental influence of RA of size lower than the rib spacing is made quite clear in this series: even with moderately high values of packing density, the series containing various levels of $RA_{<c}$ suffer a large decrease in bond strength, while the value for $RA_{\geq c}$ remains almost the same.

Regarding the initial bond stiffness, the inclusion of RA into the concrete mixture leads to a stiffer bond performance overall, since all LCRAC series achieve peak bond stress at slip values below 1.0 mm, contrary to their reference LBC series (see Figure 45 b), which extends past this limit; however, this might only be due to the small sample size. In general, all models predict a conservative ascending branch, with higher slip values than those observed experimentally, despite RA inclusion not directly influencing the $\tau_b - s$ curve in this respect.

#### 5.2.2.3 Ordinary concrete

Between Louro (2014) and Freitas (2016), there were a total of 16 pull-out test series involving OC performed using 12, 16 and 25 mm diameter reinforcing bars. Once again, experimental and numerical bond strength results are compared and presented in Table 22. In addition, the graphical comparison between each experimental series' bond stress-slip curve and the numerical results using each bond model are shown in Figure 46, 47 and 48.

Table 22 – Comparison of bond strength results for test series involving OC.

| **Results >>** | **Mean Exp.** | **Numerical** | | | | | | | | | |
|---|---|---|---|---|---|---|---|---|---|---|---|
| **Bond Model >>** | | **fib MC2010** | | **Louro (2014)** | | **Freitas (2016)** | | **Pereira (2019)** | | **New Model** | |
| | $\tau_{dmax}$ (MPa) | $\tau_{bmax}$ (MPa) | Δ | $\tau_{bmax}$ (MPa) | Δ | $\tau_{bmax}$ (MPa) | Δ | $\tau_{bmax}$ (MPa) | Δ | $\tau_{bmax}$ (MPa) | Δ |
| **C250_A12** | 20.02 | 14.03 | 42.69% | 14.56 | 37.46% | 22.68 | **-11.76%** | 18.03 | 11.05% | 18.40 | **8.82%** |
| **C250_i12** | 15.38 | 14.03 | **9.61%** | 14.56 | **5.59%** | 16.05 | -4.17% | 16.40 | -6.26% | 16.74 | -8.14% |
| **C250_A16** | 18.70 | 14.03 | 33.30% | 14.56 | 28.41% | 18.26 | **2.42%** | 16.94 | 10.37% | 15.48 | 20.83% |
| **C250_i16** | 16.21 | 14.03 | 15.56% | 14.56 | 11.33% | 18.26 | **-11.21%** | 16.94 | -4.32% | 15.48 | **4.75%** |
| **A_C1_16** | 14.76 | 15.19 | -2.78% | 15.76 | -6.34% | 22.86 | **-35.41%** | 17.31 | **-14.71%** | 17.78 | **-16.95%** |
| **B_C1_16** | 17.91 | 15.19 | 17.95% | 17.78 | **0.76%** | 32.05 | **-44.11%** | 24.66 | **-27.35%** | 21.46 | **-16.54%** |
| **AT_C1_16** | 16.36 | 15.19 | **7.75%** | 15.76 | **3.80%** | 22.56 | **-27.46%** | 17.24 | -5.11% | 17.71 | -7.60% |
| **BT_C1_16** | 16.57 | 15.19 | **9.12%** | 17.78 | -6.78% | 31.75 | **-47.80%** | 24.57 | **-32.55%** | 21.39 | **-22.51%** |
| **A_C2_16** | 22.14 | 18.67 | 18.60% | 19.38 | 14.25% | 26.82 | **-17.45%** | 18.29 | 21.08% | 23.42 | -5.47% |
| **AT_C2_16** | 23.86 | 18.67 | 27.81% | 19.38 | 23.13% | 26.45 | -9.79% | 18.22 | 30.98% | 23.33 | **2.27%** |
| **A_C1_25** | 17.28 | 15.19 | 13.80% | 17.78 | -2.79% | 27.35 | **-36.81%** | 18.29 | -5.50% | 13.83 | 24.99% |
| **B_C1_25** | 15.88 | 15.19 | **4.54%** | 17.78 | **-10.70%** | 28.85 | **-44.97%** | 18.61 | **-14.71%** | 14.07 | 12.81% |
| **AT_C1_25** | 14.33 | 15.19 | -5.62% | 17.78 | **-19.38%** | 31.45 | **-54.43%** | 24.48 | **-41.46%** | 15.69 | -8.65% |
| **BT_C1_25** | 14.36 | 15.19 | -5.41% | 17.78 | **-19.20%** | 32.65 | **-56.00%** | 24.83 | **-42.15%** | 15.91 | -9.73% |
| **A_C2_25** | 17.27 | 18.67 | -7.49% | 21.85 | **-20.97%** | 32.34 | **-46.60%** | 19.32 | **-10.60%** | 18.22 | -5.18% |
| **B_C2_25** | 17.17 | 18.67 | -8.04% | 21.85 | **-21.44%** | 32.71 | **-47.52%** | 24.57 | **-30.13%** | 18.28 | -6.09% |
| Δmax | | | 42.69% | | 37.46% | | 2.42% | | 30.98% | | 24.99% |
| Δmin | | | -8.04% | | -21.44% | | -56.00% | | -42.15% | | -22.51% |
| Δrange | | | 50.73% | | 58.90% | | 58.42% | | 73.13% | | 47.50% |
| Δmean | | | 10.71% | | 1.07% | | -30.82% | | -10.08% | | -2.03% |
| Δmedian | | | 9.37% | | -1.01% | | -36.11% | | -8.43% | | -5.78% |

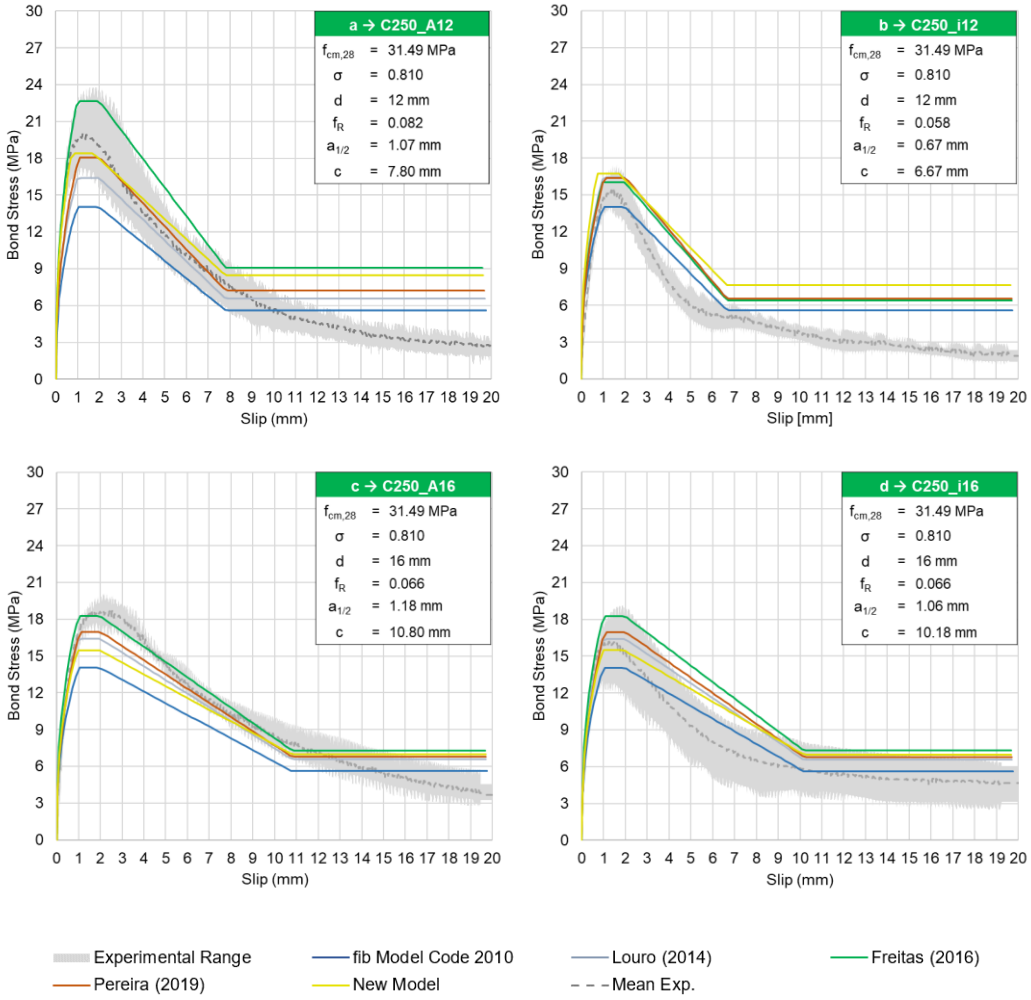


Figure 46 – Comparison of bond stress-slip curve results for the OC test series of Freitas (2016).

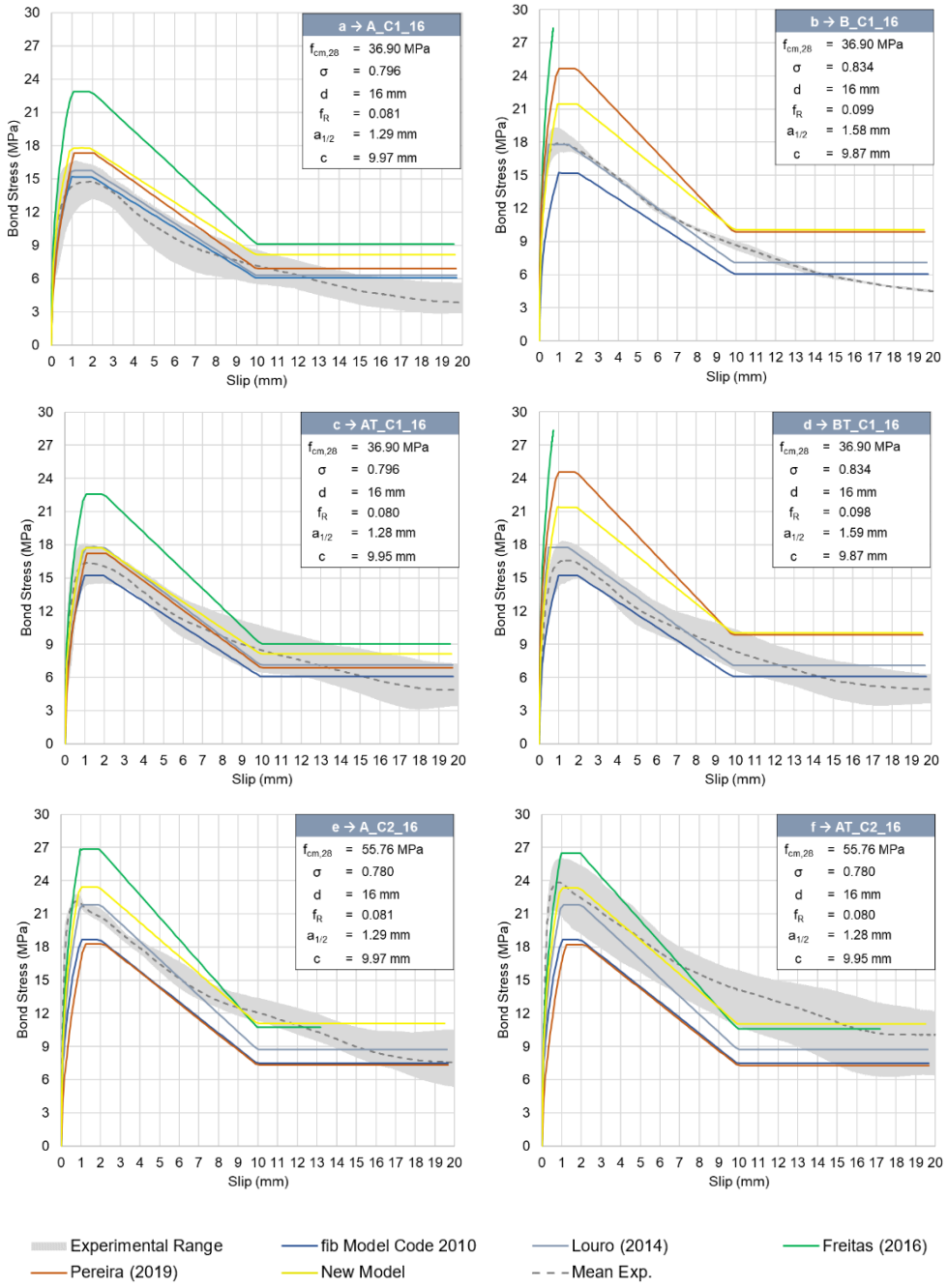


Figure 47 – Comparison of bond stress-slip curve results for the OC test series of Louro (2014) with d=16 mm.

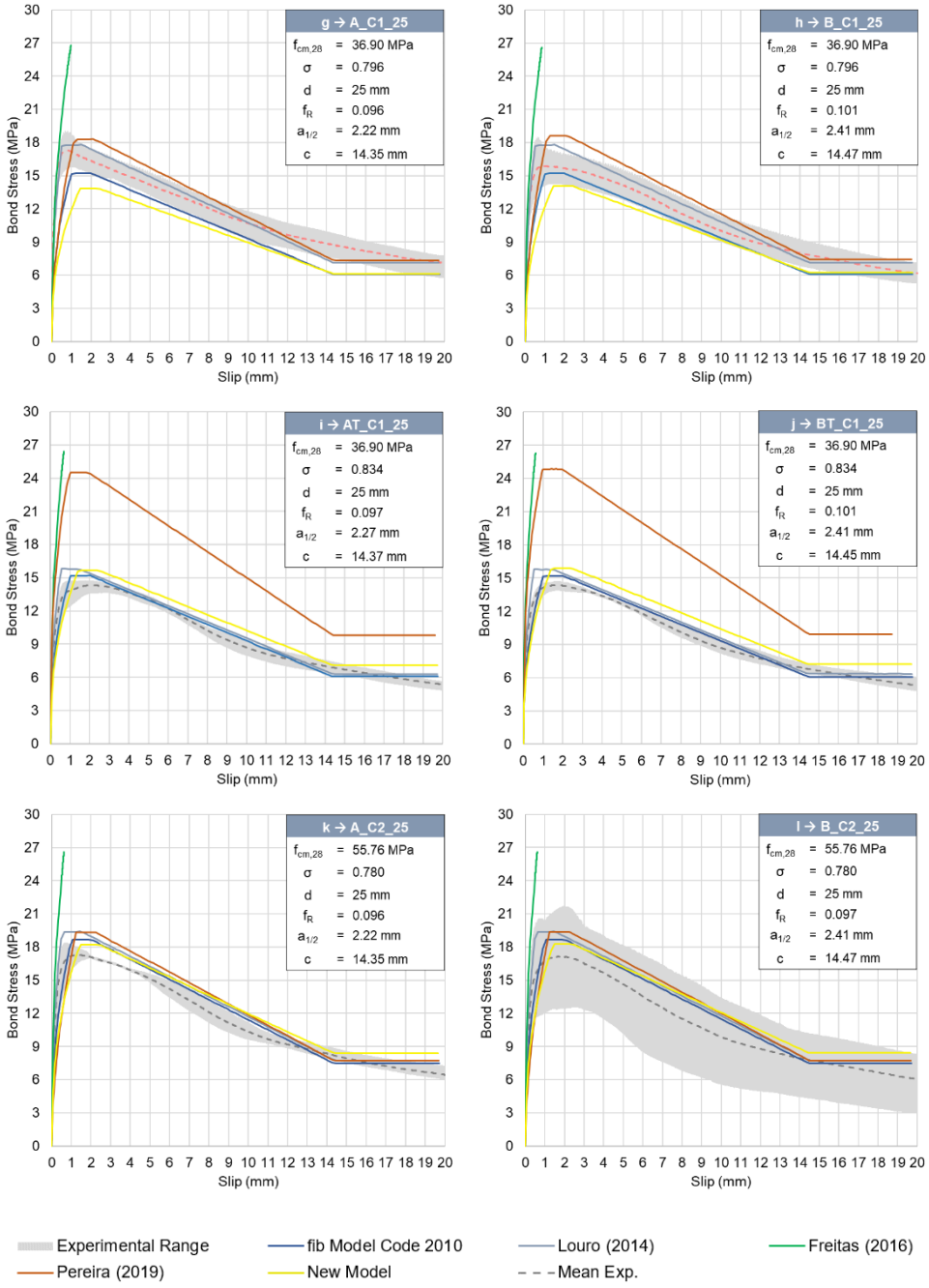


Figure 48 – Comparison of bond stress-slip curve results for the OC test series of Louro (2014) with d=25 mm.

In opposition to the previous cases of LBC and LCRAC, for the local bond behaviour on OC, the models from fib Model Code 2010 and Louro (2014) no longer provide consistently conservative results, being normally much closer to the experimental mean bond stress-slip curve. For the specific cases of series with 25 mm diameter bars (see Figure 48 g), h), i), j), k) and l)), the predictions given by these two models are on the non-conservative side by standing above the mean curve. This inability to present conservative results can be associated with the lack of consideration for the influence that a higher diameter bar has on lowering the local bond strength.

Concerning the remaining models, there is a real struggle to provide accurate predictions for the local bond behaviour of OC, with numerical results being non-conservative and sporadically wildly overestimating the bond strength. A special mention should be made to the model from Freitas (2016), which, upon observation of the numerical results for the series tested by Louro (2014), proves to be unreliable in predicting the bond behaviour of OC. The inability of this model to predict low bond stresses is patent here (see Figure 48 b) and d), and Figure 48 g), h), i), j), k) and l), where the predicted bond strength is so high that the numerical results present a tensile steel failure, due to the bar being so well bonded to the surrounding concrete that it is pulled out from the test piece, which was never the case, as shown by the experimental data. Looking specifically at the new calibrated model, the difficulty in obtaining good predictions for the local bond of OC might be connected with the fact that the majority of the pull-out specimens tested with this concrete type are the ones with the modified shape to allow the inclusion of the transversal reinforcement for added confinement. Through the introduction of these modified specimens into the overall data set, while disregarding the differences in passive confinement that are obviously associated with a larger concrete cover plus the transverse reinforcement, contributes to a higher number of variables that are not addressed in the calibration process, making it more complicated to for the model to have an appropriate response. The fact that some of the series performed by Louro (2014) are only comprised of three test specimens instead of the usual five or six (Figure 48 a), b), c), d), e) and f), and Figure 48 i), j) and k) also introduces an added level of difficulty to have a robust data sample to perform the calibration for the OC type. As a solution, a more extensive data set of bond testing on OC and using Standard specimens would, in the author's own opinion, be quite helpful in improving the calibration of the model to respond to the various types of concrete.

In terms of initial bond stiffness, the models generally offer a good and conservative response that is easiest to observe when bond strength predictions are more accurate (see Figure 46 a) and c), Figure 48 c), e) and f), and Figure 48 g), h), k) and l). It should also be noted that the experimental results seem to suggest that as the rib spacing increases, so does the length of the resistance plateau, with the descending branch slope becoming smoother than for low values of $c$. However this change might also be associated with the bar diameter size since, concomitantly, the spacing between ribs tends to increase together with the diameter. Nevertheless, regardless of its cause, this effect makes it easier for the bond prediction models to present conservative results in the post-peak stage of the local bond stress-slip curve.

## 5.3 Discussion of the beam models' results

The numerical beam models were created to extrapolate the successful modelling of the local bond behaviour into a scenario of a conceptual structural member, where the embedded length of the reinforcement is no longer short. The second intention behind the creation of the beam models was to study the influence that different local bond strength levels have on the anchorage/lap-splice length of the reinforcement. This exercise is of special relevance since it could provide information regarding the use of different concrete types as well as of bars with different characteristics and their impact on the structural behaviour, where development lengths are concerned.

Consequently, the analysis was performed using either the fib Model Code 2010 bond model or the calibrated model proposal to simulate the bond behaviour. Additionally, the analysis was based on a set of reference values for the studied bond-related parameters, which would then be varied in order to study their influence on the development length of the bars. The reference set of parameters was intended to match the characteristics of an LBC with medium compressive strength. Additionally, the reinforcing bars used always maintain a diameter of 16 mm, which is the middle ground from the experimental range of diameters that comprised the data set used to calibrate the proposed bond model. From this reference set of parameters, variations were then introduced to take into account the maximum values of the studied range of each bond-related parameter to provide some sense of how influential these can be to the variation in the development length of the reinforcement. In total, six different bond strength levels were analysed, which are identified in Table 23.

Table 23 – Variations of the bond model used in the SAB and LSB models.

| *Bond model* | *Parameters* | $f_{cm}$ *(MPa)* | $f_R$ | $\sigma$ | *d (mm)* | $RA_{<c}$ | $RA_{\geq c}$ | $\tau_{bmax}$ *(MPa)* |
|---|---|---|---|---|---|---|---|---|
| *fib MC2010* | Reference | 33 | 0.058 | 0.82 | 16 | 0.00 | 0.00 | 14.36 |
| *New model* | Reference | | 0.058 | 0.82 | | 0.00 | 0.00 | **15.87** |
| | Variation 1 | | 0.058 | 0.82 | | **0.34** | 0.00 | 11.16 |
| | Variation 2 | | **0.101** | 0.82 | | 0.00 | 0.00 | 18.68 |
| | Variation 3 | | 0.058 | 0.82 | | 0.00 | **0.46** | 19.22 |
| | Variation 4 | | 0.058 | **0.86** | | 0.00 | 0.00 | 22.48 |

For each variation introduced in the bond function assigned to the bars of the beam model, an iterative exercise was performed in order to assess the development length necessary for the beam to avoid failure due to insufficient bond resistance. Thus, this exercise consisted in running several analyses for each set of parameters, where the length of the bars would vary 5 mm at a time. During the analysis, the axial stress in the bars was monitored, as well as the bond stress-slip response at the end of the reinforcement. The anchorage length for a given bond level would then be assessed by registering at which bar length the yielding of the steel would occur previously to the maximum bond stress at the end of the bars being reached. The results of this process were documented and will be discussed in the following sections.

### 5.3.1 Results of the straight anchorage beam model

The SAB model presented good results regarding the bond performance of the reinforcement since by varying the anchorage length of the bars, it suffered little effect over its overall performance under flexure but developed significant differences in the anchorage zones. Furthermore, monitoring the bond stress-slip relationship at the end of the anchorage zone proved successful since it enabled the evaluation of the bond failure occurring in the reinforcement. Finally, the case study that employed the fib Model Code 2010 bond model will be presented to exemplify the model's overall structural behaviour.

The SAB model presented an adequate load-deflection response, as shown in Figure 49. The first flexural cracks start to appear around a load level of about 8 kN, introducing a significant loss of stiffness to the element. The yielding of the reinforcement occurs later, at approximately a load level of 42 kN,

introducing another significant loss of stiffness to the beam. Figure 50 presents the evolution of the cracking pattern as the load level increases, with flexural cracking continuously propagating from the mid-span to the supports and minimal cracks occurring due to transverse loading, as expected as a result of the level of transverse reinforcement.

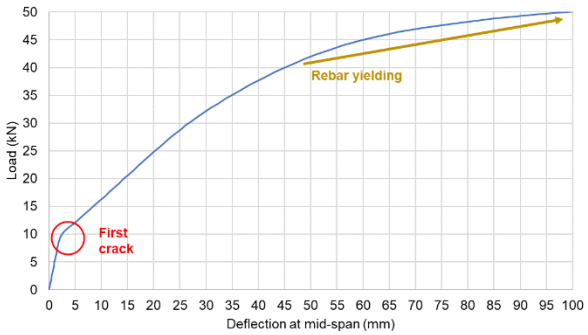


Figure 49 – SAB model: load vs deflection at mid-span, with the fib Model Code 2010 bond model.

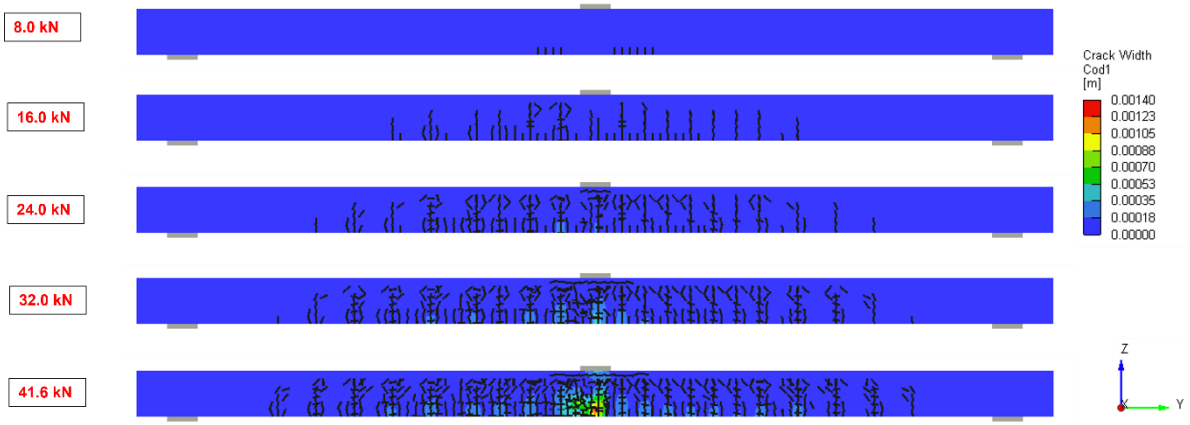


Figure 50 – SAB model: evolution of the crack pattern.

Figure 51 shows the development of the axial and bond stresses during the analysis, and at first glance, it is possible to observe how different is the bond behaviour along the bar compared to the local bond behaviour observed in the pull-out model. Conversely to the local bond behaviour, where an average bond stress is attained, in a bar with a long embedded length, as the load level increases, results show that the bond stress reaches a low limit value (around 4.9 MPa in this case), which oscillates in signal along the bar length. Additionally, at the anchorage zone, bond stress increases until the connection's bond strength is achieved. Concerning the evolution of the axial stress, it is possible to see the progressive increase where the flexure moment is expected to be the highest (i.e. at the mid-span) with a sharp decrease occurring in the anchorage end due to the high bond stresses and slip that develop in this region. From these graphical observations, it is possible to ascertain that although high bond stresses are needed to avoid failure, the proper transfer of stresses that enables the main load-carrying mechanism of the beam only requires a low level of bond resistance, which once again, is not constant throughout the bar.

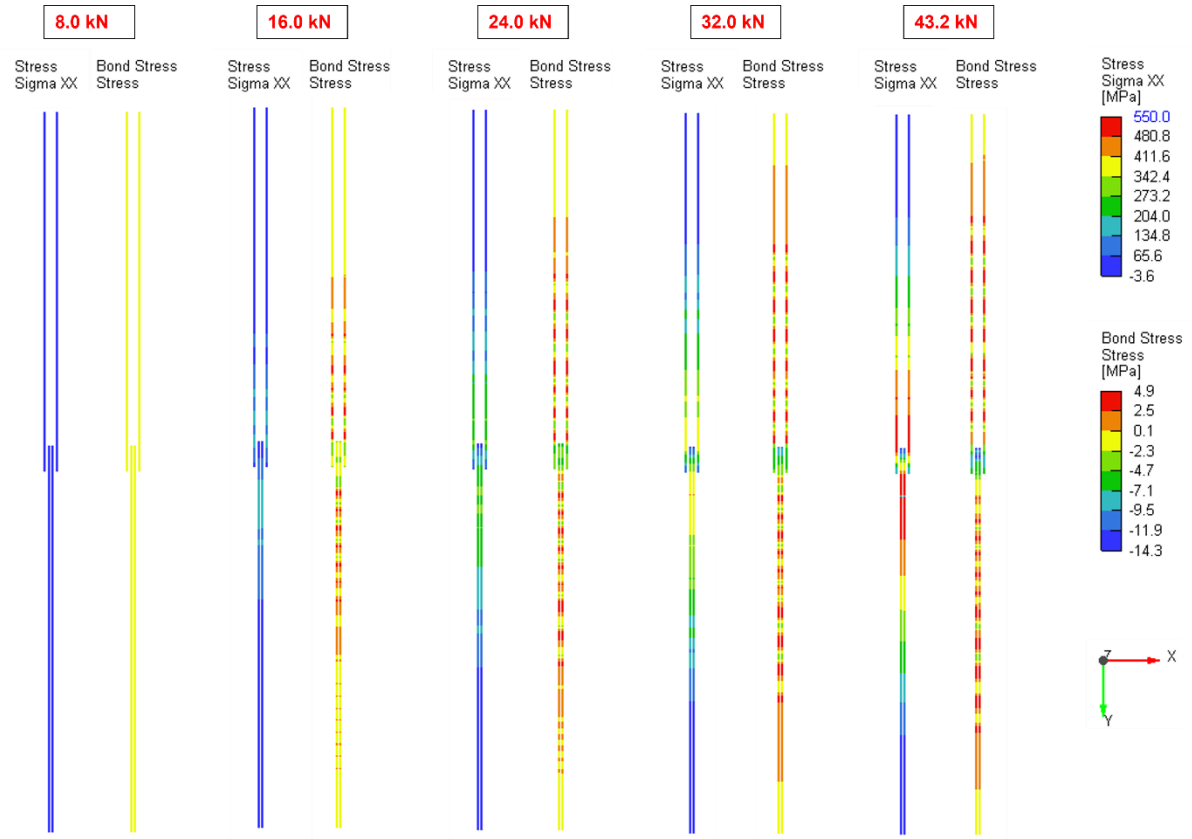


Figure 51 – SAB model: evolution of the axial (Sigma XX) and the bond stresses during the analysis

In Figure 52, it is possible to observe the monitored bond-stress slip relationship at the extremity of the straight anchorage zone. The shape of the bond-stress slip curve resembles the one observed for the pull-out tests, thus confirming that in this type of structural member with conventional concrete cover and distance between bars, confinement levels are sufficient to ensure a ductile failure by pull-out, hence avoiding the undesirable splitting failure.

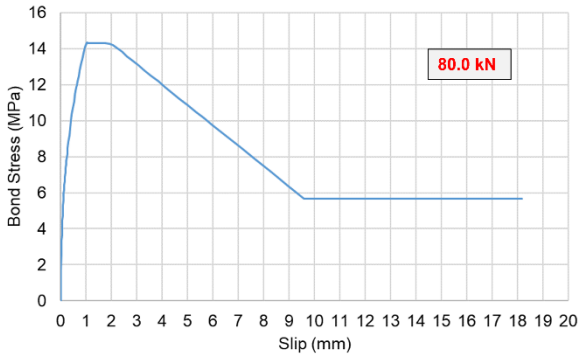


Figure 52 – SAB model: bond stress-slip response at the end of the straight anchorage using the fib Model Code 2010 bond model.

The following approach was taken to investigate the needed anchorage length to discuss the influence of the variation in parameters applied to the SAB model. For a given set of parameters, the analysis was run with a specific bar length, and the analysis's steps at which the steel yielding and pull-out failure occurred were registered. If the pull-out failure occurred prior to steel yielding, the length of the bar would be increased by 5 mm, and the analysis would be repeated. Once the yielding preceded the bond

failure, the value of the anchorage length for that analysis would be deemed appropriate, and the search would be concluded for that given set of parameters. The consequential results of this process are presented in Table 24 and Figure 53 illustrates the evolution of the necessary anchorage length according to the bond strength level employed.

Table 24 – SAB model: anchorage length results according to the bond strength level.

| *Bond model* | *Parameters* | ⇔ | $\tau_{bmax}$ *(MPa)* | $\Delta\ \tau_{bmax}$ *(%)* | *Anchorage length (mm)* | $\Delta\ l_b$ *(%)* |
|---|---|---|---|---|---|---|
| *fib MC2010* | Reference | - | 14.36 | 0% | 225 | 0% |
| *New model* | Reference | - | 15.87 | 11% | 200 | -11% |
| | Variation 1 | $RA_{<c}$=0 → 0.34 | 11.16 | -22% | 280 | 24% |
| | Variation 2 | $f_R$=0.580 → 0.101 | 18.68 | 30% | 150 | -33% |
| | Variation 3 | $RA_{\geq c}$ =0 → 0.46 | 19.22 | 34% | 150 | -33% |
| | Variation 4 | σ=0.82 → 0.86 | 22.48 | 57% | 145 | -36% |

* Δ refers to variation relative to the fib Model Code 2010 bond model's results

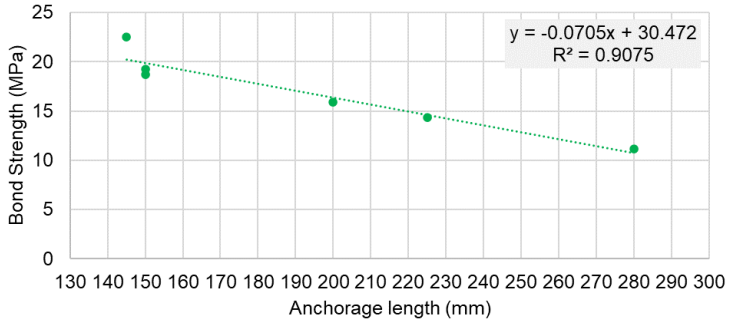


Figure 53 – SAB model: bond strength versus anchorage length.

Concerning the reference set of parameters, a first observation can be made that the use of the new bond model requires less steel than the one from fib Model Code 2010. The difference in anchorage length between the two models was 25 mm, accounting for an 11% variation in anchorage length, coincidentally the same as the variation in bond strength between the models. Comparison between these cases is useful since it provides an example of the differences in material usage obtained from using a rather conservative bond model or a more precise model; however, the number of results obtained is very limited, and so any conclusion that is reached should consider this factor (i.e. a much larger number of data would be necessary to affirm with certainty how much is the impact of using different bond models). Secondly, observing parameter variation 1, which concerns the use of 34% of $RA_{<c}$, it is very clear that the loss in bond strength is very negative to the anchorage requirements: a difference of 80 mm and the anchorage length varying once again linearly with the bond stress. Thirdly, it was interesting to observe that parameter variation 3 (regarding 46% of $RA_{\geq c}$) seems to be as much beneficial as the use of ribbed bars with a high bond index (parameter variation 2); this is, both registered the same anchorage length given their similar bond strength levels. However, as mentioned previously, results regarding the prediction of bond strength in LCRAC should be taken with some caution.

The best results were present when using an LBC with a high packing density (parameter variation 4), which provided the shortest anchorage length. Nonetheless, it should be noted that contrary to the

registered tendency of previous parameter variations, where the reduction in anchorage length seems to vary linearly with the bond strength, the present case presented only a 36% reduction in bar length when bond strength increased 57% (comparatively to the fib Model Code 2010 bond model).

### 5.3.2 Results of the lap-splice beam model

The LSB model captured good results regarding the bond performance of the reinforcement since by varying the lap-splice length of the bars, the beam suffered little effect over its overall performance under flexure but performed with significant differences in the lap-splice zone. Furthermore, monitoring the bond stress-slip relationship at the extremity of the inner and external reinforcing bars proved successful since it enabled the evaluation of the bond failure that occurred in the reinforcement. However, the LSB model produced less stable results than the SAB model, with the convergence errors registered in the numerical analysis rising above the recommended threshold of 10% when the loading levels were high. This factor affected the obtained bond stress-slip curves, which frequently presented awkward fluctuation in bond strength at the bond strength plateau range. The case study that employed the fib Model Code 2010 bond model will be presented to exemplify the model's overall structural behaviour.

The LSB model presented an adequate load-deflection response, as shown in Figure 54. The first flexural cracks start to appear around the 6 kN load level, introducing a significant loss of stiffness to the element. The yielding of the reinforcement occurs later and around 30 kN, introducing another significant stiffness loss in the beam. Figure 55 presents the development of the cracking pattern as the load level increases, with flexural cracking continuously spreading from the mid-span to the supports and minimal cracks occurring due to transverse loading. It should be noted that the load level represented in the following figures is relative to each point load since both applied loads always have equal value throughout the analysis (for example, the yielding occurs when at each loading plate is applied 30 kN).

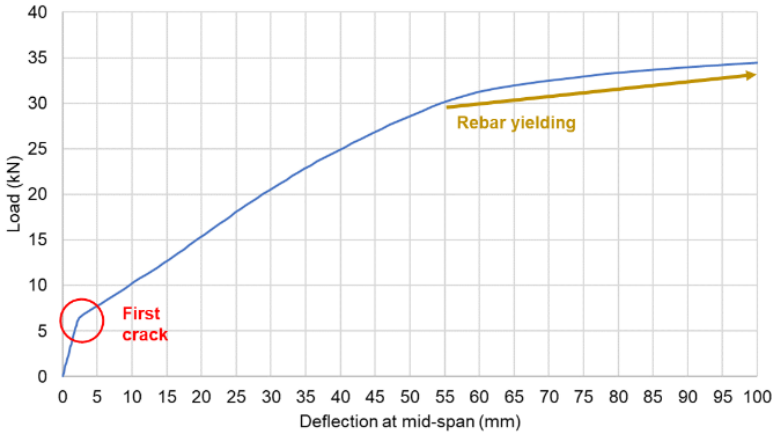


Figure 54 – LSB model: load vs deflection at mid-span with the fib Model Code 2010 bond model.

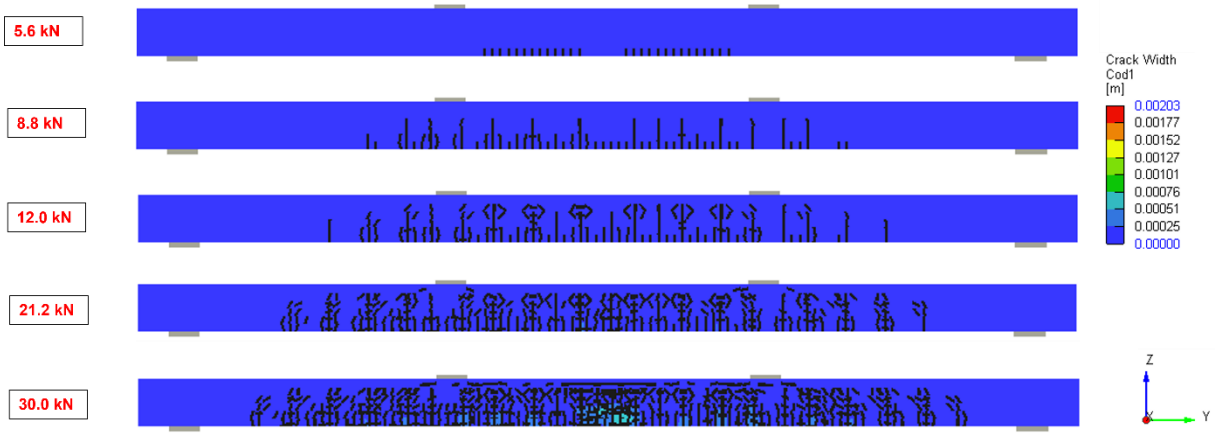


Figure 55 – LSB model: evolution of the crack pattern.

Figure 56 shows the evolution of the axial stress and the bond stress during the analysis. The overall results are very similar to those of the SAB model, despite the differences in anchorage type. As the loading increases, the bond stress reaches a low limit value (around 4.6 MPa, in this case) which oscillates in signal along the length of the bar until it reaches the zone of the lap-splice, where bond stress values fulfil the bond strength capacity.

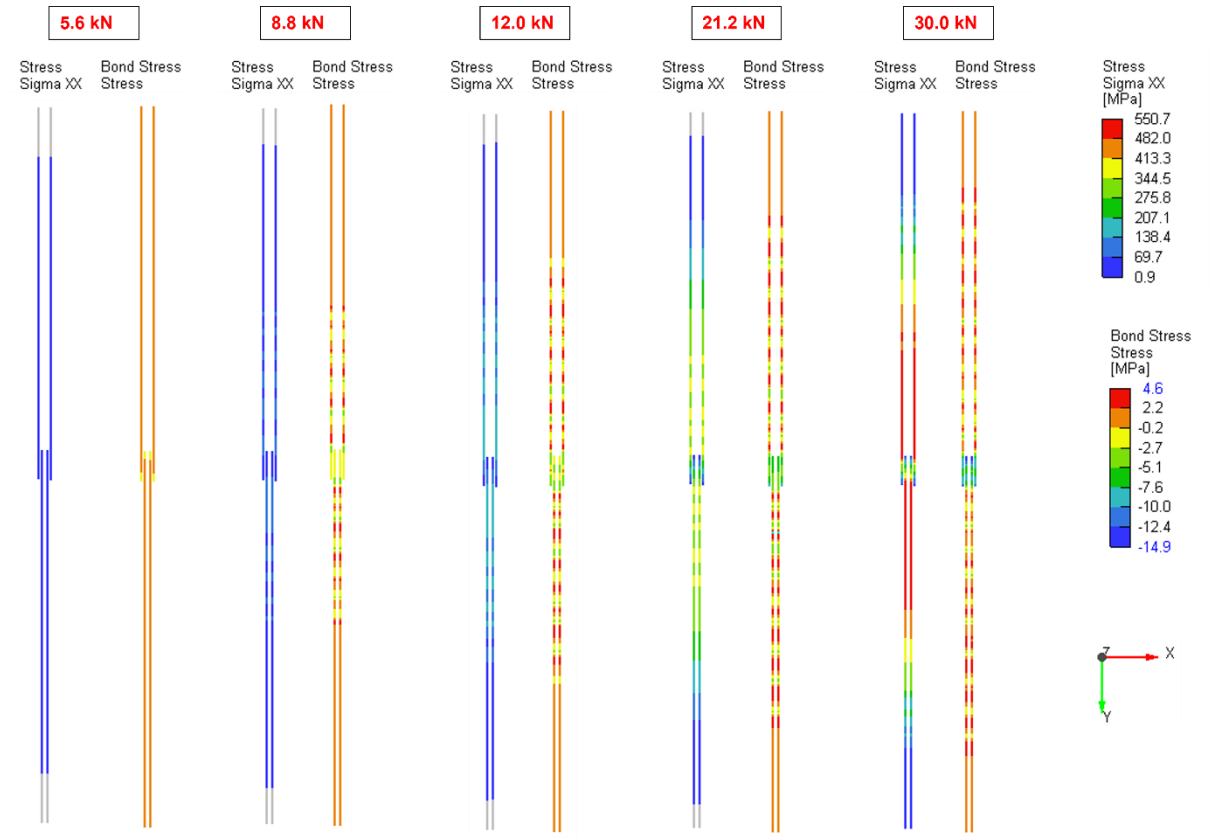


Figure 56 – LSB model: evolution of the axial (Sigma XX) and the bond stresses during the analysis.

Figure 57 presents the monitored bond stress-slip curves for the inner and external reinforcing bars at the end of the analysis (load level of 40 kN). Again, some oscillation can be observed in the bond strength plateau, although the ascending branch of the curve seemed not to have been affected. In terms of bond failure, as was the case for the SAB model, it was possible to observe the ductile pull-out

failure in both bars of the lap-splice anchorage. A common occurrence throughout the LSB model, regardless of the set of parameters employed for varying the bond function, was that the bond of the inner reinforcing bar tended to fail much sooner than the external bar. This fact might be linked with the inner bar possibly having lower confinement than the external bar, given the proximity to the other reinforcing bars present inside the beam (the cover distance of the external bar may provide better confinement). The earlier occurrence of the pull-out failure in the inner bar is reflected in the slip values reached by both bars at the end of the analysis (i.e. the inner bar surpasses the 4 mm mark, whereas the external bar stays closer to the 3 mm slip value).

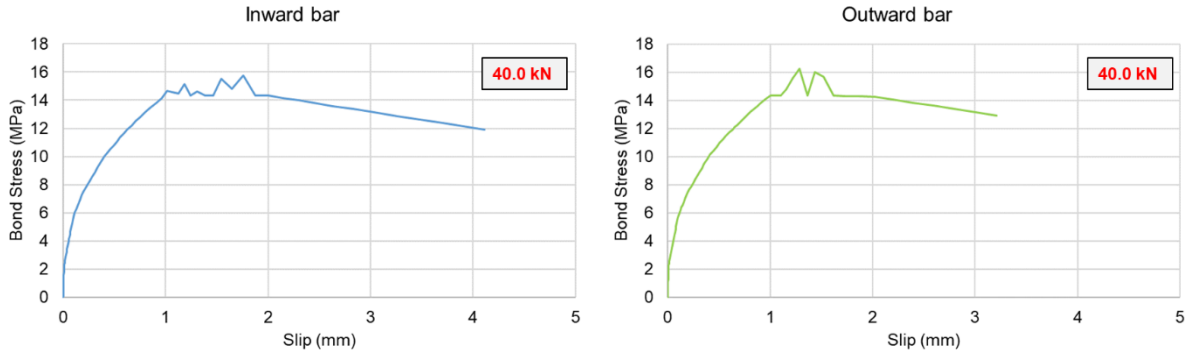


Figure 57 – LSB model: bond stress-slip response at the end of the lap splice anchorage using the fib Model Code 2010 bond model.

The evaluation of the lap-splice length followed a similar process as the one used for the SAB model's anchorage length, with changes in length affecting both the inner and external bars. The consequential results of the lap-splice length evaluation process are presented in Table 25. Figure 58 depicts the evolution of the lap-splice length according to the bond strength level.

Table 25 – LSB model: lap-splice length results according to the bond strength level.

| *Bond model* | *Parameters* | ⇔ | $\tau_{bmax}$ *(MPa)* | $\Delta\ \tau_{bmax}$ *(%)* | *Lap-splice length (mm)* | $\Delta\ l_b$ *(%)* |
|---|---|---|---|---|---|---|
| *fib MC2010* | Reference | - | 14.36 | 0% | 250.0 | 0% |
| *New model* | Reference | - | 15.87 | 11% | 230.0 | -8% |
| | Variation 1 | $RA_{<c}=0 \rightarrow 0.34$ | 11.16 | -22% | 270.0 | 8% |
| | Variation 2 | $f_R=0.580 \rightarrow 0.101$ | 18.68 | 30% | 220.0 | -12% |
| | Variation 3 | $RA_{\geq c}=0 \rightarrow 0.46$ | 19.22 | 34% | 220.0 | -12% |
| | Variation 4 | $\sigma=0.82 \rightarrow 0.86$ | 22.48 | 57% | 180.0 | -28% |

** Δ refers to variation relative to the fib Model Code 2010 bond model's results*

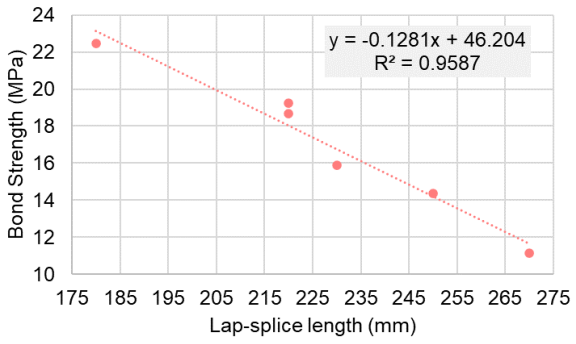


Figure 58 – LSB model: bond strength vs lap-splice length.

As was observed for the anchorage length in the SAB model, the lap-splice length seems to vary linearly with the bond strength level of the reinforcement. The linear regression line for these results has a higher goodness-of-fit value than the previous ones ($R^2$=0.9587 versus 0.9075), which is undoubtedly due to the parameter variation 4 not disrupting the tendency established by the previous variation, as was the case in the SAB model. However, this relationship shows some differences from the one observed previously, with variation in bond strength leading to smaller changes in bar length. This fact is quite noticeable in the parameter variations 2 and 3, where a difference of around 30% in bond strength (comparatively to the fib Model Code 2010 bond model) equated to less than half of that value in the lap-splice length variation.

### 5.3.3 Summary remarks

On the surface level, the results of the exercise performed in both the beam models are, in fact, quite straightforward, given the linear relationships that were revealed between the bond strength and the anchorage/lap-splice length; however, some important considerations can be extracted from this small set of results.

Based on these results, a case can be made for the importance that a more thorough evaluation of the bond behaviour of reinforcement in anchorage zones can have on the sustainability of the construction industry because of the important material savings that can be obtained by taking into consideration the various factors that affect the bond performance. For example, the savings obtained using the new bond model instead of the more conservative one from fib Model Code 2010 were 25 and 20 mm for the SAB and LSB models, respectively. Furthermore, when comparing the worst and best-case scenarios (i.e. an LBC with RA<c=0.34% versus an LBC with σ=0.86), the differences in bar length are even more noticeable, them being 135 and 90 mm for the SAB and LSB models, respectively. Although, at first glance, it could be argued that these savings are almost insignificant in the context of a single structural member when extrapolated to the context of a full structure, the sum of all these small values can have a big impact on the construction cost and ecological footprint. A case could also be made that the new calibrated bond model used still is not sufficiently accurate to provide the desired results; however, this argument does not change the fact that the model from fib Model Code 2010 is very conservative when it comes to the prediction of the bond behaviour of LBC and LCRAC, and that both these types of concrete, when properly conceived, have shown to be able to improve the bond performance considerably.

As a last note, it should be safeguarded that the number of results obtained from performing this exercise is very limited, and any certainty to the conclusions drawn would require a much bigger data sample to be obtained. However, this exercise is useful as an indicator that the bond performance at the anchorage/lap-splice zones can be important and that it would be useful to perform a further investigation on this subject.

# 6. Conclusions and future work

## 6.1 Conclusions

The main outcome of the present dissertation was the calibration of a new bond model for OC/LBC/LCRAC. This new bond model focused on including the influence of a broad range of bond-related parameters, already established in the literature as capable of affecting the bond performance but not yet properly quantified in conjunction with other bond parameters. The new model and adopted coefficients are presented in Table 26.

Table 26 – New calibrated local bond stress-slip model. (Same as Table 12).

| | |
|---|---|
| $\tau_{bmax}$ [MPa] | $2.5 \cdot \sqrt{f_{cm}} \cdot \varphi_{f_R} \cdot \varphi_{\sigma} \cdot \varphi_{d} \cdot \varphi_{RA_{\geq c}} \cdot \varphi_{RA_{<c}}$ |
| $\varphi_{f_R}$ | $4.757 \cdot f_R + 0.8785$ |
| $\varphi_{\sigma}$ | $117.17 \cdot \sigma^2 - 188.24 \cdot \sigma + 76.397$ |
| $\varphi_{d}$ | $-0.0292 \cdot d + 1.4634$ |
| $\varphi_{RA_{\geq c}}$ | $-2.2446 \cdot RA_{\geq c}^2 + 1.4731 \cdot RA_{\geq c} + 0.9579$ |
| $\varphi_{RA_{<c}}$ | $4.038 \cdot RA_{<c}^2 - 2.4333 \cdot RA_{<c} + 1.2152$ |
| $s_1$ [mm] | $0.05 \cdot d + 0.15$ |
| $s_2$ [mm] | $0.05 \cdot d + 1.15$ |
| $s_3$ [mm] | $c$ |
| $\alpha$ | $0.4$ |
| $\tau_{bf}$ [MPa] | $0.5164 \cdot \tau_{bmax} - 1.017, \quad for\ OC$ |
| | $0.3826 \cdot \tau_{bmax} - 0.9094, \quad for\ LBC/LCRAC$ |

Where, $\tau_{bmax}$ is the bond strength, $\varphi$ is the coefficient for the influence of the identified bond-related parameter, $s_1$ and $s_2$ are the limit slip values of the bond strength plateau, $s_3$ is the slip value for the beginning of the bond's residual capacity, $\alpha$ is the coefficient that characterizes the $\tau_b - s$ relationship of the ascending branch and $\tau_{bf}$ is the residual bond stress due to bond friction.

The refinement of the coefficient regarding the influence of the bond index proved to be unsuccessful, and as such, the coefficient used in the model of Pereira (2019) was adopted in the new model. The various attempts performed to calibrate the coefficient revealed a negative influence of $f_R$ over the bond behaviour, which goes against what has already been extensively documented in the literature. The reasons behind the failure to calibrate could be linked to the inability of the method used to isolate the influence of $f_R$. The coefficient from the model of Pereira (2019) is a linear equation with a positive slope, thus depicting the positive influence of the increase of $f_R$ over the bond behaviour.

The packing density's influence on the bond strength was greater when the parameter's value was at the top end of the studied range (between 0.82 and 0.86) and less significant when in the lower range (between 0.78 and 0.82). The influence of $\sigma$ was thus captured by a second-degree polynomial equation,

with an inflexion point at approximately $\sigma = 0.80$. In practice, the obtained results mean that whilst when the packing density is lower, as is the case for OC, the impact is almost insignificant, when packing density is higher, as occurs for LBC and LCRAC, the improvements over the bond behaviour are significant. This conclusion is new information that adds to the previous knowledge that the increase of $\sigma$ was positive to the bond performance.

The inclusion of a coefficient regarding the bar diameter had the novelty of including, in conjunction with other bond-related parameters, the influence of the size effect. The coefficient consists of a linear equation with a negative slope which depicts the negative influence of the increasing diameter over the bond performance, a fact that already had been extensively documented in the literature. Furthermore, not only did the bar diameter exhibit an influence over the bond strength but also over the bond stiffness, with the hallmark slip values of the bond strength plateau exhibiting a clear correlation with the bar size. Larger sized bars showed a negative effect on the bond stiffness. In previous works, bond stiffness was correlated with other parameters such as the bond index and the packing density; however, after careful analysis of the data, the results concluded that the diameter was the main responsible for the variation in the slip values.

The influence of the RA content was evaluated according to the aggregate size, whether it is bigger or smaller than the rib spacing of the reinforcement. Pereira (2019) had already shown the negative influence of increasing $RA_{<c}$; however, the new calibrated model included a coefficient for the influence of $RA_{\geq c}$ to better predict the bond strength of LCRAC. Both coefficients consist of second-degree equations with opposite inflexions to one another. In practice, $RA_{<c}$ presents a negative effect over bond in the studied range (between 0 and 0.34), whereas $RA_{\geq c}$ is mainly beneficial to bond in the studied range (between 0 and 0.46), with the inflexion point located at approximately $RA_{\geq c} = 0.33$. The caveat of the calibration of both these coefficients is the fact that the data pool of LCRAC was very limited and would benefit from further calibration if more POT results were available.

Concerning the residual bond capacity, the type of concrete revealed a clear influence over the bond stress at this stage. In fact, this tendency had already been identified by Pereira (2019), and the new model only calibrated the $\tau_{bf}$ parameter to better predict the results of the current data pool.

Regarding the remaining parameters $s_3$ and $\alpha$, as no clear relationship was established between them and any of the addressed bond-related parameters, their values remained the same as the ones defined in the fib Model Code 2010 model.

About the FE modelling of the local bond behaviour, four reference POT models were successfully built to replicate the specimens of the experimental campaigns of Louro (2014), Freitas (2016) and Pereira (2019) since the bond behaviour registered by the reinforcement was consistent with the literature, and the crack pattern observed was compatible with a failure by pull-out (or splitting in certain cases). The FE modelling of the bond behaviour was performed through a phenomenological approach, meaning that bond is accounted for as a bond stress-slip function assigned to a discrete reinforcement element; however, this approach was revealed not to be appropriate to calibrate the bond stress-slip model since the bond behaviour is defined by the function and is not influenced by the material properties of the

remaining elements of the model. As such, in order to perform the calibration of the bond model through the use of numerical methods, the detailed modelling approach is recommended, where reinforcement is modelled as 3D or 2D element with the appropriate rib configuration instead of a discrete element with an assigned bond function.

The main difficulty in the models' construction was in the mesh refinement, which was found to have a strong influence on the pull-out load applied to the model and, indirectly the resulting crack pattern observed in the concrete. The mesh refinement was set in a way such that the difference between the monitored pull-out force converted to bond stress and the bond stress monitored in the free-end of the reinforcement was approximately equal to 10%. Meshes with too many elements resulted in unrealistic crack patterns despite there being no clear reason for the model to behave in such a manner. It is the conviction of the author that some of the problems found in the modelling of the POT models might be related to the use of the ATENA 3D user interface, and it would be advisable the use of the GiD user interface in future attempts.

The comparison between the numerical and experimental results enabled the evaluation of the various bond models. Overall, the calibrated bond model was able to provide more accurate results than the pre-existing models, with its mean deviation to accuracy error being 0% compared to 39.20, 31.48, -17.20 and -1.48% for the models of fib Model Code 2010, Louro (2014), Freitas (2016) and Pereira (2019), respectively. Although the mean error of the calibrated model is very similar to that of the model from Pereira (2019), the new model was able to reduce the difference between the maximum positive and negative error (47.50% compared to 73.13%) and also provides more accurate results, despite all the mentioned shortcomings and the occasional non-conservative prediction.

Nonetheless, the successful modelling of the POT enabled then the modelling of the local bond behaviour to be extrapolated to two different beam models. These beam models permitted the evaluation of anchorage and lap-splice lengths by using the local bond stress-slip model to prescribe the bond behaviour to the reinforcement. Furthermore, the results from the beam models showed that by considering the different bond resistance capacity that comes with the use of different concrete types and reinforcing bars, the length of reinforcement needed in the anchorage/lap-splice zones is affected. Both models exhibited a positive linear relationship between the bond strength variation and the anchorage/lap-splice length variation. Thus, the use of properly conceived ecological concrete mixtures such as LBC and LCRAC are shown in this exercise to have an ability to improve the sustainability of the construction industry but also to improve the structural performance where bond performance is concerned. However, it should be safeguarded that the restricted number of obtained results lend to this exercise a mere exploratory nature, and a bigger data pool would be required for the drawn conclusions to be more certain and trustworthy.

## 6.2 Future work

In the future, the empirical calibration of the bond stress-slip model would greatly benefit from a larger data sample of pull-out tests conducted in specimens involving LCRAC. The 15 POT performed on

LCRAC comprised only 11% of the total data pool, which is bound to have a negative effect on the potential of the calibrated bond model to accurately predict the bond behaviour in this concrete type. Additionally, given the non-conservative predictions that the new model had for the POT performed in OC, the author's opinion is that a new calibration with a bigger data pool of POT performed in OC under standard conditions would be beneficial. Unfortunately, the fact that it was not possible to account for the different confinement levels of the modified POT of Louro (2014) compared to the standard POT of Freitas (2016) and Pereira (2019) means that this variable was not accounted for in the calibration and is certain to have had negatively impacted the results. Despite the studied literature featuring various experimental POT campaigns, these often focused on a limited number of bond-related parameters, which was an obstacle to the obtention of data to perform a global study of bond behaviour, such as was the case of the present work

Alternatively, calibration of a new bond model for LBC/LCRAC could be attempted through FE modelling (as was firstly intended in this dissertation); however, this should be performed by following a detailed modelling approach instead of a phenomenological one. Using a detailed approach means that the reinforcing bar should be modelled as a 3D or 2D element, taking into account the characteristics of the transversal ribs. Also, the impact that the confinement level, RA content, and packing density have on the concrete behaviour should be carefully evaluated in order to obtain appropriate results since this modelling approach evaluates the bond behaviour based on the interaction between the concrete elements that interface with the modelled ribs of the reinforcement.

Another future work could be linked with the study of the LBC/LCRAC bond under cyclic loading. Louro (2014) studied the bond behaviour under cyclic loading of pull-out specimens involving OC, and a similar study involving the new ecological concrete types could be very relevant in the future. Moreover, in 2014 Louro attempted the FE modelling of the local bond behaviour under cyclic loading, although limitations of the software used at the time impeded the results of the experience from being successful. With the advancement of technology through the years, it would be relevant to attempt to model the bond behaviour under this type of loading once again.

Regarding the overall study of bond behaviour, many parameters are still left to be incorporated into the bond model. Some parameters have already been referred to previously, such as the confinement, the loading rate, and different packing optimisation curves, but many others remain. For example, concerning the concrete material, what influence can high temperatures or the freeze-thaw effect have on bond performance. On the side of the reinforcement properties, factors such as rebar coating, corrosion, and different rebar materials can also be incorporated. This is not to say that these factors have not been addressed in the literature, which they have; however, attempting their inclusion in a parameter broad bond model could be beneficial to furthering the knowledge on the subject.

With regards to the modelling structures utilizing the local bond model to reproduce the bond behaviour of the reinforcing bars with long embedded lengths, a broader parametric study, similar to the exercise performed in the present work for the two beam models, would be very beneficial to evaluate with greater certainty the impact that the difference in bond strength levels has on the anchorage/lap-splice zones.

# Bibliography


ACI Committee 408. (2003). 'ACI 408R-03 Bond and Development of Straight Reinforcing Bars in Tension'. *American Concrete Institute*, 1–49.

Alavi-Fard, M., and Marzouk, H. (2004). 'Bond of high-strength concrete under monotonic pull-out loading'. *Magazine of Concrete Research*, 56(9), 545–557.

Arel, H. Ş., and Yazici, Ş. (2012). 'Concrete-reinforcement bond in different concrete classes'. *Construction and Building Materials*, 36, 78–83.

Azizinamini, A., Chisala, M., and Ghosh, S. K. (1995). 'Tension development length of reinforcing bars embedded in high-strength concrete'. *Engineering Structures*, 17(7), 512–522.

Bamonte, P. F., and Gambarova, P. G. (2007). 'High-bond bars in NSC and HPC: Study on size effect and on the local bond stress-slip law'. *Journal of Structural Engineering*, 133(2), 225–234.

Breccolotti, M., and Materazzi, A. L. (2013). 'Structural reliability of bonding between steel rebars and recycled aggregate concrete'. *Construction and Building Materials*, Elsevier Ltd, 47, 927–934.

Butler, L., West, J. S., and Tighe, S. L. (2011). 'The effect of recycled concrete aggregate properties on the bond strength between RCA concrete and steel reinforcement'. *Cement and Concrete Research*, Elsevier Ltd, 41(10), 1037–1049.

Červenka, V., Jendele, L., and Červenka, J. (2012). 'ATENA Program Documentation Part 1 Theory'. *Atena*, 1–282.

Chiriatti, L., Hafid, H., Mercado-Mendoza, H. R., Apedo, K. L., Fond, C., and Feugeas, F. (2018). 'Influence of Recycled Concrete Aggregate Content on the Rebar/Concrete Bond Properties through Pull-Out Tests and Acoustic Emission Measurements'. *International Journal of Civil, Environmental, Structural, Construction and Architectural Engineering*, 12(3).

Costa, A., and Appleton, J. (2002). 'Lecture notes for Reinforced and Prestressed concrete structures, Parte II - Materials'. *Instituto Superior Técnico, Lisbon.*

Darwin, D., and Graham, E. K. (1993). 'Effect of deformation height and spacing on bond strength of reinforcing bars'. *ACI Materials Journal*, 90(6), 646–657.

Darwin, D., McCabe, S. L., Idun, E. K., and Schoenekase, S. P. (1992). 'Development length criteria. Bars not confined by transverse reinforcement'. *ACI Structural Journal*, 89(6), 709–720.

Darwin, D., Tholen, M. L., Idun, E. K., and Zuo, J. (1996). 'Splice strength of high relative rib area reinforcing bars'. *ACI Structural Journal*, 93(1), 95–107.

Dong, H., Song, Y., Cao, W., Sun, W., and Zhang, J. (2019). 'Flexural bond behavior of reinforced recycled aggregate concrete'. *Construction and Building Materials*, Elsevier Ltd, 213, 514–527.

Eligehausen, R., Popov, E. P., and Bertero, V. . (1983). 'Local bond stress-slip relationships of deformed bars under generalized excitations, University of California, report no UCB/EERC-83/23 of the National Science Foundation'. *Proceedings of the 7th European Conference on Earthquake Engineering.*, 69–80.

Eligehausen, R., Popov, E. P., and Bertero, V. V. (1982). 'Local Bond Stress-Slip Relationships of Deformed Bars Under Generalized Excitations.' 4(November), 69–80.

European Aggregates Association (2022). *31st of May 2022*, https://uepg.eu/pages/facts.

European Committee for Standardization (2004). 'Eurocode 2: Design of concrete structures - Part 1-1: General rules and rules for buildings' (EN 1992-1-1).

European Committee for Standardization (2005). 'Steel for the reinforcement of concrete - Weldable reinforcing steel - General' (EN 10080:2005).

European Committee for Standardization (2007). 'Concrete Part 1: Specification, performance, production and conformity', (NP EN 206-1).

Federation internationale du beton. (2000). 'fib Bulletin No10 - Bond of reinforcement in concrete'.

Federation internationale du beton (2010). *fib Model Code for Concrete Structures 2010*. Ernst & Sohn.

Fennis, S. A. A. M. (2011). 'Design of Ecological Concrete by Particle Packing Optimization'. *Pasaia*, (January 2010), 20110.

Fennis, S. A. A. M., and Walraven, J. C. (2012). 'Using particle packing technology for sustainable concrete mixture design'. *Heron*, 57(2), 73–101.

Fernandez, I., Etxeberria, M., and Marí, A. R. (2016). 'Ultimate bond strength assessment of uncorroded and corroded reinforced recycled aggregate concretes'. *Construction and Building Materials*, Elsevier Ltd, 111, 543–555.

Flower, D. J. M., and Sanjayan, J. G. (2007). 'Green house gas emissions due to concrete manufacture'. *The International Journal of Life Cycle Assessment*, 12(5), 282–288.

Freitas, E., Louro, A. S., Costa, H., Cavaco, E. S., Júlio, E., and Pipa, M. (2020). 'Bond behaviour between steel / stainless-steel reinforcing bars and low binder concrete (LBC)'. *Engineering Structures*, Elsevier, 221(July), 111072.

Freitas, E. R. (2016). 'Bond between stainless steel bars and low binder concrete' (in Portuguese), *Master's Thesis, Instituto Superior Técnico, Lisbon*.

Hamad, B. S. (1995). 'Bond strength improvement of reinforcing bars with specially designed rib geometries'. *ACI Structural Journal*, 92(1), 3–13.

Harajli, M. H., Hamad, B. S., and Rteil, A. A. (2004). 'Effect of confinement of bond strength between steel bars and concrete'. *ACI Structural Journal*, 101(5), 595–603.

Hayles, M., Sanchez, L. F. M., and Noël, M. (2018). 'Eco-efficient low cement recycled concrete aggregate mixtures for structural applications'. *Construction and Building Materials*, Elsevier Ltd, 169, 724–732.

Ichinose, T., Kanayama, Y., Inoue, Y., and Bolander, J. E. (2004). 'Size effect on bond strength of deformed bars'. *Construction and Building Materials*, 18(7), 549–558.

International Organization for Standardization (2010). 'Steel for the reinforcement and prestressing of concrete - Test methods - Part 1: Reinforcing bars, wire rod and wire' (ISO 15630-1:2010).

Jendele, L., and Cervenka, J. (2006). 'Finite element modelling of reinforcement with bond'. *Computers and Structures*, 84(28), 1780–1791.

Kim, S. W., and Yun, H. Do. (2013). 'Influence of recycled coarse aggregates on the bond behavior of deformed bars in concrete'. *Engineering Structures*, 48, 133–143.

Kim, S. W., and Yun, H. Do. (2014). 'Evaluation of the bond behavior of steel reinforcing bars in recycled fine aggregate concrete'. *Cement and Concrete Composites*, Elsevier Ltd, 46, 8–18.

Kim, S. W., Yun, H. Do, Park, W. S., and Jang, Y. Il. (2015). 'Bond strength prediction for deformed steel rebar embedded in recycled coarse aggregate concrete'. *Materials and Design*, Elsevier Ltd, 83, 257–269.

Kosmatka, S. H., Kerkhoff, B., and Panarese, W. C. (1996). *Design and Control of Concrete Mixtures, EB001*. *Design and Control of Concrete Mixtures*.

Lehne, J., and Preston, F. (2018). 'Chatham House Report - Making Concrete Change Innovation in Low-carbon Cement and Concrete'

Li, X., Wu, Z., Zheng, J., Alahdal, A., and Dong, W. (2016). 'Effect of loading rate on the bond behaviour of deformed steel bars in concrete subjected to lateral pressure'. *Materials and Structures/Materiaux et Constructions*, Springer Netherlands, 49(6), 2097–2111.

Li, X., Wu, Z., Zheng, J., and Dong, W. (2015). 'Effect of loading rate on the bond behavior of plain round bars in concrete under lateral pressure'. *Construction and Building Materials*, Elsevier Ltd, 94, 826–836.

Long, W. J., Gu, Y., Liao, J., and Xing, F. (2017). 'Sustainable design and ecological evaluation of low binder self-compacting concrete'. *Journal of Cleaner Production*, Elsevier Ltd, 167, 317–325.

Long, X., Wang, C. Y., Zhao, P. Z., and Kang, S. B. (2020). 'Bond strength of steel reinforcement under different loading rates'. *Construction and Building Materials*, Elsevier Ltd, 238, 117749.

Lorrain, M. S., Caetano, L. F., Silva, B. V., Gomes, L. E. S., Barbosa, M. P., and Silva Filho, L. C. P. (2010). 'Bond strength and rib geometry: A comparative study of the influence of deformation patterns on anchorage bond strength'. *3rd International fib Congress and Exhibition, Incorporating the PCI Annual Convention and Bridge Conference: Think Globally, Build Locally, Proceedings*, (August 2015).

Louro, A. S. (2014). 'Characterization of bond of ribbed bars subjected to repeated and alternating actions' (in Portuguese), *PhD Thesis, Universidade Nova de Lisboa, Lisbon*.

Lv, L., Yang, H., Zhang, T., and Deng, Z. (2018). 'Bond behavior between recycled aggregate concrete and deformed bars under uniaxial lateral pressure'. *Construction and Building Materials*, Elsevier Ltd, 185, 12–19.

Malvar, L. J. (1991). 'Bond of Reinforcement Under Controlled Confinement'. *ACI Materials Journal*, 89(6).

Mayer, U., and Eligehausen, R. (1998). 'Bond behaviour of ribbed bars at inelastic steel strains'. *Proceedings - 2nd International PhD Symposium in Civil Engineering*, (January 1998), 39–46.

Metelli, G., and Plizzari, G. A. (2014). 'Influence of the relative rib area on bond behaviour'. *Magazine of Concrete Research*, 66(6), 277–294.

Moallemi Pour, S., and Alam, M. S. (2016). 'Investigation of Compressive Bond Behavior of Steel Rebar Embedded in Concrete With Partial Recycled Aggregate Replacement'. *Structures*, Elsevier B.V., 7, 153–164.

Niu, Q., Feng, N., Yang, J., and Zheng, X. (2002). 'Effect of superfine slag powder on cement properties'. *Cement and Concrete Research*, 32(4), 615–621.

Orangun, C. O., Jirsa, J. O., and Breen, J. E. (1977). 'Reevaluation of Test Data on Development Length and Splices.' *J Am Concr Inst*, 74(3), 114–122.

Pala, M., Özbay, E., Öztaş, A., and Yuce, M. I. (2007). 'Appraisal of long-term effects of fly ash and silica fume on compressive strength of concrete by neural networks'. *Construction and Building Materials*, 21(2), 384–394.

Pandurangan, K., Dayanithy, A., and Om Prakash, S. (2016). 'Influence of treatment methods on the bond strength of recycled aggregate concrete'. *Construction and Building Materials*, Elsevier Ltd, 120, 212–221.

Pepe, M., Toledo Filho, R. D., Koenders, E. A. B., and Martinelli, E. (2014). 'Alternative processing procedures for recycled aggregates in structural concrete'. *Construction and Building Materials*, Elsevier Ltd, 69, 124–132.

Pereira, T. (2019). 'Bond between steel bars and low binder concrete with the incorporation of recycled aggregates' (in Portuguese), *Master's Thesis, Instituto Superior Técnico, Lisbon*.

Prince, M. J. R., and Singh, B. (2013). 'Bond behaviour of deformed steel bars embedded in recycled aggregate concrete'. *Construction and Building Materials*, Elsevier Ltd, 49, 852–862.

Prince, M. J. R., and Singh, B. (2014). 'Investigation of bond behaviour between recycled aggregate concrete and deformed steel bars'. *Structural Concrete*, 15(2), 154–168.

Robalo, K., Costa, H., do Carmo, R., and Júlio, E. (2020). 'Experimental development of low cement content and recycled construction and demolition waste aggregates concrete'. *Construction and Building Materials*, Elsevier Ltd, 272, 121680.

Robalo, K., Soldado, E., Costa, H., do Carmo, R., Alves, H., and Júlio, E. (2021). 'Efficiency of cement content and of compactness on mechanical performance of low cement concrete designed with packing optimization'. *Construction and Building Materials*, Elsevier Ltd, 266, 121077.

Seara-Paz, S., González-Fonteboa, B., Eiras-López, J., and Herrador, M. F. (2014). 'Bond behavior between steel reinforcement and recycled concrete'. *Materials and Structures/Materiaux et Constructions*, 47(1–2), 323–334.

Shang, H. shuai, Cui, F. kun, Zhang, P., Zhao, T. jun, and Ren, G. sheng. (2017). 'Bond behavior of steel bar embedded in recycled coarse aggregate concrete under lateral compression load'. *Construction and Building Materials*, 150, 529–537.

Shen, D., Shi, X., Zhang, H., Duan, X., and Jiang, G. (2016). 'Experimental study of early-age bond behavior between high strength concrete and steel bars using a pull-out test'. *Construction and Building Materials*, Elsevier Ltd, 113, 653–663.

T. de Grazia, M., F. M. Sanchez, L., C. O. Romano, R., and G. Pileggi, R. (2019). 'Investigation of the use of continuous particle packing models (PPMs) on the fresh and hardened properties of low-cement concrete (LCC) systems'. *Construction and Building Materials*, Elsevier Ltd, 195, 524–536.

Tepfers, R. (1973). 'A Theory of Bond Applied to Overlapped Tensile Reinforcement Splices for Deformed Bars'. *PhD Thesis, Chalmers University of Technology*.

Turk, K., Yildirim, M. S., and Caliskan, S. (2003). 'Effect of reinforcement size on the concrete / reinforcement bond strength'. *Role of Cement Science in Sustainable Development - Proceedings of the International Symposium - Celebrating Concrete: People and Practice*, (January 2017), 47–57.

Vos, E., and Reinhardt, H. W. (1982). 'Influence of loading rate on bond behaviour of reinforcing steel and prestressing strands'. *Matériaux et Constructions*, 15(1), 3–10.

Wassouf, M., Yang, J., and Clark, L. (2015). 'Bond and Ductility of Concrete Reinforced With Various Steel Bars Surface and Ductility Conditions'. *PhD Thesis, Univesity of Birmingham, Birmingham.*

Xiao, J., and Falkner, H. (2007). 'Bond behaviour between recycled aggregate concrete and steel rebars'. *Construction and Building Materials*, 21(2), 395–401.

Xing, G., Zhou, C., Wu, T., and Liu, B. (2015). 'Experimental Study on Bond Behavior between Plain Reinforcing Bars and Concrete'. *Advances in Materials Science and Engineering*.

Xu, J., Shu, S., Han, Q., and Liu, C. (2018). 'Experimental research on bond behavior of reinforced recycled aggregate concrete based on the acoustic emission technique'. *Construction and Building Materials*, Elsevier Ltd, 191, 1230–1241.

Yanweerasak, T., Kea, T. M., Ishibashi, H., and Akiyama, M. (2018). 'Effect of recycled aggregate quality on the bond behavior and shear strength of RC members'. *Applied Sciences (Switzerland)*, 8(11).

Yasojima, A., and Kanakubo, T. (2004). 'Effect of lateral confinement in bond splitting behaviour of RC members'. *13th World Conference on Earthquake Engineering*, 78(11), 74–76.

Yoo, D. Y., and Shin, H. O. (2018). 'Bond performance of steel rebar embedded in 80–180 MPa ultra-high-strength concrete'. *Cement and Concrete Composites*, Elsevier, 93(February), 206–217.

Yousuf, S., Sanchez, L. F. M., and Shammeh, S. A. (2019). 'The use of particle packing models (PPMs) to design structural low cement concrete as an alternative for construction industry'. *Journal of Building Engineering*, Elsevier Ltd, 25(May), 100815.

Zuo, J., and Darwin, D. (1998). 'Bond strength of high relative rib area reinforcing bars'.

Zuo, J., and Darwin, D. (2000). 'Bond slip of high relative rib area bars under cyclic loading'. *ACI Structural Journal*, 97(2), 331–334.

Zuo, W., Liu, J., Tian, Q., Xu, W., She, W., Feng, P., and Miao, C. (2018). 'Optimum design of low-binder Self-Compacting Concrete based on particle packing theories'. *Construction and Building Materials*, 163, 938–948.

# Annexes

# A. Experimental data pool

## A.1 Pull-out test series from Louro (2014)

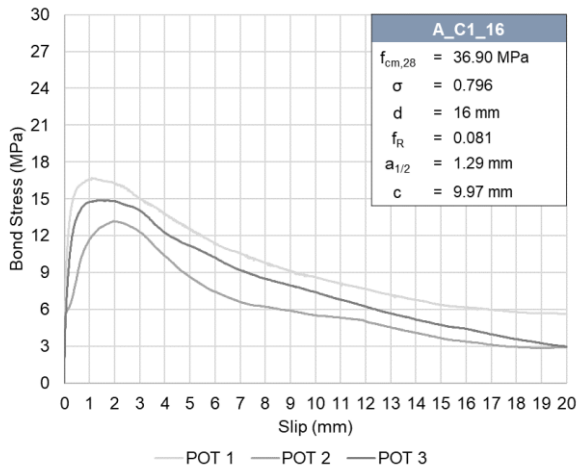


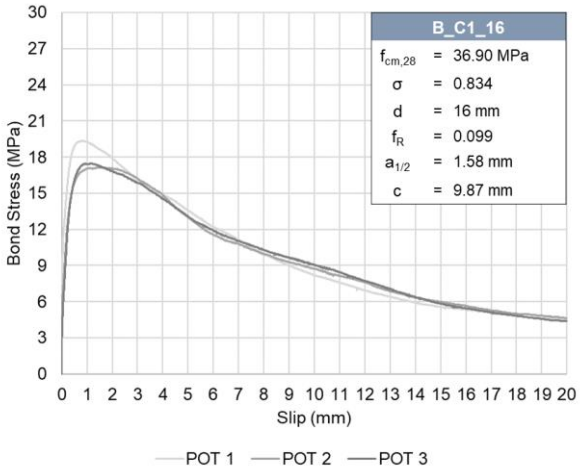


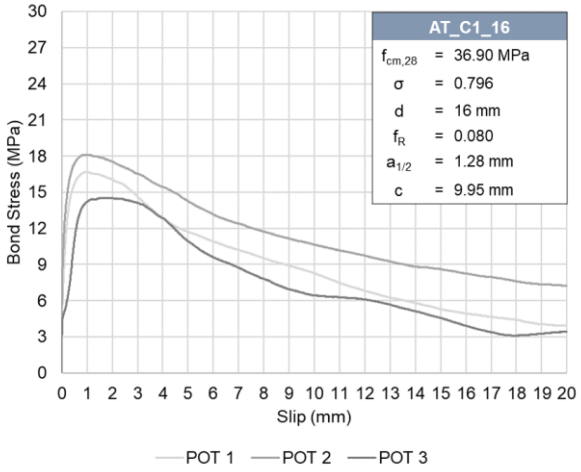


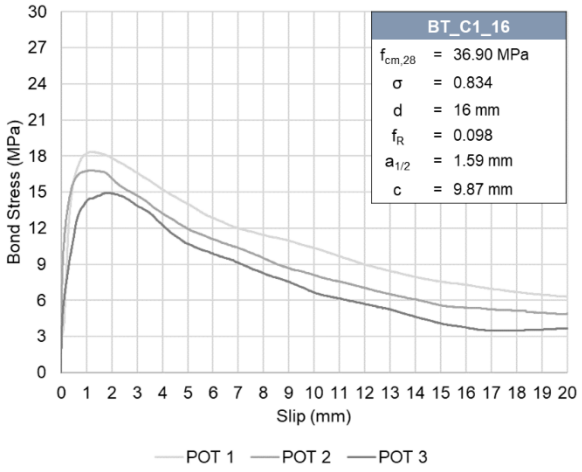


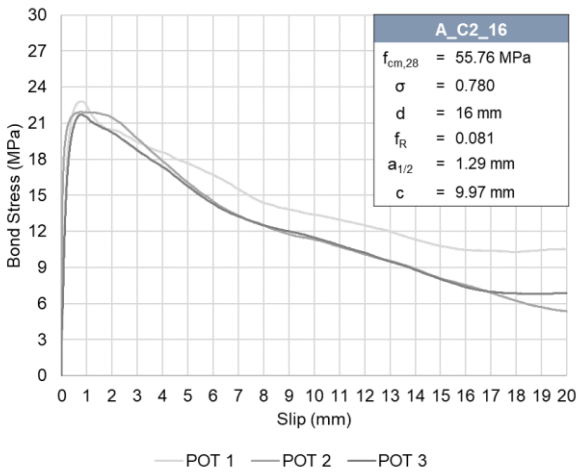


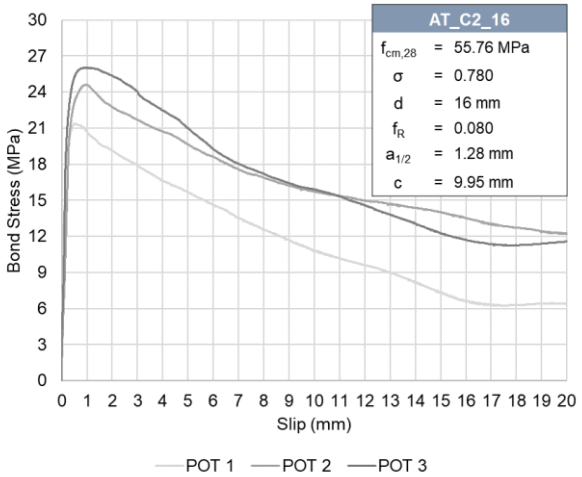

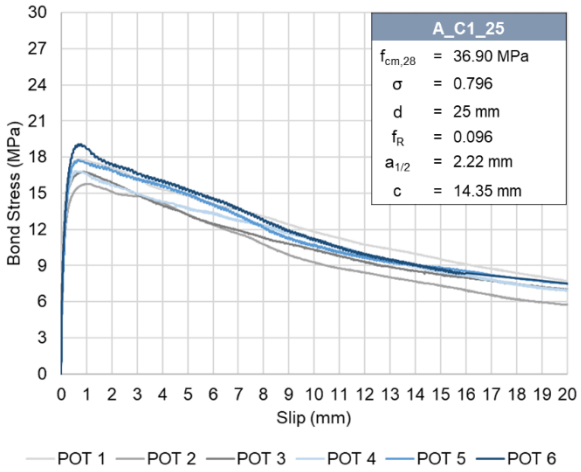
A_C1_25
$f_{cm,28}$ = 36.90 MPa
σ = 0.796
d = 25 mm
$f_R$ = 0.096
$a_{1/2}$ = 2.22 mm
c = 14.35 mm
Bond Stress (MPa)
Slip (mm)
POT 1 POT 2 POT 3 POT 4 POT 5 POT 6

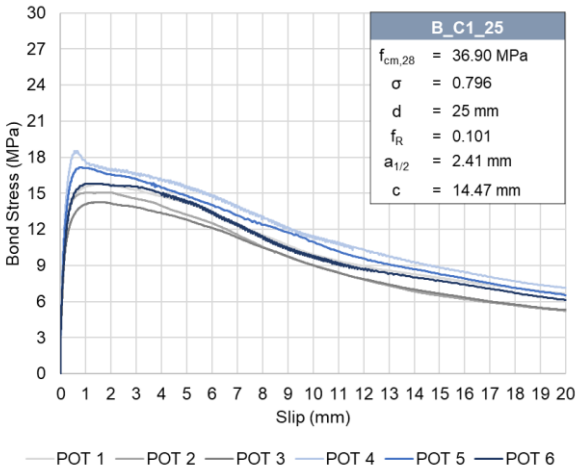
B_C1_25
$f_{cm,28}$ = 36.90 MPa
σ = 0.796
d = 25 mm
$f_R$ = 0.101
$a_{1/2}$ = 2.41 mm
c = 14.47 mm
Bond Stress (MPa)
Slip (mm)
POT 1 POT 2 POT 3 POT 4 POT 5 POT 6

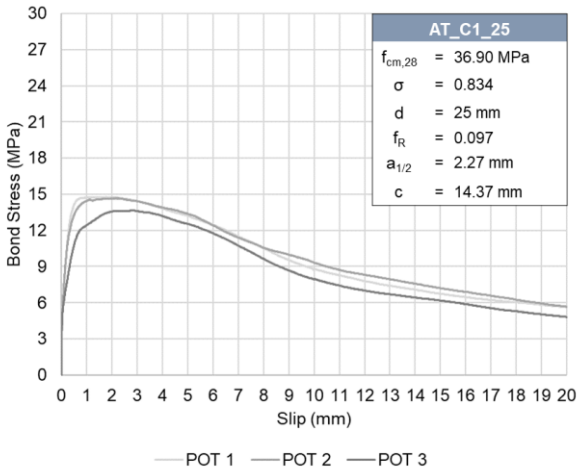
AT_C1_25
$f_{cm,28}$ = 36.90 MPa
σ = 0.834
d = 25 mm
$f_R$ = 0.097
$a_{1/2}$ = 2.27 mm
c = 14.37 mm
Bond Stress (MPa)
Slip (mm)
POT 1 POT 2 POT 3

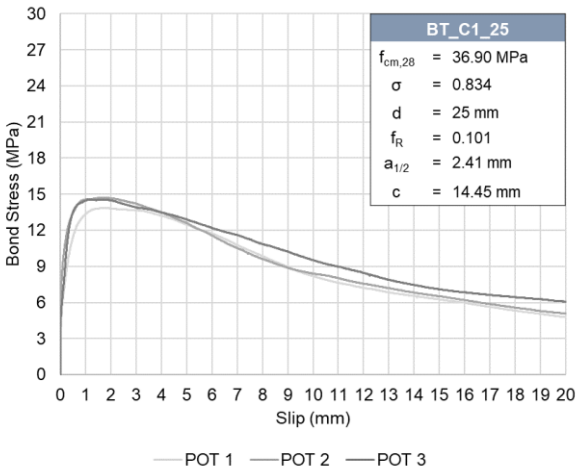
BT_C1_25
$f_{cm,28}$ = 36.90 MPa
σ = 0.834
d = 25 mm
$f_R$ = 0.101
$a_{1/2}$ = 2.41 mm
c = 14.45 mm
Bond Stress (MPa)
Slip (mm)
POT 1 POT 2 POT 3

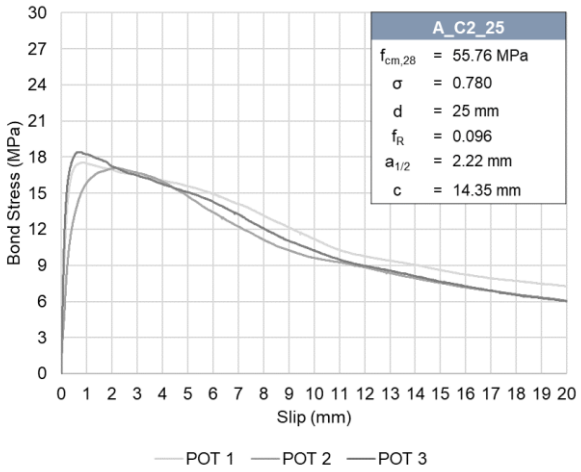
A_C2_25
$f_{cm,28}$ = 55.76 MPa
σ = 0.780
d = 25 mm
$f_R$ = 0.096
$a_{1/2}$ = 2.22 mm
c = 14.35 mm
Bond Stress (MPa)
Slip (mm)
POT 1 POT 2 POT 3

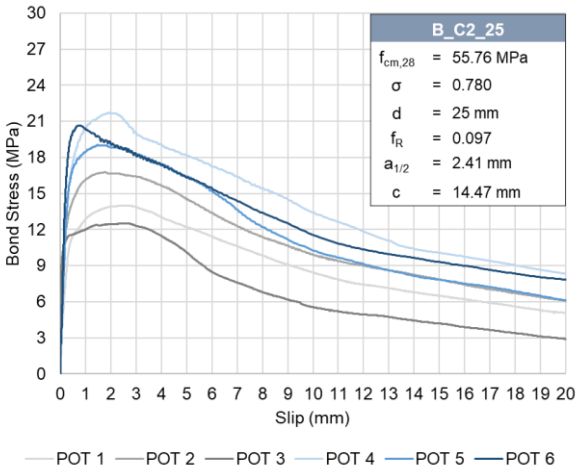
B_C2_25
$f_{cm,28}$ = 55.76 MPa
σ = 0.780
d = 25 mm
$f_R$ = 0.097
$a_{1/2}$ = 2.41 mm
c = 14.47 mm
Bond Stress (MPa)
Slip (mm)
POT 1 POT 2 POT 3 POT 4 POT 5 POT 6

## A2. Pull-out test series from Freitas (2016)

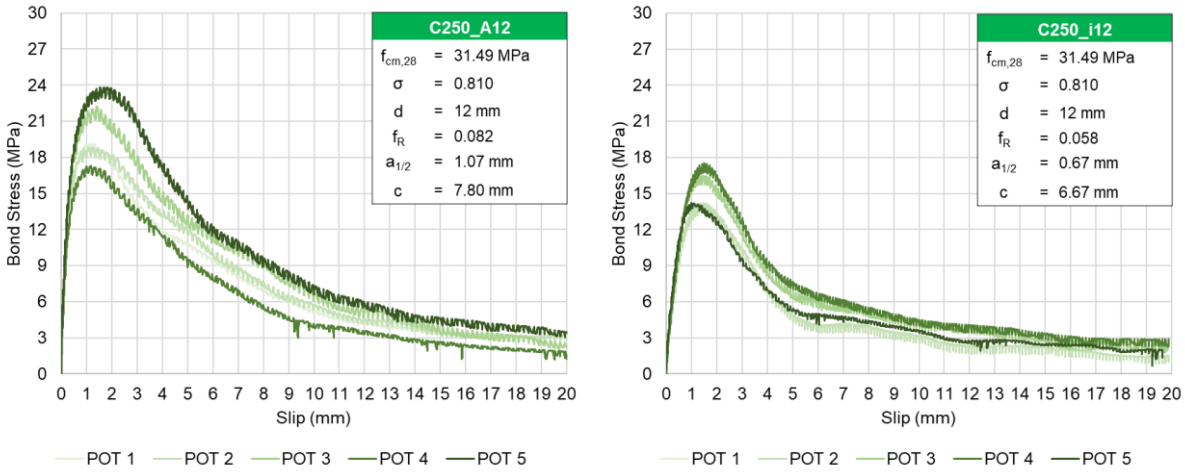





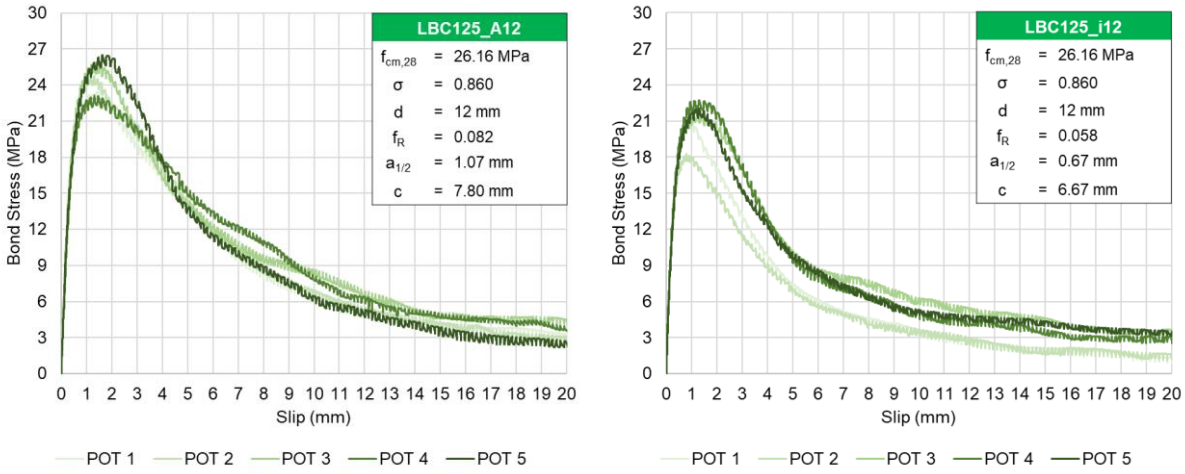





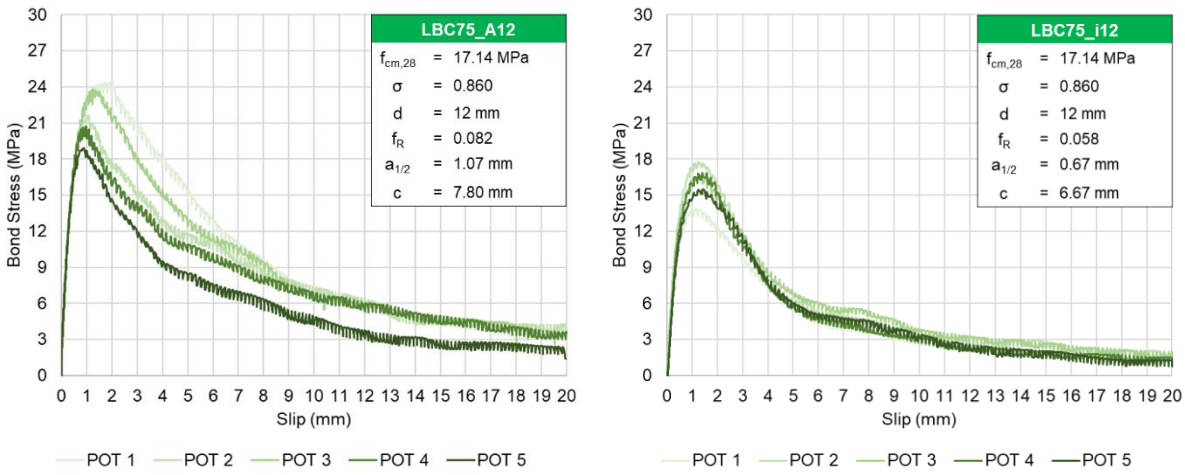

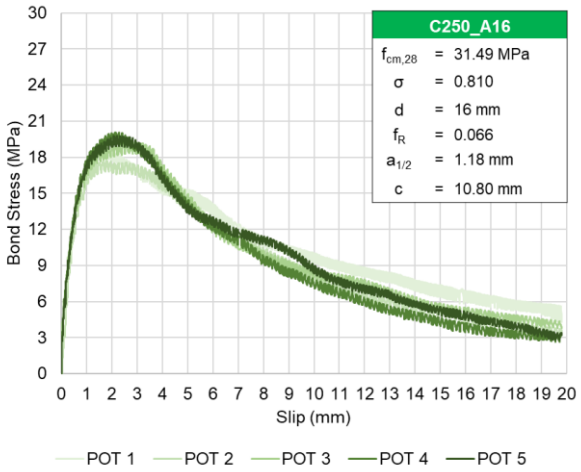
C250_A16
$f_{cm,28}$ = 31.49 MPa
σ = 0.810
d = 16 mm
$f_R$ = 0.066
$a_{1/2}$ = 1.18 mm
c = 10.80 mm
Bond Stress (MPa)
Slip (mm)
POT 1
POT 2
POT 3
POT 4
POT 5

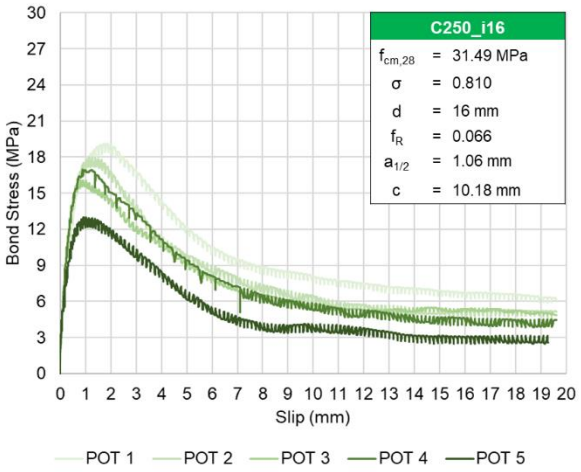
C250_i16
$f_{cm,28}$ = 31.49 MPa
σ = 0.810
d = 16 mm
$f_R$ = 0.066
$a_{1/2}$ = 1.06 mm
c = 10.18 mm
Bond Stress (MPa)
Slip (mm)
POT 1
POT 2
POT 3
POT 4
POT 5

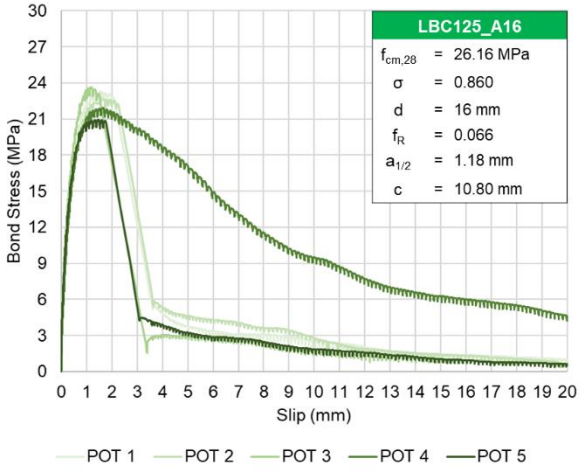
LBC125_A16
$f_{cm,28}$ = 26.16 MPa
σ = 0.860
d = 16 mm
$f_R$ = 0.066
$a_{1/2}$ = 1.18 mm
c = 10.80 mm
Bond Stress (MPa)
Slip (mm)
POT 1
POT 2
POT 3
POT 4
POT 5

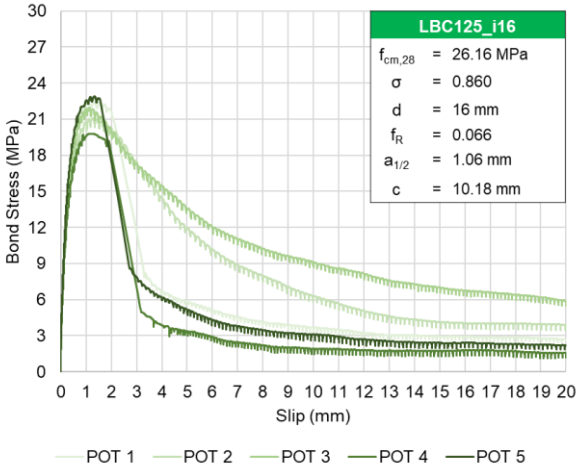
LBC125_i16
$f_{cm,28}$ = 26.16 MPa
σ = 0.860
d = 16 mm
$f_R$ = 0.066
$a_{1/2}$ = 1.06 mm
c = 10.18 mm
Bond Stress (MPa)
Slip (mm)
POT 1
POT 2
POT 3
POT 4
POT 5

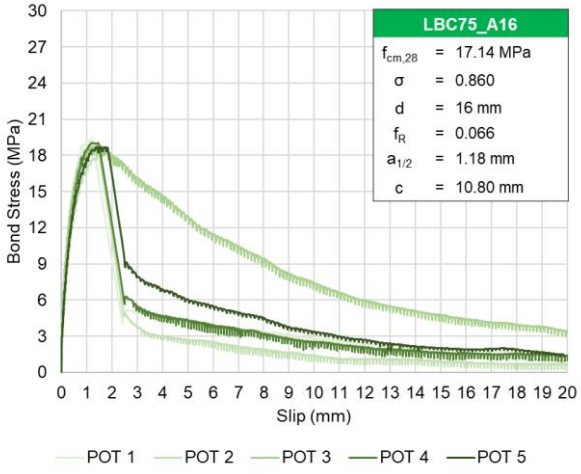
LBC75_A16
$f_{cm,28}$ = 17.14 MPa
σ = 0.860
d = 16 mm
$f_R$ = 0.066
$a_{1/2}$ = 1.18 mm
c = 10.80 mm
Bond Stress (MPa)
Slip (mm)
POT 1
POT 2
POT 3
POT 4
POT 5

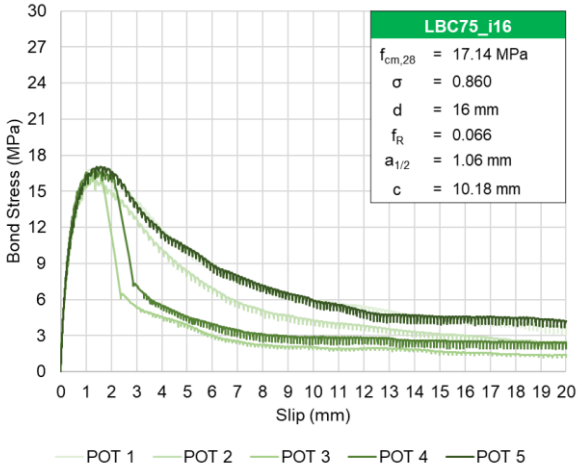
LBC75_i16
$f_{cm,28}$ = 17.14 MPa
σ = 0.860
d = 16 mm
$f_R$ = 0.066
$a_{1/2}$ = 1.06 mm
c = 10.18 mm
Bond Stress (MPa)
Slip (mm)
POT 1
POT 2
POT 3
POT 4
POT 5

## A3. Pull-out test series from Pereira (2019)

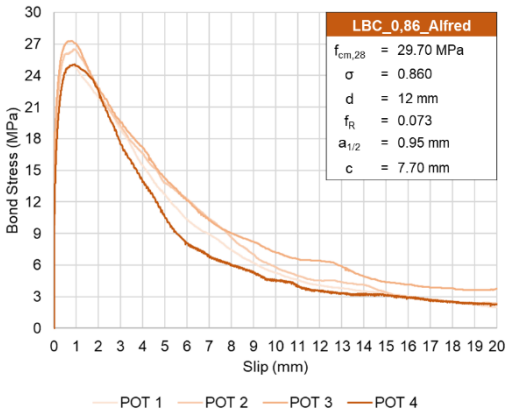


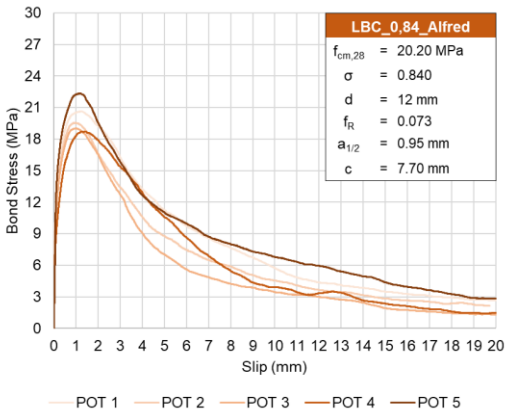


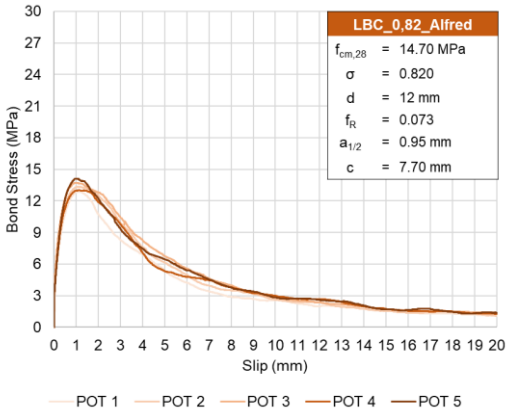


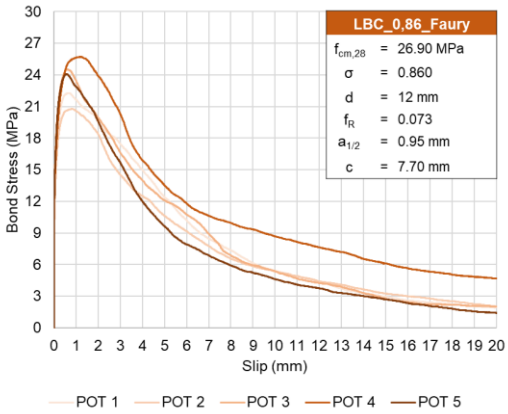


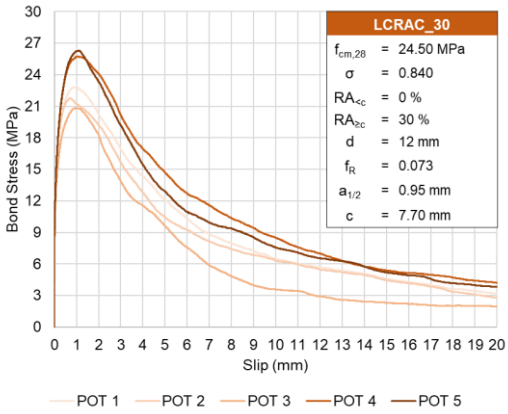


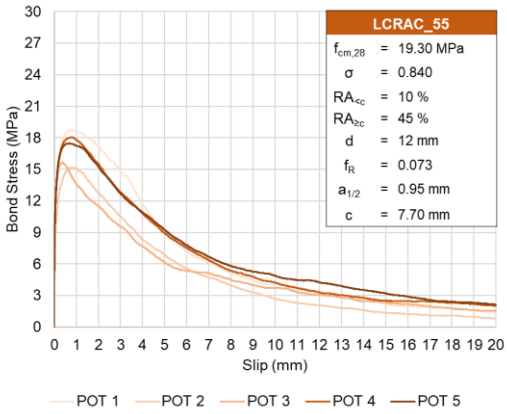


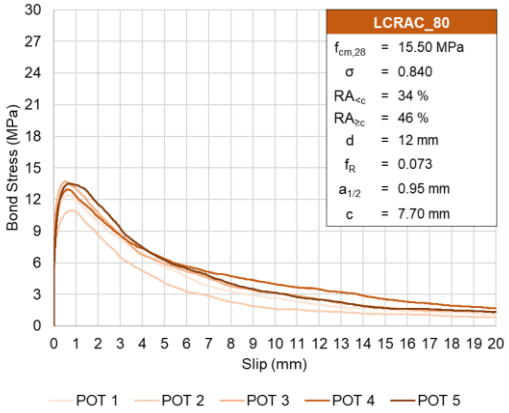

# B. Input values for the bond material of the pull-out model

## B1. Pull-out models for the test series of Louro (2014)

| | | fib MC 2010 | Louro (2014) | Freitas (2016) | Pereira (2019) | New Model | | fib MC 2010 | Louro (2014) | Freitas (2016) | Pereira (2019) | New Model | | |
|---|---|---|---|---|---|---|---|---|---|---|---|---|---|---|
| A_C1_16 | $\tau_{b,0.01}$ | 2.41 | 2.50 | 3.62 | 1.67 | 2.88 | | 2.41 | 3.72 | 5.08 | 5.19 | 3.47 | $\tau_{b,0.01}$ | B_C1_16 |
| | $\tau_{b,0.1}$ | 6.05 | 6.28 | 9.10 | 5.22 | 7.22 | | 6.05 | 9.34 | 12.76 | 11.45 | 8.72 | $\tau_{b,0.1}$ | |
| | $\tau_{b,0.2}$ | 7.98 | 8.28 | 12.01 | 7.37 | 9.53 | | 7.98 | 12.32 | 16.83 | 14.53 | 11.51 | $\tau_{b,0.2}$ | |
| | $\tau_{b,0.4}$ | 10.53 | 10.93 | 15.84 | 10.39 | 12.58 | | 10.53 | 16.26 | 22.21 | 18.44 | 15.18 | $\tau_{b,0.4}$ | |
| | $\tau_{b,0.6}$ | 12.38 | 12.85 | 18.63 | 12.70 | 14.79 | MPa | 12.38 | - | 26.13 | 21.21 | 17.86 | $\tau_{b,0.6}$ | |
| | $\tau_{b,0.8}$ | 13.89 | 14.42 | 20.91 | 14.65 | 16.60 | | 13.89 | - | 29.31 | 23.41 | 20.04 | $\tau_{b,0.8}$ | |
| | $\tau_{bmáx}$ | 15.19 | 15.76 | 22.86 | 17.31 | 17.78 | | 15.19 | 17.78 | 32.05 | 24.66 | 21.46 | $\tau_{bmáx}$ | |
| | $\tau_{bf}$ | 6.07 | 6.31 | 9.14 | 6.92 | 8.16 | | 6.07 | 7.11 | 12.82 | 9.86 | 10.07 | $\tau_{bf}$ | |
| | $s_1$ | 1.00 | 1.00 | 1.00 | 1.12 | 0.95 | | 1.00 | 0.50 | 1.00 | 0.93 | 0.95 | $s_1$ | |
| | $s_2$ | 2.00 | 2.00 | 2.00 | 2.12 | 1.95 | mm | 2.00 | 1.50 | 2.00 | 1.93 | 1.95 | $s_2$ | |
| | $s_3$ | 9.97 | 9.97 | 9.97 | 9.97 | 9.97 | | 9.87 | 9.87 | 9.87 | 9.87 | 9.87 | $s_3$ | |
| AT_C1_16 | $\tau_{b,0.01}$ | 2.41 | 2.82 | 3.58 | 1.66 | 2.87 | | 2.41 | 3.72 | 5.03 | 5.17 | 3.46 | $\tau_{b,0.01}$ | BT_C1_16 |
| | $\tau_{b,0.1}$ | 6.05 | 7.08 | 8.98 | 5.20 | 7.20 | | 6.05 | 9.34 | 12.64 | 11.41 | 8.69 | $\tau_{b,0.1}$ | |
| | $\tau_{b,0.2}$ | 7.98 | 9.34 | 11.85 | 7.34 | 9.50 | | 7.98 | 12.32 | 16.68 | 14.48 | 11.47 | $\tau_{b,0.2}$ | |
| | $\tau_{b,0.4}$ | 10.53 | 12.32 | 15.64 | 10.35 | 12.53 | | 10.53 | 16.26 | 22.01 | 18.38 | 15.13 | $\tau_{b,0.4}$ | |
| | $\tau_{b,0.6}$ | 12.38 | 14.49 | 18.39 | 12.65 | 14.74 | MPa | 12.38 | - | 25.88 | 21.13 | 17.80 | $\tau_{b,0.6}$ | |
| | $\tau_{b,0.8}$ | 13.89 | 16.26 | 20.63 | 14.59 | 16.53 | | 13.89 | - | 29.04 | 23.33 | 19.97 | $\tau_{b,0.8}$ | |
| | $\tau_{bmáx}$ | 15.19 | 17.78 | 22.56 | 17.24 | 17.71 | | 15.19 | 17.78 | 31.75 | 24.57 | 21.39 | $\tau_{bmáx}$ | |
| | $\tau_{bf}$ | 6.07 | 7.11 | 9.02 | 6.90 | 8.13 | | 6.07 | 7.11 | 12.70 | 9.83 | 10.03 | $\tau_{bf}$ | |
| | $s_1$ | 1.00 | 1.00 | 1.00 | 1.12 | 0.95 | | 1.00 | 0.50 | 1.00 | 0.93 | 0.95 | $s_1$ | |
| | $s_2$ | 2.00 | 2.00 | 2.00 | 2.12 | 1.95 | mm | 2.00 | 1.50 | 2.00 | 1.93 | 1.95 | $s_2$ | |
| | $s_3$ | 9.95 | 9.95 | 9.95 | 9.95 | 9.95 | | 9.87 | 9.87 | 9.87 | 9.87 | 9.87 | $s_3$ | |
| A_C2_16 | $\tau_{b,0.01}$ | 2.96 | 3.46 | 4.25 | 1.25 | 3.79 | | 2.96 | 3.46 | 4.19 | 1.25 | 3.77 | $\tau_{b,0.01}$ | AT_C2_16 |
| | $\tau_{b,0.1}$ | 7.43 | 8.70 | 10.68 | 4.55 | 9.52 | | 7.43 | 8.70 | 10.53 | 4.53 | 9.48 | $\tau_{b,0.1}$ | |
| | $\tau_{b,0.2}$ | 9.81 | 11.48 | 14.09 | 6.70 | 12.56 | | 9.81 | 11.48 | 13.89 | 6.68 | 12.51 | $\tau_{b,0.2}$ | |
| | $\tau_{b,0.4}$ | 12.94 | 15.15 | 18.59 | 9.88 | 16.57 | | 12.94 | 15.15 | 18.33 | 9.85 | 16.51 | $\tau_{b,0.4}$ | |
| | $\tau_{b,0.6}$ | 15.22 | 17.81 | 21.86 | 12.40 | 19.49 | MPa | 15.22 | 17.81 | 21.56 | 12.36 | 19.41 | $\tau_{b,0.6}$ | |
| | $\tau_{b,0.8}$ | 17.07 | 19.99 | 24.53 | 14.57 | 21.86 | | 17.07 | 19.99 | 24.19 | 14.52 | 21.78 | $\tau_{b,0.8}$ | |
| | $\tau_{bmáx}$ | 18.67 | 21.85 | 26.82 | 18.29 | 23.42 | | 18.67 | 21.85 | 26.45 | 18.22 | 23.33 | $\tau_{bmáx}$ | |
| | $\tau_{bf}$ | 7.47 | 8.74 | 10.73 | 7.31 | 11.08 | | 7.47 | 8.74 | 10.58 | 7.29 | 11.03 | $\tau_{bf}$ | |
| | $s_1$ | 1.00 | 1.00 | 1.00 | 1.20 | 0.95 | | 1.00 | 1.00 | 1.00 | 1.20 | 0.95 | $s_1$ | |
| | $s_2$ | 2.00 | 2.00 | 2.00 | 2.20 | 1.95 | mm | 2.00 | 2.00 | 2.00 | 2.20 | 1.95 | $s_2$ | |
| | $s_3$ | 9.97 | 9.97 | 9.97 | 9.97 | 9.97 | | 9.95 | 9.95 | 9.95 | 9.95 | 9.95 | $s_3$ | |

| | | fib MC 2010 | Louro (2014) | Freitas (2016) | Pereira (2019) | New Model | | fib MC 2010 | Louro (2014) | Freitas (2016) | Pereira (2019) | New Model | | |
|---|---|---|---|---|---|---|---|---|---|---|---|---|---|---|
| A_C1_25 | $T_{b,0.01}$ | 2.41 | 3.72 | 4.33 | 1.76 | 1.92 | | 2.41 | 3.72 | 4.57 | 1.79 | 1.95 | $T_{b,0.01}$ | B_C1_25 |
| | $T_{b,0,1}$ | 6.05 | 9.34 | 10.89 | 5.52 | 4.81 | | 6.05 | 9.34 | 11.48 | 5.62 | 4.90 | $T_{b,0,1}$ | |
| | $T_{b,0.2}$ | 7.98 | 12.32 | 14.37 | 7.78 | 6.35 | | 7.98 | 12.32 | 15.15 | 7.92 | 6.46 | $T_{b,0.2}$ | |
| | $T_{b,0.4}$ | 10.53 | 16.26 | 18.96 | 10.97 | 8.38 | | 10.53 | 16.26 | 20.00 | 11.17 | 8.53 | $T_{b,0.4}$ | |
| | $T_{b,0.6}$ | 12.38 | 19.12 | 22.30 | 13.42 | 9.85 | MPa | 12.38 | - | 23.52 | 13.66 | 10.03 | $T_{b,0.6}$ | |
| | $T_{b,0.8}$ | 13.89 | - | 25.01 | 15.48 | 11.05 | | 13.89 | - | 26.38 | 15.75 | 11.25 | $T_{b,0.8}$ | |
| | $T_{bmáx}$ | 15.19 | - | 27.35 | 18.29 | 13.83 | | 15.19 | 17.78 | 28.85 | 18.61 | 14.07 | $T_{bmáx}$ | |
| | $T_{bf}$ | 6.07 | 7.11 | 10.94 | 7.31 | 6.12 | | 6.07 | 7.11 | 11.54 | 7.45 | 6.25 | $T_{bf}$ | |
| | $S_1$ | 1.00 | 0.50 | 1.00 | 1.12 | 1.40 | | 1.00 | 0.50 | 1.00 | 1.12 | 1.40 | $S_1$ | |
| | $S_2$ | 2.00 | 1.50 | 2.00 | 2.12 | 2.40 | mm | 2.00 | 1.00 | 2.00 | 2.12 | 2.40 | $S_2$ | |
| | $S_3$ | 14.35 | 14.35 | 14.35 | 14.35 | 14.35 | | 14.47 | 14.47 | 14.47 | 14.47 | 14.47 | $S_3$ | |
| AT_C1_25 | $T_{b,0.01}$ | 2.41 | 3.30 | 4.98 | 5.15 | 2.17 | | 2.41 | 3.30 | 5.17 | 5.22 | 2.20 | $T_{b,0.01}$ | BT_C1_25 |
| | $T_{b,0,1}$ | 6.05 | 8.28 | 12.52 | 11.37 | 5.46 | | 6.05 | 8.28 | 13.00 | 11.53 | 5.54 | $T_{b,0,1}$ | |
| | $T_{b,0.2}$ | 7.98 | 10.93 | 16.52 | 14.43 | 7.20 | | 7.98 | 10.93 | 17.15 | 14.63 | 7.31 | $T_{b,0.2}$ | |
| | $T_{b,0.4}$ | 10.53 | 14.42 | 21.80 | 18.31 | 9.51 | | 10.53 | 14.42 | 22.63 | 18.57 | 9.64 | $T_{b,0.4}$ | |
| | $T_{b,0.6}$ | 12.38 | - | 25.64 | 21.06 | 11.18 | MPa | 12.38 | - | 26.61 | 21.35 | 11.34 | $T_{b,0.6}$ | |
| | $T_{b,0.8}$ | 13.89 | - | 28.76 | 23.25 | 12.54 | | 13.89 | - | 29.86 | 23.58 | 12.72 | $T_{b,0.8}$ | |
| | $T_{bmáx}$ | 15.19 | 15.76 | 31.45 | 24.48 | 15.69 | | 15.19 | 15.76 | 32.65 | 24.83 | 15.91 | $T_{bmáx}$ | |
| | $T_{bf}$ | 6.07 | 6.31 | 12.58 | 9.79 | 7.08 | | 6.07 | 6.31 | 13.06 | 9.93 | 7.20 | $T_{bf}$ | |
| | $S_1$ | 1.00 | 0.50 | 1.00 | 0.93 | 1.40 | | 1.00 | 0.50 | 1.00 | 0.93 | 1.40 | $S_1$ | |
| | $S_2$ | 2.00 | 1.50 | 2.00 | 1.93 | 2.40 | mm | 2.00 | 1.50 | 2.00 | 1.93 | 2.40 | $S_2$ | |
| | $S_3$ | 14.37 | 14.37 | 14.37 | 14.37 | 14.37 | | 14.45 | 14.45 | 14.45 | 14.45 | 14.45 | $S_3$ | |
| A_C2_25 | $T_{b,0.01}$ | 2.96 | 4.05 | 5.13 | 1.32 | 2.52 | | 2.96 | 4.05 | 5.18 | 1.33 | 2.53 | $T_{b,0.01}$ | B_C2_25 |
| | $T_{b,0,1}$ | 7.43 | 10.18 | 12.88 | 4.80 | 6.34 | | 7.43 | 10.18 | 13.02 | 4.82 | 6.36 | $T_{b,0,1}$ | |
| | $T_{b,0.2}$ | 9.81 | 13.43 | 16.99 | 7.08 | 8.36 | | 9.81 | 13.43 | 17.18 | 7.11 | 8.39 | $T_{b,0.2}$ | |
| | $T_{b,0.4}$ | 12.94 | 17.72 | 22.42 | 10.44 | 11.04 | | 12.94 | 17.72 | 22.67 | 10.48 | 11.08 | $T_{b,0.4}$ | |
| | $T_{b,0.6}$ | 15.22 | - | 26.36 | 13.10 | 12.98 | MPa | 15.22 | - | 26.66 | 13.15 | 13.03 | $T_{b,0.6}$ | |
| | $T_{b,0.8}$ | 17.07 | - | 29.58 | 15.39 | 14.56 | | 17.07 | - | 29.92 | 15.45 | 14.61 | $T_{b,0.8}$ | |
| | $T_{bmáx}$ | 18.67 | 19.38 | 32.34 | 19.32 | 18.22 | | 18.67 | 19.38 | 32.71 | 19.39 | 18.28 | $T_{bmáx}$ | |
| | $T_{bf}$ | 7.47 | 7.75 | 12.94 | 7.73 | 8.39 | | 7.47 | 7.75 | 13.08 | 7.75 | 8.42 | $T_{bf}$ | |
| | $S_1$ | 1.00 | 0.50 | 1.00 | 1.20 | 1.40 | | 1.00 | 0.50 | 1.00 | 1.20 | 1.40 | $S_1$ | |
| | $S_2$ | 2.00 | 1.50 | 2.00 | 2.20 | 2.40 | mm | 2.00 | 1.50 | 2.00 | 2.20 | 2.40 | $S_2$ | |
| | $S_3$ | 14.35 | 14.35 | 14.35 | 14.35 | 14.35 | | 14.47 | 14.47 | 14.47 | 14.47 | 14.47 | $S_3$ | |

## B2. Pull-out models for the test series of Freitas (2016)

| | | fib MC 2010 | Louro (2014) | Freitas (2016) | Pereira (2019) | New Model | | fib MC 2010 | Louro (2014) | Freitas (2016) | Pereira (2019) | New Model | | |
|---|---|---|---|---|---|---|---|---|---|---|---|---|---|---|
| C250_A12 | $\tau_{b,0.01}$ | 2.22 | 2.60 | 3.60 | 2.33 | 3.27 | | 2.22 | 2.60 | 2.54 | 2.12 | 2.98 | $\tau_{b,0.01}$ | C250_i12 |
| | $\tau_{b,0.1}$ | 5.59 | 6.54 | 9.03 | 6.41 | 8.22 | | 5.59 | 6.54 | 6.39 | 5.83 | 7.48 | $\tau_{b,0.1}$ | |
| | $\tau_{b,0.2}$ | 7.37 | 8.63 | 11.92 | 8.69 | 10.84 | | 7.37 | 8.63 | 8.43 | 7.91 | 9.87 | $\tau_{b,0.2}$ | |
| | $\tau_{b,0.4}$ | 9.72 | 11.38 | 15.72 | 11.79 | 14.31 | | 9.72 | 11.38 | 11.12 | 10.73 | 13.02 | $\tau_{b,0.4}$ | |
| | $\tau_{b,0.6}$ | 11.44 | 13.39 | 18.49 | 14.09 | 16.83 | MPa | 11.44 | 13.39 | 13.08 | 12.82 | 15.31 | $\tau_{b,0.6}$ | |
| | $\tau_{b,0.8}$ | 12.83 | 15.02 | 20.75 | 15.99 | - | | 12.83 | 15.02 | 14.68 | 14.55 | - | $\tau_{b,0.8}$ | |
| | $\tau_{bmáx}$ | 14.03 | 16.42 | 22.69 | 18.03 | 18.40 | | 14.03 | 16.42 | 16.05 | 16.40 | 16.74 | $\tau_{bmáx}$ | |
| | $\tau_{bf}$ | 5.61 | 6.57 | 9.07 | 7.21 | 8.48 | | 5.61 | 6.57 | 6.42 | 6.56 | 7.63 | $\tau_{bf}$ | |
| | $s_1$ | 1.00 | 1.00 | 1.00 | 1.05 | 0.75 | | 1.00 | 1.00 | 1.00 | 1.05 | 0.75 | $s_1$ | |
| | $s_2$ | 2.00 | 2.00 | 2.00 | 2.05 | 1.75 | mm | 2.00 | 2.00 | 2.00 | 2.05 | 1.75 | $s_2$ | |
| | $s_3$ | 7.80 | 7.80 | 7.80 | 7.80 | 7.80 | | 6.67 | 6.67 | 6.67 | 6.67 | 6.67 | $s_3$ | |
| | | | | | | | | | | | | | | |
| LBC125_A12 | $\tau_{b,0.01}$ | 2.03 | 2.37 | 4.07 | 7.99 | 4.37 | | 2.03 | 2.37 | 3.11 | 7.27 | 3.98 | $\tau_{b,0.01}$ | LBC125_i12 |
| | $\tau_{b,0.1}$ | 5.09 | 5.96 | 10.22 | 13.88 | 10.98 | | 5.09 | 5.96 | 7.81 | 12.63 | 9.99 | $\tau_{b,0.1}$ | |
| | $\tau_{b,0.2}$ | 6.72 | 7.86 | 13.49 | 16.39 | 14.49 | | 6.72 | 7.86 | 10.31 | 14.91 | 13.18 | $\tau_{b,0.2}$ | |
| | $\tau_{b,0.4}$ | 8.86 | 10.37 | 17.80 | 19.36 | 19.11 | | 8.86 | 10.37 | 13.60 | 17.61 | 17.39 | $\tau_{b,0.4}$ | |
| | $\tau_{b,0.6}$ | 10.42 | 12.20 | 20.93 | 21.33 | 22.48 | MPa | 10.42 | 12.20 | 16.00 | 19.41 | 20.46 | $\tau_{b,0.6}$ | |
| | $\tau_{b,0.8}$ | 11.69 | 13.69 | 23.48 | 22.86 | - | | 11.69 | 13.69 | 17.95 | 20.80 | - | $\tau_{b,0.8}$ | |
| | $\tau_{bmáx}$ | 12.79 | 14.97 | 25.68 | 22.86 | 24.58 | | 12.79 | 14.97 | 19.62 | 20.80 | 22.37 | $\tau_{bmáx}$ | |
| | $\tau_{bf}$ | 5.11 | 5.99 | 10.27 | 6.86 | 8.49 | | 5.11 | 5.99 | 7.85 | 6.24 | 7.65 | $\tau_{bf}$ | |
| | $s_1$ | 1.00 | 1.00 | 1.00 | 0.80 | 0.75 | | 1.00 | 1.00 | 1.00 | 0.80 | 0.75 | $s_1$ | |
| | $s_2$ | 2.00 | 2.00 | 2.00 | 1.80 | 1.75 | mm | 2.00 | 2.00 | 2.00 | 1.80 | 1.75 | $s_2$ | |
| | $s_3$ | 7.80 | 7.80 | 7.80 | 7.80 | 7.80 | | 6.67 | 6.67 | 6.67 | 6.67 | 6.67 | $s_3$ | |
| | | | | | | | | | | | | | | |
| LBC75_A12 | $\tau_{b,0.01}$ | 1.64 | 1.92 | 3.45 | 6.46 | 3.54 | | 1.64 | 1.92 | 2.67 | 5.88 | 3.22 | $\tau_{b,0.01}$ | LBC75_i12 |
| | $\tau_{b,0.1}$ | 4.12 | 4.82 | 8.65 | 11.23 | 8.89 | | 4.12 | 4.82 | 6.70 | 10.22 | 8.09 | $\tau_{b,0.1}$ | |
| | $\tau_{b,0.2}$ | 5.44 | 6.36 | 11.42 | 13.27 | 11.73 | | 5.44 | 6.36 | 8.85 | 12.07 | 10.67 | $\tau_{b,0.2}$ | |
| | $\tau_{b,0.4}$ | 7.17 | 8.40 | 15.07 | 15.67 | 15.47 | | 7.17 | 8.40 | 11.67 | 14.26 | 14.08 | $\tau_{b,0.4}$ | |
| | $\tau_{b,0.6}$ | 8.44 | 9.88 | 17.72 | 17.27 | 18.20 | MPa | 8.44 | 9.88 | 13.73 | 15.71 | 16.56 | $\tau_{b,0.6}$ | |
| | $\tau_{b,0.8}$ | 9.47 | 11.08 | 19.88 | 18.50 | - | | 9.47 | 11.08 | 15.40 | 16.84 | - | $\tau_{b,0.8}$ | |
| | $\tau_{bmáx}$ | 10.35 | 12.12 | 21.74 | 18.50 | 19.89 | | 10.35 | 12.12 | 16.84 | 16.84 | 18.10 | $\tau_{bmáx}$ | |
| | $\tau_{bf}$ | 4.14 | 4.85 | 8.69 | 5.55 | 6.70 | | 4.14 | 4.85 | 6.74 | 5.05 | 6.02 | $\tau_{bf}$ | |
| | $s_1$ | 1.00 | 1.00 | 1.00 | 0.80 | 0.75 | | 1.00 | 1.00 | 1.00 | 0.80 | 0.75 | $s_1$ | |
| | $s_2$ | 2.00 | 2.00 | 2.00 | 1.80 | 1.75 | mm | 2.00 | 2.00 | 2.00 | 1.80 | 1.75 | $s_2$ | |
| | $s_3$ | 7.80 | 7.80 | 7.80 | 7.80 | 7.80 | | 6.67 | 6.67 | 6.67 | 6.67 | 6.67 | $s_3$ | |

| | | fib MC 2010 | Louro (2014) | Freitas (2016) | Pereira (2019) | New Model | | fib MC 2010 | Louro (2014) | Freitas (2016) | Pereira (2019) | New Model | | |
|---|---|---|---|---|---|---|---|---|---|---|---|---|---|---|
| C250_A16 | $T_{b,0.01}$ | 2.22 | 2.60 | 2.89 | 2.19 | 2.50 | MPa | 2.22 | 2.60 | 2.89 | 2.19 | 2.50 | $T_{b,0.01}$ | C250_i16 |
| | $T_{b,0,1}$ | 5.59 | 6.54 | 7.27 | 6.02 | 6.29 | | 5.59 | 6.54 | 7.27 | 6.02 | 6.29 | $T_{b,0,1}$ | |
| | $T_{b,0.2}$ | 7.37 | 8.63 | 9.59 | 8.17 | 8.30 | | 7.37 | 8.63 | 9.59 | 8.17 | 8.30 | $T_{b,0.2}$ | |
| | $T_{b,0.4}$ | 9.72 | 11.38 | 12.66 | 11.08 | 10.95 | | 9.72 | 11.38 | 12.66 | 11.08 | 10.95 | $T_{b,0.4}$ | |
| | $T_{b,0.6}$ | 11.44 | 13.39 | 14.88 | 13.25 | 12.88 | | 11.44 | 13.39 | 14.88 | 13.25 | 12.88 | $T_{b,0.6}$ | |
| | $T_{b,0.8}$ | 12.83 | 15.02 | 16.70 | 15.03 | 14.45 | | 12.83 | 15.02 | 16.70 | 15.03 | 14.45 | $T_{b,0.8}$ | |
| | $T_{bmáx}$ | 14.03 | 16.42 | 18.26 | 16.94 | 15.48 | | 14.03 | 16.42 | 18.26 | 16.94 | 15.48 | $T_{bmáx}$ | |
| | $T_{bf}$ | 5.61 | 6.57 | 7.30 | 6.78 | 6.98 | | 5.61 | 6.57 | 7.30 | 6.78 | 6.98 | $T_{bf}$ | |
| | $S_1$ | 1.00 | 1.00 | 1.00 | 1.05 | 0.95 | mm | 1.00 | 1.00 | 1.00 | 1.05 | 0.95 | $S_1$ | |
| | $S_2$ | 2.00 | 2.00 | 2.00 | 2.05 | 1.95 | | 2.00 | 2.00 | 2.00 | 2.05 | 1.95 | $S_2$ | |
| | $S_3$ | 10.80 | 10.80 | 10.80 | 10.80 | 10.80 | | 10.18 | 10.18 | 10.18 | 10.18 | 10.18 | $S_3$ | |
| LBC125_A16 | $T_{b,0.01}$ | 2.03 | 2.37 | 3.43 | 7.51 | 3.35 | MPa | 2.03 | 2.37 | 3.43 | 7.51 | 3.35 | $T_{b,0.01}$ | LBC125_i16 |
| | $T_{b,0,1}$ | 5.09 | 5.96 | 8.62 | 13.04 | 8.40 | | 5.09 | 5.96 | 8.62 | 13.04 | 8.40 | $T_{b,0,1}$ | |
| | $T_{b,0.2}$ | 6.72 | 7.86 | 11.37 | 15.41 | 11.09 | | 6.72 | 7.86 | 11.37 | 15.41 | 11.09 | $T_{b,0.2}$ | |
| | $T_{b,0.4}$ | 8.86 | 10.37 | 15.00 | 18.19 | 14.63 | | 8.86 | 10.37 | 15.00 | 18.19 | 14.63 | $T_{b,0.4}$ | |
| | $T_{b,0.6}$ | 10.42 | 12.20 | 17.64 | 20.05 | 17.21 | | 10.42 | 12.20 | 17.64 | 20.05 | 17.21 | $T_{b,0.6}$ | |
| | $T_{b,0.8}$ | 11.69 | 13.69 | 19.79 | 21.49 | 19.31 | | 11.69 | 13.69 | 19.79 | 21.49 | 19.31 | $T_{b,0.8}$ | |
| | $T_{bmáx}$ | 12.79 | 14.97 | 21.64 | 21.49 | 20.68 | | 12.79 | 14.97 | 21.64 | 21.49 | 20.68 | $T_{bmáx}$ | |
| | $T_{bf}$ | 5.11 | 5.99 | 8.66 | 6.45 | 7.00 | | 5.11 | 5.99 | 8.66 | 6.45 | 7.00 | $T_{bf}$ | |
| | $S_1$ | 1.00 | 1.00 | 1.00 | 0.80 | 0.95 | mm | 1.00 | 1.00 | 1.00 | 0.80 | 0.95 | $S_1$ | |
| | $S_2$ | 2.00 | 2.00 | 2.00 | 1.80 | 1.95 | | 2.00 | 2.00 | 2.00 | 1.80 | 1.95 | $S_2$ | |
| | $S_3$ | 10.80 | 10.80 | 10.80 | 10.80 | 10.80 | | 10.18 | 10.18 | 10.18 | 10.18 | 10.18 | $S_3$ | |
| LBC75_A16 | $T_{b,0.01}$ | 1.64 | 1.92 | 2.93 | 6.08 | 2.71 | MPa | 1.64 | 1.92 | 2.93 | 6.08 | 2.71 | $T_{b,0.01}$ | LBC75_i16 |
| | $T_{b,0,1}$ | 4.12 | 4.82 | 7.35 | 10.56 | 6.80 | | 4.12 | 4.82 | 7.35 | 10.56 | 6.80 | $T_{b,0,1}$ | |
| | $T_{b,0.2}$ | 5.44 | 6.36 | 9.70 | 12.47 | 8.98 | | 5.44 | 6.36 | 9.70 | 12.47 | 8.98 | $T_{b,0.2}$ | |
| | $T_{b,0.4}$ | 7.17 | 8.40 | 12.80 | 14.73 | 11.84 | | 7.17 | 8.40 | 12.80 | 14.73 | 11.84 | $T_{b,0.4}$ | |
| | $T_{b,0.6}$ | 8.44 | 9.88 | 15.06 | 16.23 | 13.93 | | 8.44 | 9.88 | 15.06 | 16.23 | 13.93 | $T_{b,0.6}$ | |
| | $T_{b,0.8}$ | 9.47 | 11.08 | 16.89 | 17.39 | 15.63 | | 9.47 | 11.08 | 16.89 | 17.39 | 15.63 | $T_{b,0.8}$ | |
| | $T_{bmáx}$ | 10.35 | 12.12 | 18.47 | 17.39 | 16.74 | | 10.35 | 12.12 | 18.47 | 17.39 | 16.74 | $T_{bmáx}$ | |
| | $T_{bf}$ | 4.14 | 4.85 | 7.39 | 5.22 | 5.49 | | 4.14 | 4.85 | 7.39 | 5.22 | 5.49 | $T_{bf}$ | |
| | $S_1$ | 1.00 | 1.00 | 1.00 | 0.80 | 0.95 | mm | 1.00 | 1.00 | 1.00 | 0.80 | 0.95 | $S_1$ | |
| | $S_2$ | 2.00 | 2.00 | 2.00 | 1.80 | 1.95 | | 2.00 | 2.00 | 2.00 | 1.80 | 1.95 | $S_2$ | |
| | $S_3$ | 10.80 | 10.80 | 10.80 | 10.80 | 10.80 | | 10.18 | 10.18 | 10.18 | 10.18 | 10.18 | $S_3$ | |

## B3. Pull-out models for the test series of Pereira (2019)

| | | fib MC 2010 | Louro (2014) | Freitas (2016) | Pereira (2019) | New Model | | fib MC 2010 | Louro (2014) | Freitas (2016) | Pereira (2019) | New Model | | |
|---|---|---|---|---|---|---|---|---|---|---|---|---|---|---|
| LBC_0,86_Alfred | $T_{b,0.01}$ | 2.16 | 2.24 | 3.90 | 8.22 | 4.50 | MPa | 1.78 | 1.85 | 3.04 | 4.08 | 3.02 | $T_{b,0.01}$ | LBC_0,84_Alfred |
| | $T_{b,0,1}$ | 5.42 | 5.63 | 9.80 | 14.29 | 11.30 | | 4.47 | 4.64 | 7.63 | 8.53 | 7.58 | $T_{b,0,1}$ | |
| | $T_{b,0.2}$ | 7.16 | 7.43 | 12.93 | 16.87 | 14.91 | | 5.90 | 6.13 | 10.07 | 10.64 | 10.00 | $T_{b,0.2}$ | |
| | $T_{b,0.4}$ | 9.44 | 9.80 | 17.06 | 19.93 | 19.68 | | 7.79 | 8.08 | 13.29 | 13.29 | 13.19 | $T_{b,0.4}$ | |
| | $T_{b,0.6}$ | 11.11 | 11.53 | 20.06 | 21.96 | 23.14 | | 9.16 | 9.51 | 15.63 | 15.13 | 15.51 | $T_{b,0.6}$ | |
| | $T_{b,0.8}$ | 12.46 | 12.94 | 22.51 | 23.53 | 25.97 | | 10.28 | 10.67 | 17.54 | 16.59 | 17.40 | $T_{b,0.8}$ | |
| | $T_{bmáx}$ | 13.62 | 14.14 | 24.61 | 23.53 | 25.30 | | 11.24 | 11.66 | 19.17 | 17.23 | 16.96 | $T_{bmáx}$ | |
| | $T_{bf}$ | 5.45 | 5.66 | 9.85 | 7.06 | 8.77 | | 4.49 | 4.67 | 7.67 | 5.17 | 5.58 | $T_{bf}$ | |
| | $S_1$ | 1.00 | 1.0 | 1.00 | 0.8 | 0.75 | mm | 1.00 | 1.0 | 1.00 | 0.9 | 0.75 | $S_1$ | |
| | $S_2$ | 2.00 | 2.0 | 2.00 | 1.8 | 1.75 | | 2.00 | 2.0 | 2.00 | 1.9 | 1.75 | $S_2$ | |
| | $S_3$ | 7.70 | 7.70 | 7.70 | 7.70 | 7.70 | | 7.70 | 7.70 | 7.70 | 7.70 | 7.70 | $S_3$ | |
| LBC_0,82_Alfred | $T_{b,0.01}$ | 1.52 | 1.58 | 2.35 | 2.03 | 2.23 | MPa | 2.06 | 2.13 | 3.75 | 7.82 | 4.28 | $T_{b,0.01}$ | LBC_0,84_Faury |
| | $T_{b,0,1}$ | 3.82 | 3.96 | 5.89 | 5.11 | 5.61 | | 5.16 | 5.36 | 9.42 | 13.60 | 10.76 | $T_{b,0,1}$ | |
| | $T_{b,0.2}$ | 5.04 | 5.23 | 7.77 | 6.74 | 7.40 | | 6.81 | 7.07 | 12.43 | 16.06 | 14.19 | $T_{b,0.2}$ | |
| | $T_{b,0.4}$ | 6.64 | 6.90 | 10.26 | 8.89 | 9.77 | | 8.99 | 9.33 | 16.40 | 18.97 | 18.73 | $T_{b,0.4}$ | |
| | $T_{b,0.6}$ | 7.81 | 8.11 | 12.06 | 10.46 | 11.49 | | 10.57 | 10.97 | 19.29 | 20.90 | 22.03 | $T_{b,0.6}$ | |
| | $T_{b,0.8}$ | 8.77 | 9.10 | 13.53 | 11.74 | 12.89 | | 11.86 | 12.31 | 21.64 | 22.40 | 24.71 | $T_{b,0.8}$ | |
| | $T_{bmáx}$ | 9.59 | 9.95 | 14.80 | 12.83 | 12.56 | | 12.97 | 13.46 | 23.67 | 22.40 | 24.08 | $T_{bmáx}$ | |
| | $T_{bf}$ | 3.83 | 3.98 | 5.92 | 3.85 | 3.90 | | 5.19 | 5.38 | 9.47 | 6.72 | 8.30 | $T_{bf}$ | |
| | $S_1$ | 1.00 | 1.0 | 1.00 | 1 | 0.75 | mm | 1.00 | 1.0 | 1.00 | 0.8 | 0.75 | $S_1$ | |
| | $S_2$ | 2.00 | 2.0 | 2.00 | 2 | 1.75 | | 2.00 | 2.0 | 2.00 | 1.8 | 1.75 | $S_2$ | |
| | $S_3$ | 7.70 | 7.70 | 7.70 | 7.70 | 7.70 | | 7.70 | 7.70 | 7.70 | 7.70 | 7.70 | $S_3$ | |
| LCRAC_30 | $T_{b,0.01}$ | 1.96 | 2.04 | 3.30 | 3.18 | 4.15 | MPa | 1.74 | 1.81 | 2.98 | 2.24 | 2.99 | $T_{b,0.01}$ | LCRAC_55 |
| | $T_{b,0,1}$ | 4.93 | 5.11 | 8.29 | 6.65 | 10.43 | | 4.37 | 4.54 | 7.49 | 4.69 | 7.51 | $T_{b,0,1}$ | |
| | $T_{b,0.2}$ | 6.50 | 6.75 | 10.93 | 8.30 | 13.77 | | 5.77 | 5.99 | 9.88 | 5.85 | 9.91 | $T_{b,0.2}$ | |
| | $T_{b,0.4}$ | 8.58 | 8.90 | 14.43 | 10.37 | 18.17 | | 7.61 | 7.90 | 13.04 | 7.31 | 13.08 | $T_{b,0.4}$ | |
| | $T_{b,0.6}$ | 10.09 | 10.47 | 16.97 | 11.80 | 21.36 | | 8.95 | 9.29 | 15.33 | 8.32 | 15.38 | $T_{b,0.6}$ | |
| | $T_{b,0.8}$ | 11.32 | 11.75 | 19.04 | 12.94 | 23.97 | | 10.05 | 10.43 | 17.20 | 9.12 | 17.25 | $T_{b,0.8}$ | |
| | $T_{bmáx}$ | 12.37 | 12.85 | 20.81 | 13.44 | 23.36 | | 10.98 | 11.40 | 18.81 | 9.47 | 16.81 | $T_{bmáx}$ | |
| | $T_{bf}$ | 4.95 | 5.14 | 8.33 | 4.03 | 8.03 | | 4.39 | 4.56 | 7.52 | 2.84 | 5.52 | $T_{bf}$ | |
| | $S_1$ | 1.00 | 1.0 | 1.00 | 0.9 | 0.75 | mm | 1.00 | 1.0 | 1.00 | 0.9 | 0.75 | $S_1$ | |
| | $S_2$ | 2.00 | 2.0 | 2.00 | 1.9 | 1.75 | | 2.00 | 2.0 | 2.00 | 1.9 | 1.75 | $S_2$ | |
| | $S_3$ | 7.70 | 7.70 | 7.70 | 7.70 | 7.70 | | 7.70 | 7.70 | 7.70 | 7.70 | 7.70 | $S_3$ | |

| | | fib MC 2010 | Louro (2014) | Freitas (2016) | Pereira (2019) | New Model | |
|---|---|---|---|---|---|---|---|
| LCRAC_80 | $T_{b,0.01}$ | 1.56 | 1.62 | 2.72 | 1.98 | 2.25 | MPa |
| | $T_{b,0,1}$ | 3.92 | 4.07 | 6.84 | 4.13 | 5.65 | |
| | $T_{b,0.2}$ | 5.17 | 5.37 | 9.02 | 5.16 | 7.46 | |
| | $T_{b,0.4}$ | 6.82 | 7.08 | 11.90 | 6.44 | 9.85 | |
| | $T_{b,0.6}$ | 8.02 | 8.33 | 14.00 | 7.33 | 11.58 | |
| | $T_{b,0.8}$ | 9.00 | 9.34 | 15.70 | 8.03 | 12.99 | |
| | $T_{bmáx}$ | 9.84 | 10.22 | 17.17 | 8.34 | 12.66 | |
| | $T_{bf}$ | 3.94 | 4.09 | 6.87 | 2.50 | 3.93 | |
| | $S_1$ | 1.00 | 1.0 | 1.00 | 0.9 | 0.75 | mm |
| | $S_2$ | 2.00 | 2.0 | 2.00 | 1.9 | 1.75 | |
| | $S_3$ | 7.70 | 7.70 | 7.70 | 7.70 | 7.70 | |

## C. Input values for the bond material of the SAB and LSB models

| Bond model | Parameters | $T_{b,0.01}$ | $T_{b,0,1}$ | $T_{b,0.2}$ | $T_{b,0.4}$ | $T_{b,0.6}$ | $T_{b,0.8}$ | $T_{bmáx}$ | $T_{bf}$ | $S_1$ | $S_2$ | $S_3$ |
|---|---|---|---|---|---|---|---|---|---|---|---|---|
| fib MC2010 | Reference | 2.28 | 5.72 | 7.54 | 9.95 | 11.71 | 13.14 | 14.36 | 5.74 | 1.00 | 2.00 | 9.60 |
| New model | Reference | 2.57 | 6.45 | 8.51 | 11.23 | 13.20 | 14.81 | 15.87 | 5.16 | 0.95 | 1.95 | 9.60 |
| | Variation 1 | 1.81 | 4.53 | 5.98 | 7.90 | 9.29 | 10.42 | 11.16 | 3.36 | 0.95 | 1.95 | 9.60 |
| | Variation 2 | 3.02 | 7.59 | 10.02 | 13.22 | 15.54 | 17.44 | 18.68 | 6.24 | 0.95 | 1.95 | 9.60 |
| | Variation 3 | 3.11 | 7.81 | 10.31 | 13.60 | 16.00 | 17.95 | 19.22 | 6.45 | 0.95 | 1.95 | 9.60 |
| | Variation 4 | 3.64 | 9.14 | 12.06 | 15.91 | 18.71 | 20.99 | 22.48 | 7.69 | 0.95 | 1.95 | 9.60 |
| | | MPa | | | | | | | | mm | | |

# D. Diagram results from the straight anchorage beam model

- **Bond Material:** fib Model Code 2010
  - Anchorage Length: 220 mm ; ☒ Yielding of steel at Step 54 v. Pull-out failure at Step 48

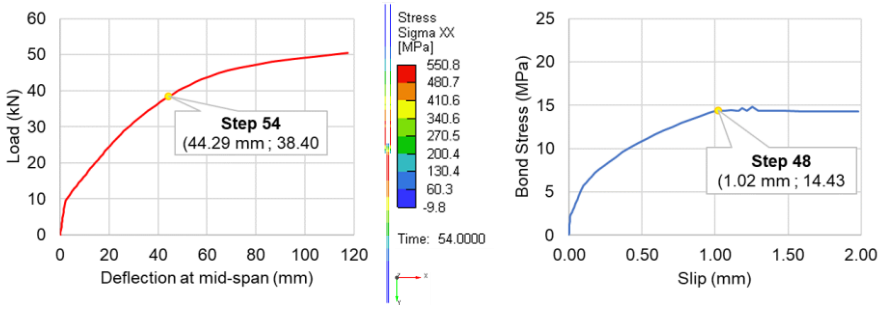


  - Anchorage Length: 225 mm ; ☑ Yielding of stell at step 52 v. Pull-out failure at step 54

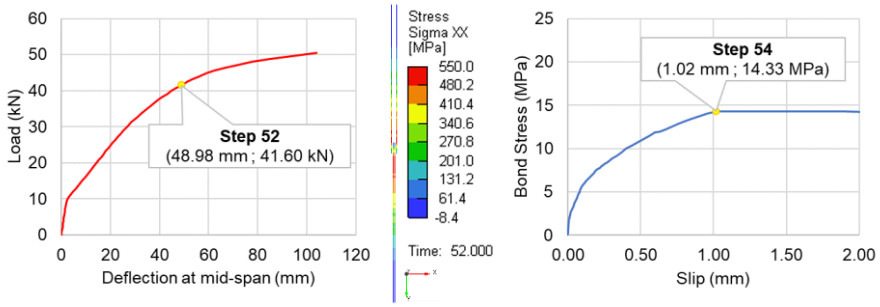


- **Bond Material:** New Model [Reference Parameters]
  - Anchorage Length: 195 mm ; ☒ Yielding of steel at Step 53 v. Pull-out failure at Step 48

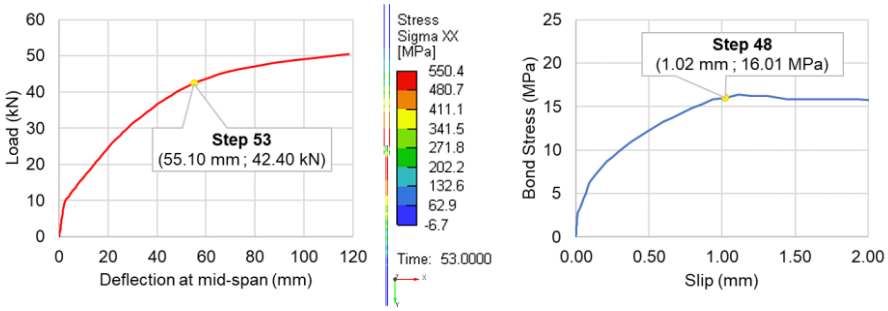


  - Anchorage Length: 200 mm ; ☑ Yielding of stell at step 55 v. Pull-out failure at step 59

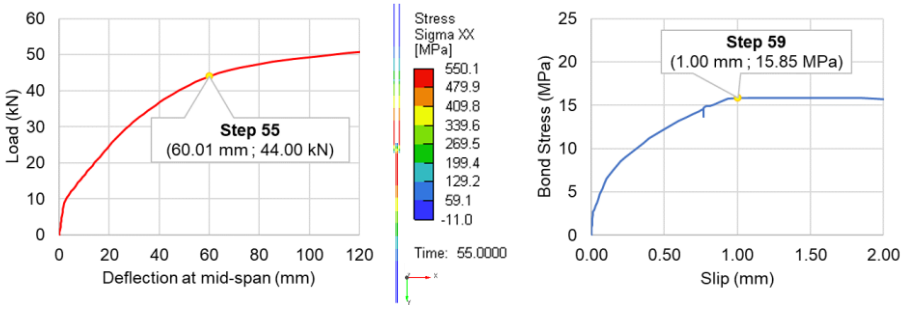

- **Bond Material:** New Model [Variation 1 → $RA_{<c}$ = 0.34]
  - Anchorage Length: 275 mm ; ☒ Yielding of steel at Step 55 v. Pull-out failure at Step 53

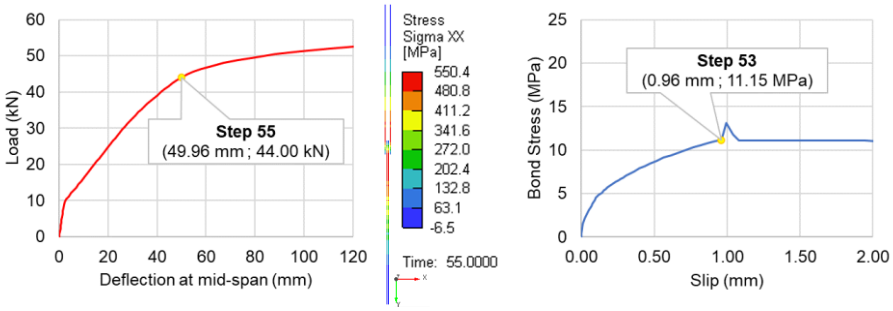


  - Anchorage Length: 280 mm ; ☑ Yielding of stell at step 55 v. Pull-out failure at step 56

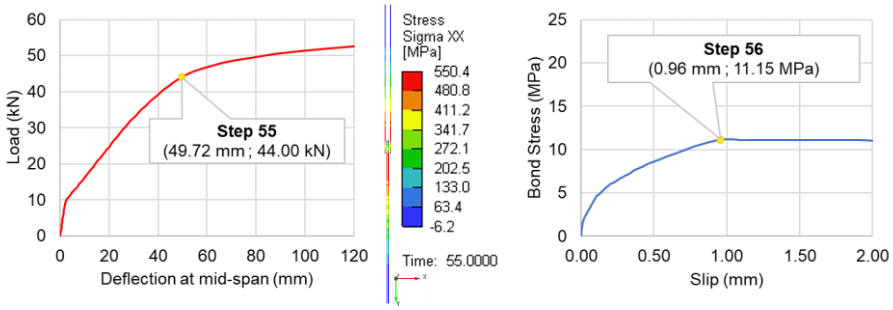


- **Bond Material:** New Model [Variation 2 → $f_R$ = 0.101]
  - Anchorage Length: 145 mm ; ☒ Yielding of steel at Step 54 v. Pull-out failure at Step 50

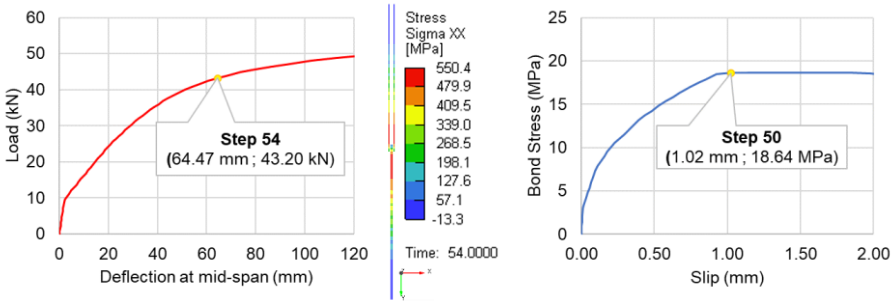


  - Anchorage Length: 150 mm ; ☑ Yielding of stell at step 53 v. Pull-out failure at step 57

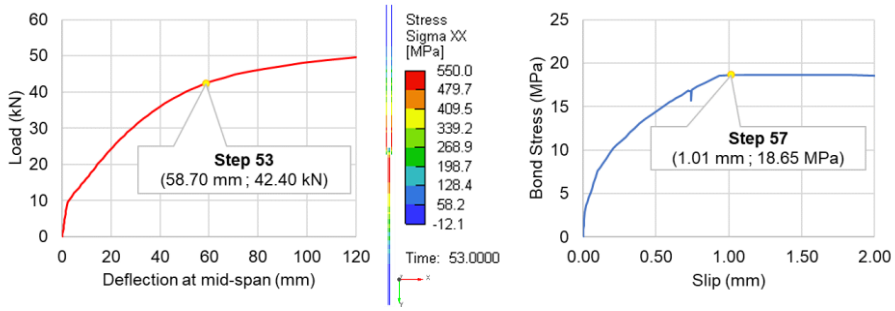

- **Bond Material:** New Model [Variation 3 → $RA_{\geq c}$ = 0.46]
  - Anchorage Length: 145 mm ; ☒ Yielding of steel at Step 54 v. Pull-out failure at Step 50

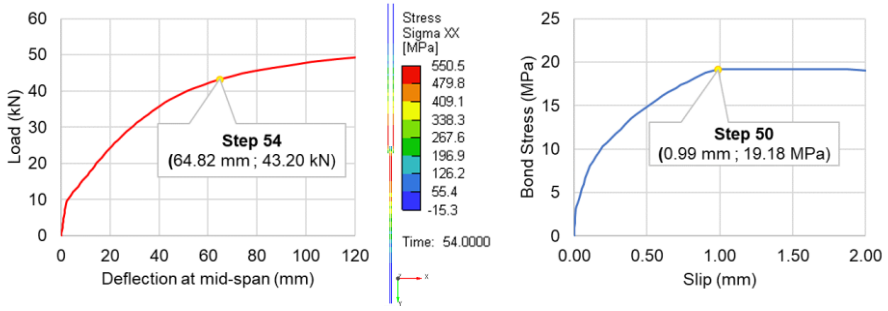


  - Anchorage Length: 150 mm ; ☑ Yielding of stell at step 53 v. Pull-out failure at step 58

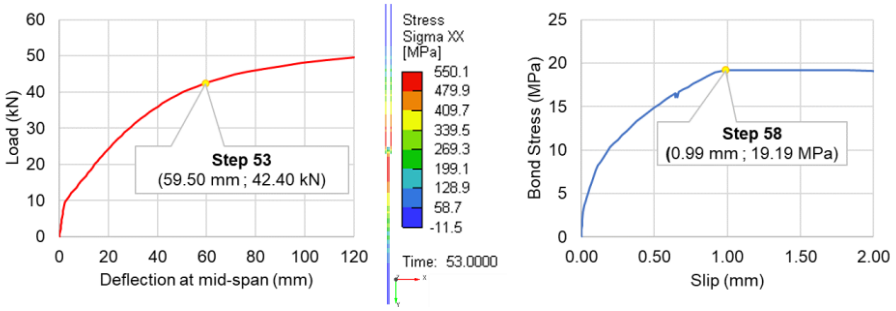


- Bond Material: New Model [Variation 4 → σ = 0.86]
  - Anchorage Length: 140 mm ; ☒ Yielding of steel at Step 54 v. Pull-out failure at Step 50

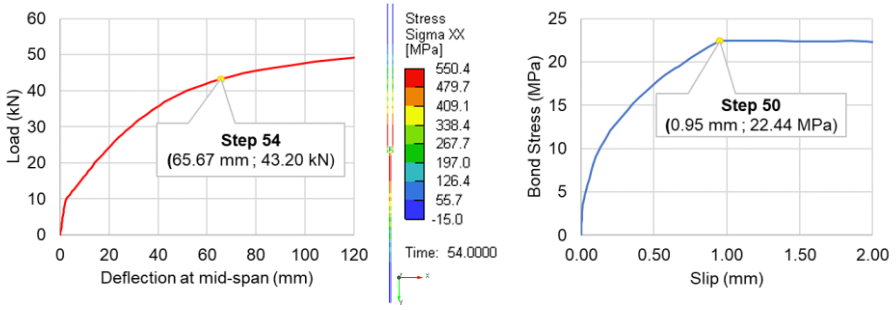


  - Anchorage Length: 145 mm ; ☑ Yielding of stell at step 53 v. Pull-out failure at step 55

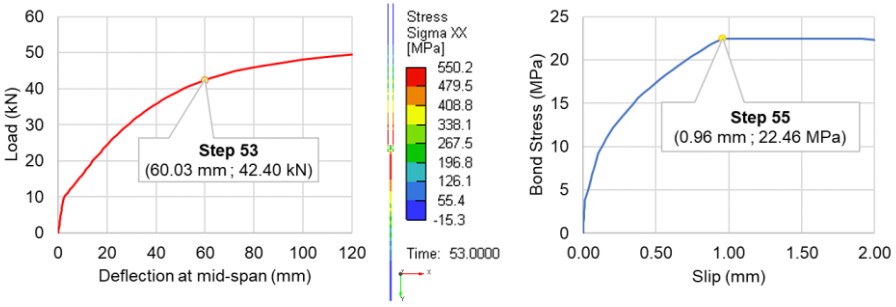

# E. Diagram results from the lap-splice beam model

- **Bond Material:** fib Model Code 2010
  - Anchorage Length: 120 mm ; ☒ Yielding of steel at Step 75 v. Pull-out failure at Step 75

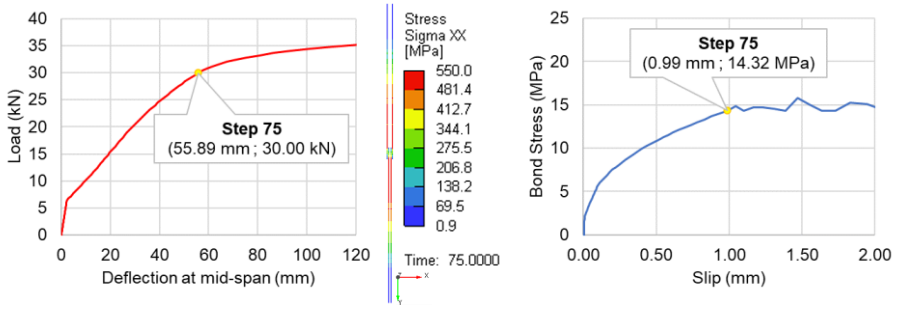


  - Anchorage Length: 125 mm ; ☑ Yielding of stell at step 75 v. Pull-out failure at step 77

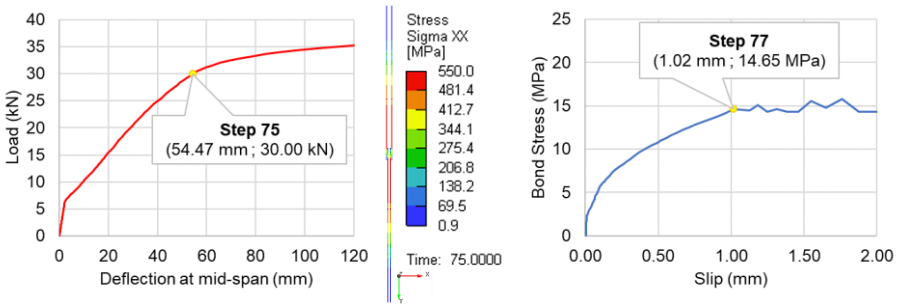


- **Bond Material:** New Model [Reference Parameters]
  - Anchorage Length: 110 mm ; ☒ Yielding of steel at Step 76 v. Pull-out failure at Step 75

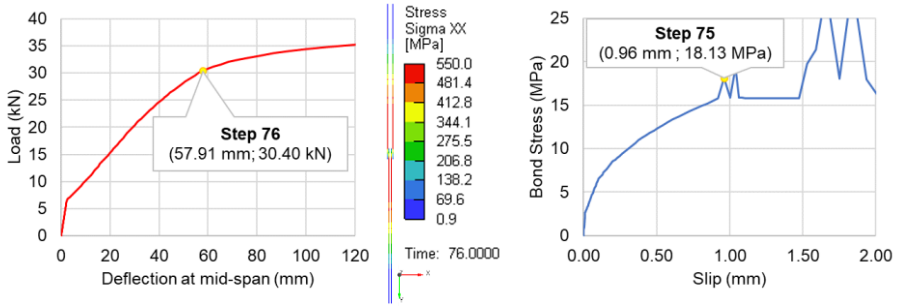


  - Anchorage Length: 115 mm ; ☑ Yielding of stell at step 75 v. Pull-out failure at step 78

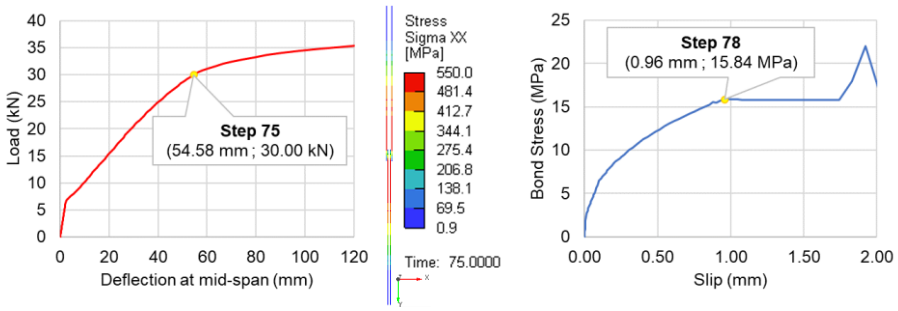

- **Bond Material:** New Model [Variation 1 → $RA_{<c}$ = 0.34]
  - Anchorage Length: 130 mm ; ☒ Yielding of steel at Step 75 v. Pull-out failure at Step 75

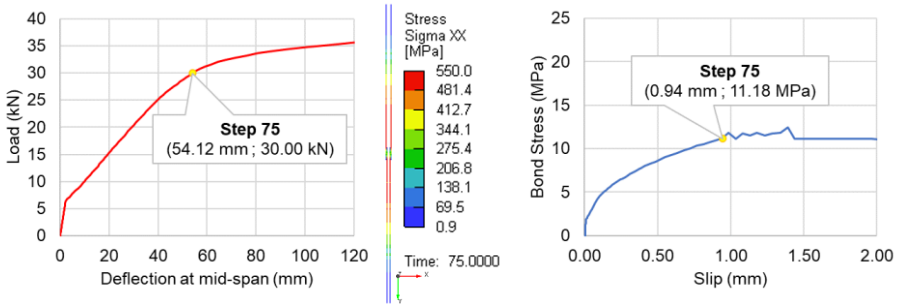


  - Anchorage Length: 135 mm ; ☑ Yielding of stell at step 75 v. Pull-out failure at step 77

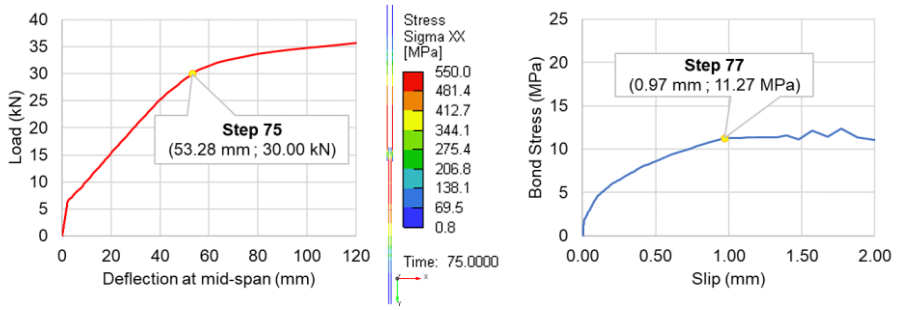


- **Bond Material:** New Model [Variation 2 → $f_R$ = 0.101]
  - Anchorage Length: 105 mm ; ☒ Yielding of steel at Step 75 v. Pull-out failure at Step 70

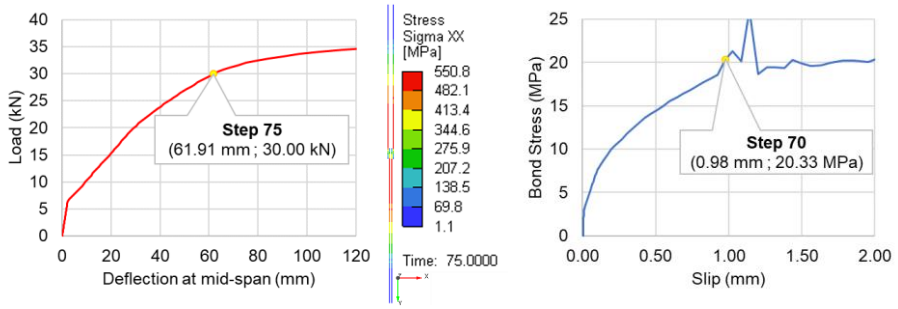


  - Anchorage Length: 110 mm ; ☑ Yielding of stell at step 76 v. Pull-out failure at step 85

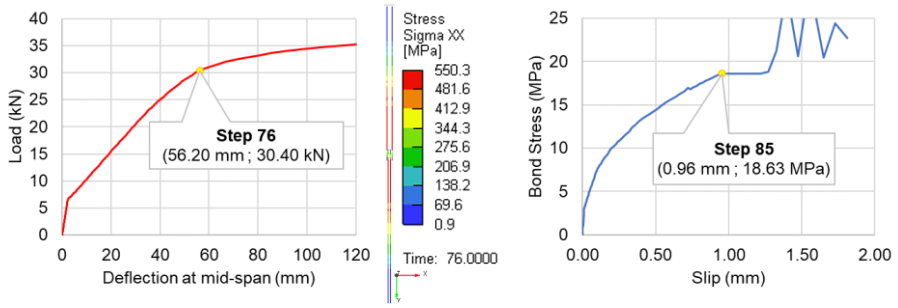

- **Bond Material:** New Model [Variation 3 → $RA_{\geq c}$ = 0.46]
  - Anchorage Length: 105 mm ; ☒ Yielding of steel at Step 74 v. Pull-out failure at Step 71

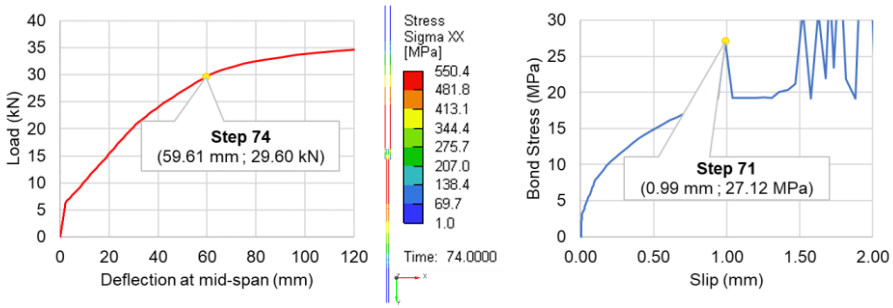


  - Anchorage Length: 110 mm ; ☑ Yielding of stell at step 76 v. Pull-out failure at step 85

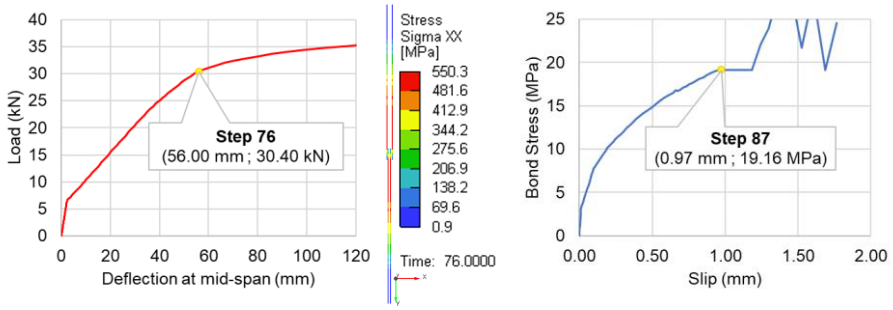


- Bond Material: New Model [Variation 4 → σ = 0.86]
  - Anchorage Length: 80 mm ; ☒ Yielding of steel at Step 74 v. Pull-out failure at Step 74

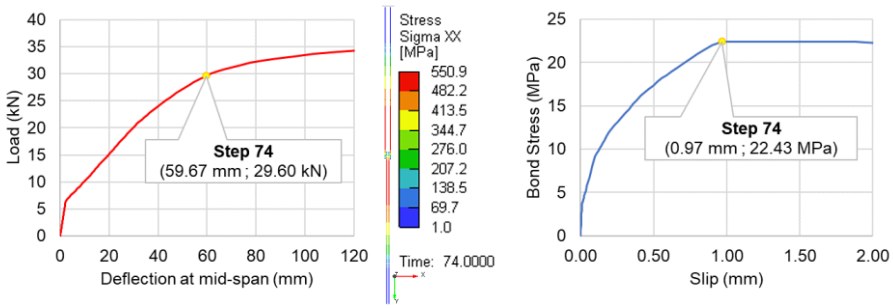


  - Anchorage Length: 85 mm ; ☑ Yielding of stell at step 74 v. Pull-out failure at step 75